UiO : Department of Mathematics
University of Oslo

Numerical investigation of internal solitary wave induced global instabilities

Joakim Soløy Sletten

Master's Thesis, Spring 2019

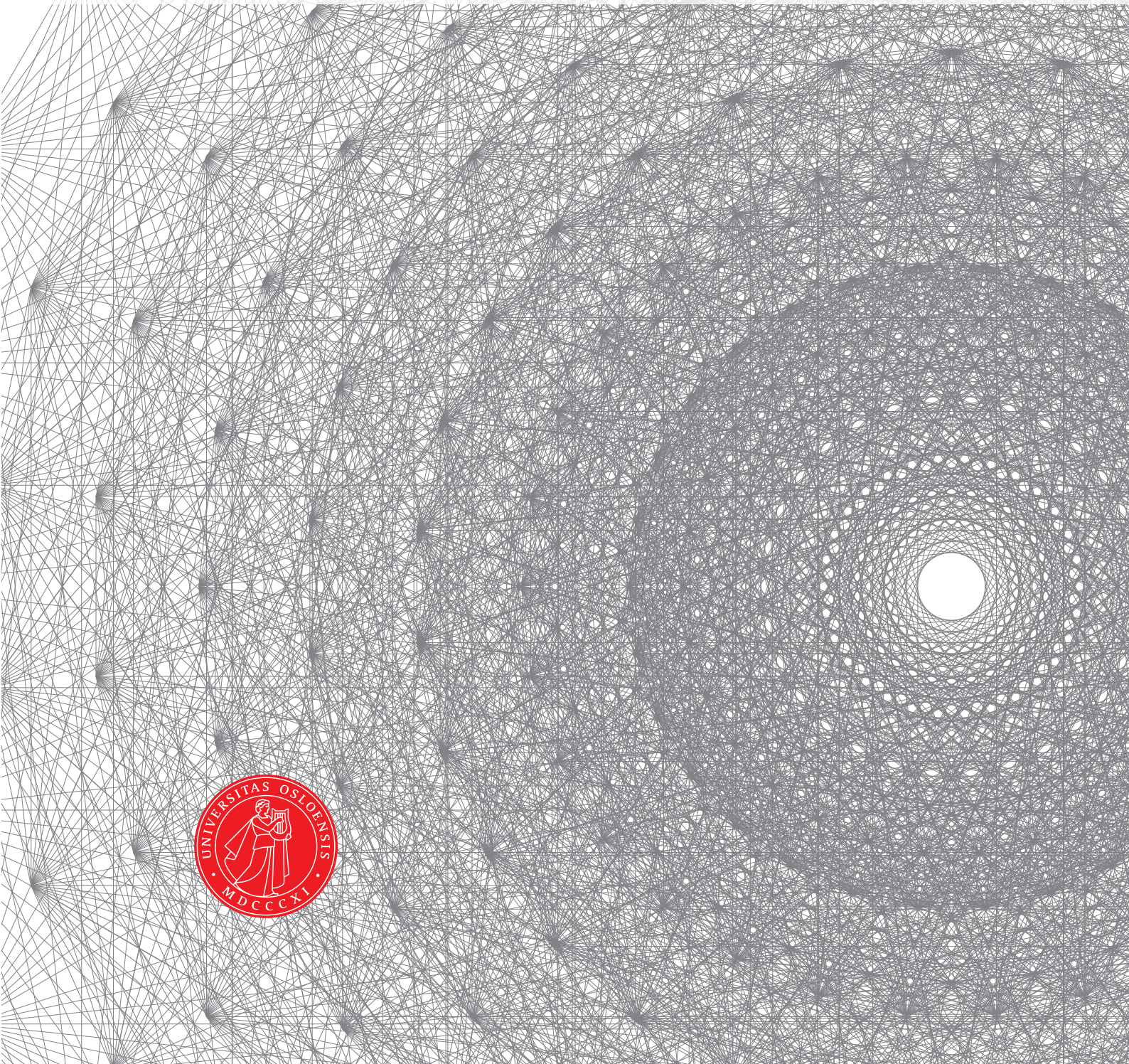

This master's thesis is submitted under the master's programme *Mechanics*, with programme option *Mechanics*, at the Department of Mathematics, University of Oslo. The scope of the thesis is 60 credits.

The front page depicts a section of the root system of the exceptional Lie group E_8, projected into the plane. Lie groups were invented by the Norwegian mathematician Sophus Lie (1842–1899) to express symmetries in differential equations and today they play a central role in various parts of mathematics.

Abstract

We have in this study investigated the global instability developing beneath large internal solitary waves (ISW) of depression in a wave tank. To perform this study, the numerical tool Basilisk has been used and we have worked in 2D. Our results proved to compare well to both fully nonlinear theory and experiments, making Basilisk a good choice of tool when studying internal waves. Simulations showed that Kelvin-Helmholtz instabilities developing in large ISWs, changed the wave profile in its rear part, making the wave broader. This effect was strongest in a two-layered fluid, while a three-layered fluid was better at retaining its wave shape. This led to larger velocities at the bottom of the wave tank, for the three-layered fluid, and a stronger resuspension of bed sediments. The simulations showed that a sloping bottom increased the vortex shedding. Having a sloping bottom increased the strength of the reverse flow leading to the development of larger vertices. This resulted in particles getting lifted over 60% of the total water depth for a slope steepness of $\alpha = 2.8°$. The results using a flat bottom showed a lift of particles of 20%. The slope used in Basilisk was comparable to the average slope steepness at the continental slope at 4°. The large resuspension of particles found in our simulations were strong enough for mixing of the entire water column to occur. Our study has showed that the instability appearing beneath a large ISW of depression can contribute massively towards resuspending sediments from the sea floor. If we include the ocean currents, we have a system where sediments from the sea floor gets lifted high up in the water column where ocean currents act as a transport mechanism, spreading nutrition over a larger area. Under the right conditions, ISWs can therefore be considered a nutrition pump in the ocean.

Acknowledgements

From the day I was introduced to large internal waves and the impact they have on the environment, I was determined to learn more about the subject. The last year, working with internal waves as the topic of my master's thesis, has been both challenging and exciting. I would like to thank John Grue for sharing his passion and knowledge throughout the study. Our conversations throughout the year have been very valuable and increased both my knowledge of internal waves and my passion for the subject. I would also like to thank Arne Bøckmann for helping me with the tool Basilisk.

A special thanks is given to Laila Andersland and Jon Alexander Pirolt for good discussions and great sessions in the hydrolab. Our collaboration has been very valuable in building a better understanding of the topic. In the end, I would also like to thank my family and girlfriend for continuous motivational support and helping me reach my goals.

Joakim Soløy Sletten
Oslo, 15 May 2019

Contents

List of Figures

List of Tables

CHAPTER 1

Introduction and background

In this study, we will investigate the global instability appearing beneath a propagating internal solitary wave (ISW) under depression in a wave tank. Both a two- and three-layered fluid will be investigated. Large ISWs give rise to several instabilities. This include convective breaking (overturning) in the upper layer (A), shear instabilities (Kelvin-Helmholtz) along the interface between the upper and lower layer (B) and global instabilities at the bottom (C) where bed sediments can be resuspended and transported vertically in the water column. An illustration of an ISW in a two-layered fluid, with the breaking processes highlighted, can be seen in figure (1.1). Our main focus in this study is the instability that happens at the bottom of the water column (C) and leads to flow separation and resuspension of sediments. The study has been completed using the numerical program Basilisk to simulate ISWs in a numerical wave tank, supported by some experiments performed in the hydrolab at the University of Oslo (UiO). The results are compared to both fully nonlinear theory and experiments for validation.

Internal waves

When we think about ocean waves, we usually only think about the ones visible for the human eye, but waves also exist beneath the ocean surface. These waves cannot be seen at the surface at first glance. Internal waves move in oceans that are layered. Layering occurs when warm and light surface water lays on top of colder and heavier water. Layering can also exist in fjords or along coastal lines where fresh water from rivers meets heavier seawater. The interface between cold and warm water is called a thermocline, while the interface between water with a density difference, e.g. fresh water and salt water, is called a pycnocline. In internal waves the upper layer is travelling in the same direction as the wave. Beneath the thermocline/pycnocline, water is moved in the opposite direction. When this shear increases its magnitude and reaches a threshold, the wave breaks. This instability is called Kelvin-Helmholtz rolls.

Internal waves are created in two different ways, both cases equally common. The first way is creation of waves when the tide travels over underwater mountains or along the continental shelf. A blockage of the tide-movement raises and lowers the thermocline, and internal waves are created. The second way, is due to winds acting on the ocean surface [29]. The wave period is typically 15-30 minutes, which is in general considered a fast movement in the ocean, especially in comparison to the tide that usually oscillates with a period of 12.4 hours. In areas at continental shelves such as Lofoten and Vesterålen,

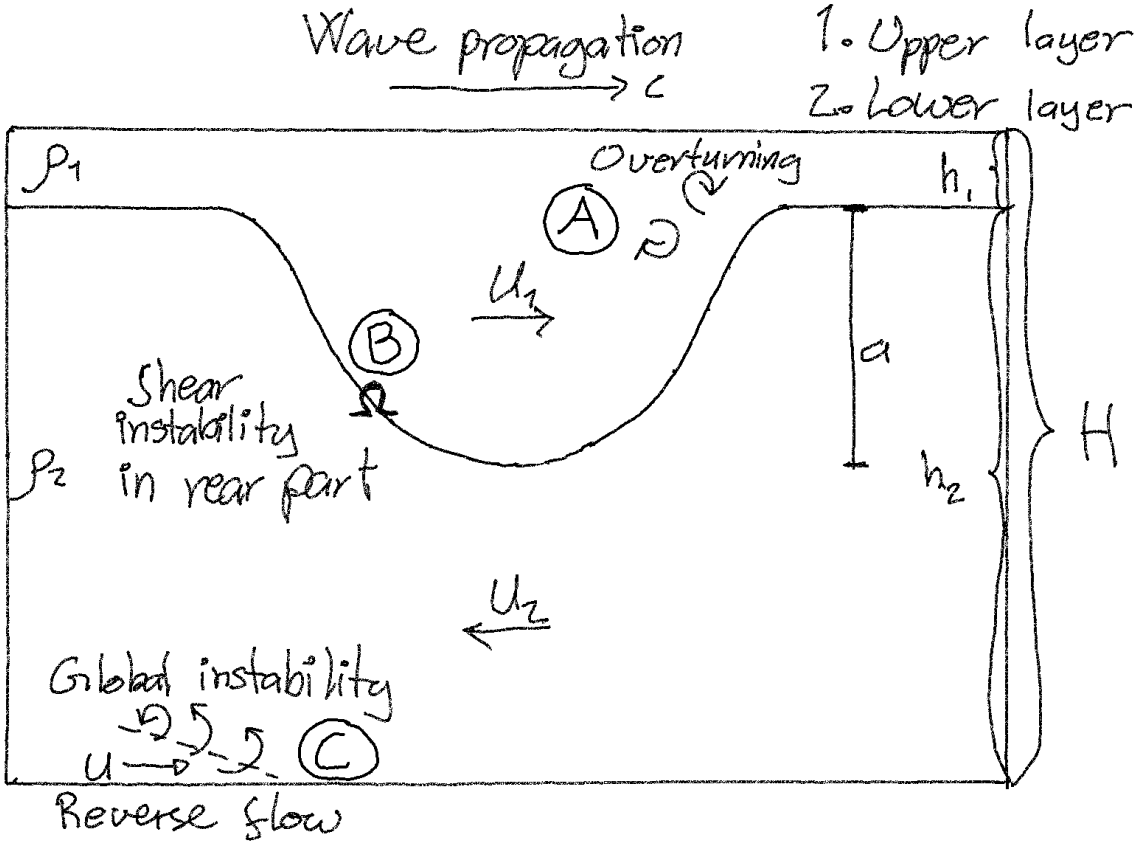

Figure 1.1: Illustration of an ISW propagating to the right with breaking processes highlighted

internal waves are created regularly [19]. Internal waves are most often occurring in groups and the distance between them is regulated by the tidal period. The tidal motion creates internal waves all across the world.

Internal waves come in two main forms: periodic wave trains and pulses. Both types move along the thermocline. The internal waves are always pointed out of the smallest layer, which means they most often are pointed downwards in the ocean (see figure 1.1). When these waves are created, they can propagate for long distances without changing their shape and strength. They are therefore considered as a transport mechanism in the ocean since they can move sediments from one place to another. The pulse waves can also occur along the sea bottom, however pointing upwards. Internal waves that propagates along the shelf slope can bring nutrition from the deep ocean to shallower and more light-rich oceans where the conditions are ideal for larvae etc.

ISWs with amplitude comparable to the ocean depth have previously been observed. Duda et al. (2004) [14] observed an ISW of depression in the South China Sea with an amplitude of 150m in a 340m deep ocean. In addition, Van Gastel and Ivey have observed ISWs with an amplitude of 80m in a 125m deep ocean (Presented in Diamessis and Redekopp [12], (2006)). In such settings, interaction between the wave and the bottom boundary is important and is expected to have a significant effect on the benthic dynamics. A benthic boundary layer is defined as the layer of water directly above sediments at the bottom of

the ocean, lakes or rivers.

1.1 Internal waves through history

The research history for internal waves started in the Arctic with Fridtjof Nansen's description of dead water. Fridtjof Nansen was an oceanographer and scientist who was interested in the ocean circulation on a large scale. A study of the ocean currents, both in the global and Arctic ocean was one of the main motivations of the Fram-trip in 1893-1896. During this trip, Nansen became the first to describe the dead water phenomena. Dead water happens due to internal waves created by a slowly moving ship. Sailors that entered a water with a thermocline, experienced a huge reduction in the ship speed, but this was hard to understand since the waves were impossible to see.

Internal waves are a collection of several phenomena including dead water, strong pulses and the internal tides. They contribute towards recycling in the ocean on a large scale. Similar phenomena exists in the atmosphere, but this did not get much attention before the development of the aviation. The modern interest in large internal waves started in the 1960s due to the development of ocean instrumentation, remote sensing and applied mathematics (Melville and Helfrich 2006 [32]). This development led to several observations of large internal waves in the coastal oceans. Among them was measurements by Perry and Schimke (1965) [34] in the Andaman Sea. They discovered internal waves with an amplitude of 80m and wavelength of 2000m for a thermocline situated at 500m in a 1500m deep ocean. Osborne and Burch (1980) [33] later showed that these waves were generated by tidal flows through channels in the Andaman and Nicobar island and propagated toward Sumatra over hundred kilometers away. It was early established that these were not linear dispersive waves. The wave amplitudes measured were too large compared to upper layer thickness for them to be linear. The observations that internal waves could propagate for long distances with finite amplitude, as those made by Osborne and Burch, suggested that dispersion was not dominant.

After the second world war, several highly technological American submarines sank. Submarines like to operate along a thermocline, since signals are reflected and spread from sonars and ships in this area, making it hard to discover the submarine. The submarines are moving neutrally in the fluid and follows the thermoclines vertical motion and therefore oscillates slowly. This can lead to accidents. One example was the accident involving the American submarine Tresher in 1963. Tresher had 129 passengers on board, but no one survived. The first explanations of what went wrong came in 1965. During this period, the first large internal waves in the ocean was observed in the Andaman ocean with an amplitude of 80m, which were quite a sensation. This is most likely what happened to Tresher. When a submarine travels deeper, the crew must reduce the density of the submarine in order to arrest the fall. If the submarine falls to fast, it can exceed the pressure capacity of the hull and the submarine will implode. There was no reports of equipment malfunctioning or weather storms in the area. Oceanographers had up to this point stated that internal waves did not exist. This changed when the Russian and American space program took pictures of the earth from space. These pictures showed signatures of internal waves at the sea surface. These signatures can be seen due to a powerful current that is induced by the internal waves at the ocean surface. This current varies along the wave extent. It is strong at a wave crest or trough and weaker at places

where the thermocline has smaller amplitudes. The surface current amplifies or weakens wind driven waves, depending on the wind direction and is perceived as changes in the light reflection from the sea surface.

The pulse wave extent is often comparable to the height of the upper layer, but the largest amplitude measured is five times the surface layer in the ocean (Grue 2013 [20]). Since the ocean is layered almost throughout due to differences in temperature or salinity, internal waves can be found everywhere. The thermocline is situated at approximately 200-300 m in equatorial areas. Other examples of thermoclines from the Norwegian coast can be found at the petroleum field Ormen Lange at 550 m and in Norwegian fjords that receive runoff, at only 4-10 m.

In recent history, most of the research on internal waves have come from the offshore-industry related to oil, gas and minerals. When using ships and platforms to bore or perform installations in deep water, long tubes are used as a connection between the vessel and the bottom of the ocean. Marine operations in equatorial areas have experienced the size and strength of internal waves and their induced surface currents. It is not until recent years that the knowledge of internal waves have increased. Several operators have lost their equipment due to internal waves, which can be a very costly affair. This increases the importance of having a thorough understanding of internal waves and their strengths, in order to perform safe and permanent marine operations. Ormen Lange is a petroleum field situated northwest of Kristiansund in Norway, which have stimulated lots of different research. The thermocline in this area is located at approximately 550 meters depth. This thermocline separates hot Atlantic Ocean at 7°C with colder polar water at -1°C. The Atlantic current can push the thermocline deep down in the ocean. Measurements performed at Ormen Lange shows a vertical extent of 300m from the usual thermocline at 550m depth to at most 850m depth. [20]

During the presidency of Barack Obama, 850,000 square miles of ocean were added to America's network of protected waters. It was pointed out that tidal waves floating over shallow banks form short internal waves. These banks were described as oases to marine life. The importance of such banks were later highlighted since the ocean is suffering from overexploitation, pollution and the increasing effect of climate changes. These oases are therefore important as a place where the marine life can recover. (National Geographic Feb 2017 [16])

1.2 Vesterålen

Large internal waves are recently observed east of Vesterålen, at the coast of Norway, by using synthetic "aperture" radar-technique. The waves can be seen on the left of figure (1.2). The waves are created on the edge of a coral reef, and the area is also known for having a high fishing density. In this case, it is the daily tides that create the large internal waves. The pycnocline is then raised to a higher level, before being "released" and internal waves starts to propagate upstream. In this area, a sloping bottom is present (see figure 1.3), with an average slope steepness of 3.2°. The waves spotted in this area have an amplitude of approximately 60m in a 200m deep ocean and a wavelength $\lambda \approx 500$m. The average wave propagation speed is approximately 0.10 m/s. The size of these waves give rise to several instabilities. Firstly we have the convectively induced breaking in the upper

layer of the wave. This means that nutrition in the upper layer are transported down into the sea, following the internal waves. Secondly, if the internal waves become large enough, a shear instability called Kelvin-Helmholtz appears. This instability mixes the layers of different densities at a vertical distance comparable to the wave amplitude. Lastly we have the development of vortices and vertical transportation along the bottom of the ocean. This instability occurs when the waves become very large and strongly nonlinear and is seen on the lee-side of the wave [19].

Figure 1.2: Signature of ISWs outside of Lofoten and Vesteralen, figure 1 from Grue (2018) [19]

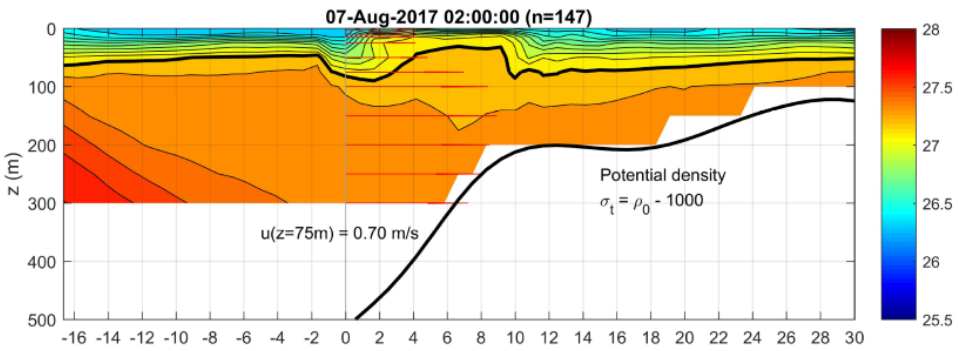

Figure 1.3: Illustration of the bottom topography in Vesterålen. The x-axis is the length scale given in km, figure 6 from Grue (2018) [19]

1.3 Breaking processes of ISWs

There are as mentioned before, several breaking mechanisms that occur for ISWs of large amplitude. We will now give an introduction to how and when they occur and present the research history for each breaking process.

Convective breaking

Convective breaking appears in internal waves, when the particle velocity u exceeds the fluid velocity c ($u/c > 1$). Carr et al. (2008) [10] showed through experiments both convective breaking and shear instabilities in strongly nonlinear waves. They proved that the upper boundary condition had large impact on the convective breaking. By using a rigid lid at the upper boundary, it became possible to run with larger wave amplitudes before the convective breaking took place compared to having a free surface. In 2000, Grue et al. [21] did both experimental and theoretical calculations, which showed that the horizontal wave velocity became equal to the wave speed when the wave amplitude became $0.855h_1$, where h_1 is the upper layer height. Their study showed that convective breaking also could take place for u/c close to 1.

Kelvin-Helmholtz instability

Kelvin-Helmholtz instability can appear when having a velocity shear in a continuous fluid or a velocity difference along the interface between two fluids. An example of this is wind blowing over the ocean. Kelvin-Helmholtz instability appears both in the ocean and in the atmosphere. Several studies have been made on this instability.

Theoretical approximations of the wave induced Kelvin-Helmholtz instability was made by Bogucki and Garret (1993) [5]. They suggested that the shear instability occurs when the Richardson number goes below 1/4, resulting in breaking and mixing of the flow. The Richardson number describes the relationship between buoyancy and flow shear forces and is defined as

$$Ri = \frac{N^2}{(\frac{\partial u}{\partial z})^2} \tag{1.1}$$

where N is the Brunt-Vaisala frequency. Bogucki and Garret [5] based their calculations on the KdV and Benjamin-Ono equations, and the pycnocline was assumed thin. Fructus and Grue (2004) [15] found similar results for the instability in a stratified shear flow, but noted that the Richardson number in some occasions had to be less than 0.20 for instability to appear. Grue et al. (1999) [18] showed how Kelvin-Helmholtz instabilities contributed towards changing the internal wave from its original form to a more broad-crested wave in its rear part. This meant that the experiments stopped matching the standard nonlinear wave theory, as shown in figure (1.4). Here, the wave amplitude is gradually increased and we can clearly see in the final figure the appearance of Kelvin-Helmholtz instabilities due to the broad-crested wave.

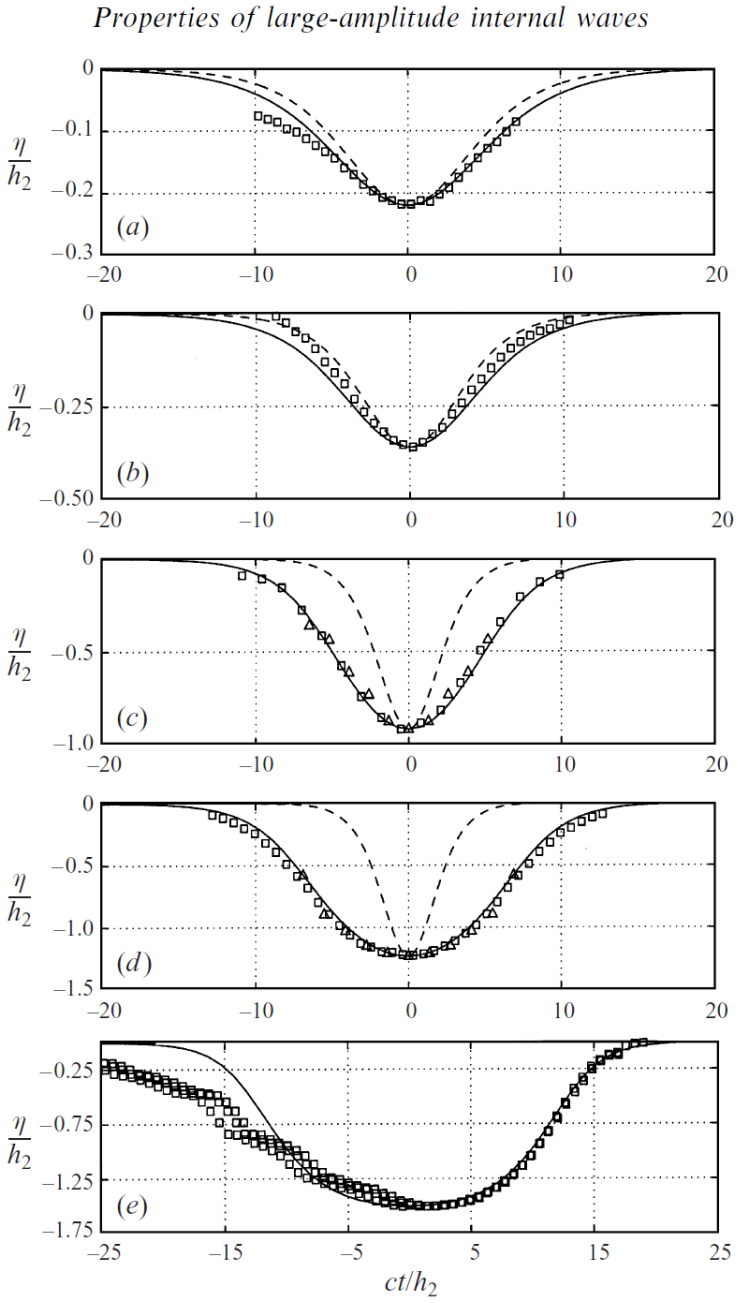

FIGURE 7. Wave profile $\eta(ct)$ at fixed position at camera 2 (10.5 m). Squares: measured pycnocline. Triangles: measured jump in velocity. Solid line: fully nonlinear theory. Dashed line: KdV theory (3.6). (*a*) $a/h_2 = 0.22$. (*b*) $a/h_2 = 0.36$. (*c*) $a/h_2 = 0.91$. (*d*) $a/h_2 = 1.23$. (*e*) $a/h_2 = 1.51$.

Figure 1.4: Comparison between experiments, weakly nonlinear and fully nonlinear theory, showing the presence of Kelvin-Helmholtz instability. From Grue et al. (1999) figure 7 [18].

Carr et al. (2008) [10] compared experiments with wave theory and concluded that the instability comes as a mix of convective and shear tension. The convective instability also contributed towards increasing the shear tension. The stability criteria found proved to compare well to Fructus and Grue (2004) [15].

In 2017, Carr et al. [9] investigated the spatial and temporal evolution of the shear-induced billows associated with breaking internal solitary waves through both experiments and numerical work. The characteristics of each billow were decided in each experiment and the interactions of the billows were investigated and classified. Both wave steepness and amplitude proved to have large impact on if breaking occurred and how the billows interacted with each other. The billow characteristics were sorted in four categories:

1. The billows grow separately
2. The billows pair together
3. They engulf each other
4. Fails to completely overturn

The number of billows that evolved proved to be dependent on the wavelength. Shorter waves had fewer but larger billows in comparison with longer waves for a given stratification.

Vortex shedding and vertical transport along the bottom

A third type of instability related to strongly nonlinear waves have recently been reported from several studies, such as Statsna and Lamb (2002) [39], Diamessis and Redekopp (2006) [12], Carr and Davies (2006) [7], Carr et al. (2008) [8] and Aghsaee et al. (2012) [1]. Both experimental and numerical studies have been made in the attempt to describe the criteria for this global instability to appear and characterize its strength. In addition, they have looked at the possibility for this instability to contribute towards resuspension of sediments vertically from the seafloor and with this contribute with nutrition throughout the water column as well as recirculating the water. Large internal waves have been observed outside of Vesterålen that satisfies the requirements for global instability to occur [19]. The same area is marked as an area of high fishing density and a coral reef is also situated nearby. This fact makes the global instability even more interesting.

Statsna and Lamb (2002) [39] studied the interaction between fully nonlinear solitary waves and the seafloor. Their study showed that the vortex shedding appearing underneath internal waves was an effective mechanism of transporting sediments away from the seafloor. By looking at stress-profiles along the bottom they concluded that the global instability was strong enough for resuspension of sediments to occur.

In 2006, Diamessis and Redekopp [12] performed direct numerical simulations, where they investigated the characteristics for benthic excitation of ISWs for different wave parameters. Their main focus was to look at the instability evolving beneath an internal wave under depression. If the wave amplitude was large enough, a reverse flow induced by the wave motion appeared behind the wave, moving in the same direction as the wave, opposite of the fluid in the lower layer. If the reverse flow was strong enough, it could evolve into a region of resuspension. Diamessis and Redekopp tried to find a criteria for global instability to appear. Their results showed that for $Re_w > 5 \times 10^3$ and a wave amplitude exceeding a critical value, a global instability could be found near the bottom, where an adverse pressure gradient developed leading to a sufficiently strong reverse flow. The critical wave amplitude α_{0cr} was found to decrease with an increase in Reynolds

number Re_w as seen in equation (1.2). The criteria for global instability to occur was suggested to be valid for both coastal oceans and rivers.

$$\alpha_{0cr} = \frac{1}{2}\left(\frac{Re_w}{10^{-4}}\right)^{-0.12} \tag{1.2}$$

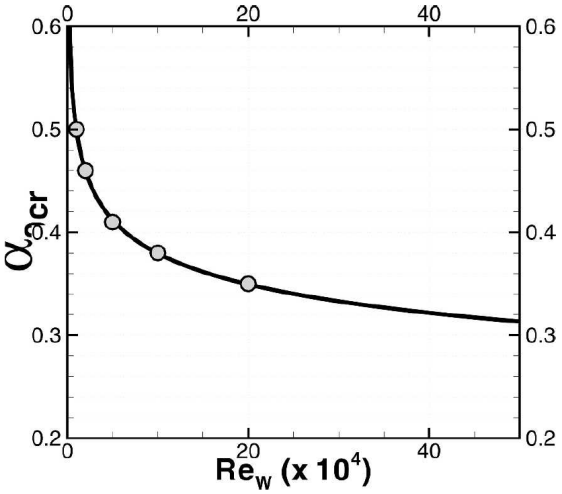

FIG. 7. Critical nondimensional wave amplitude α_{0cr} as a function of Re_W for mode-1 solitary wave of depression. The solid line represents the exponential best-fit function: $\alpha_{0cr} = 0.5(Re_W/10^4)^{-0.12}$.

Figure 1.5: Critical wave amplitude vs Reynolds number, from Diamessis and Redekopp (2006) figure 7 [12].

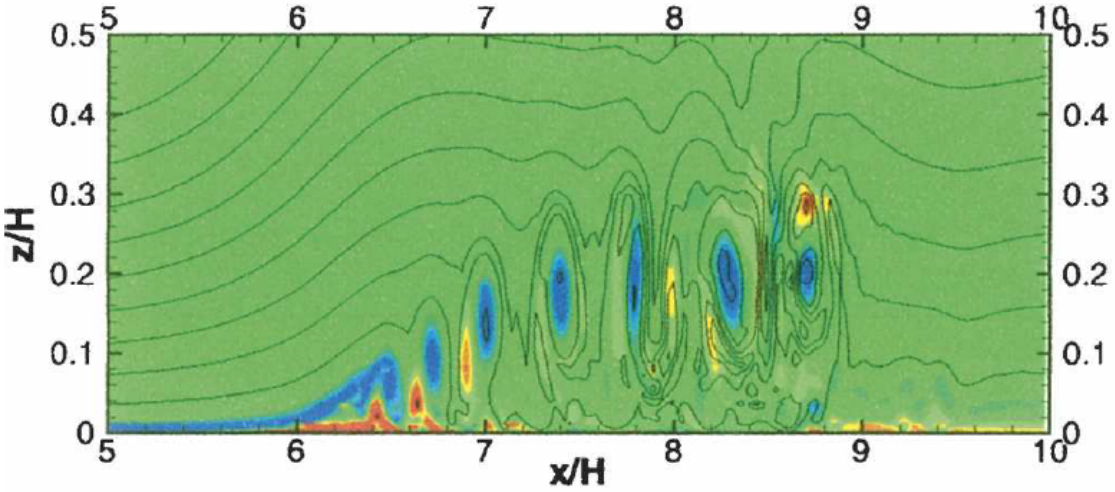

Figure 1.6: Visualization of global instability, from Diamessis and Redekopp (2006) figure 10b [12]

Carr and Davies (2006) [7] performed experimental measurements of the boundary layer region beneath ISWs under depression of large amplitudes propagating over a smooth topography. Their experiments were performed in a two-layered fluid. While Diamessis and Redekopp [12] focused on characterizing global instability and find a criteria for when it occurs, Carr and Davies wanted to obtain data of velocities near the bottom for a range of different wave parameters, phase velocities and boundary layer thicknesses. Their experiments were mainly performed with a wave amplitude comparable to the upper layer thickness, $a/h_1 \sim 1$. The experiments showed that the velocity field was affected by the bottom, leading to a decrease of the wave profile width with the distance to the wall as seen in figure 1.7. In addition to the observed changes of the horizontal velocity profiles, an unstable boundary jet-flow developed along the wall. This flow was small in magnitude compared to the maximal velocity in the fluid, but was directed in the same direction as the wave, opposite of the internal lower layer of fluid, as reported by Diamessis and Redekopp (2006). The boundary layer flow was generated due to the presence of an adverse pressure gradient aft of the wave leading to a reverse flow. Theoretical approximations of the location of the separation bubble was found to compare well with the experimental data, and confirmed that the boundary layer flow was a result of boundary layer separation. Good qualitative comparisons were made towards the numerical results of Diamessis and Redekopp (2006). Both the gradual narrowing of the velocity profile near the bottom in addition to the generation of a reverse flow were reproduced by the numerical model of Diamessis and Redekopp (2006), despite differences in the experimental and numerical simulations.

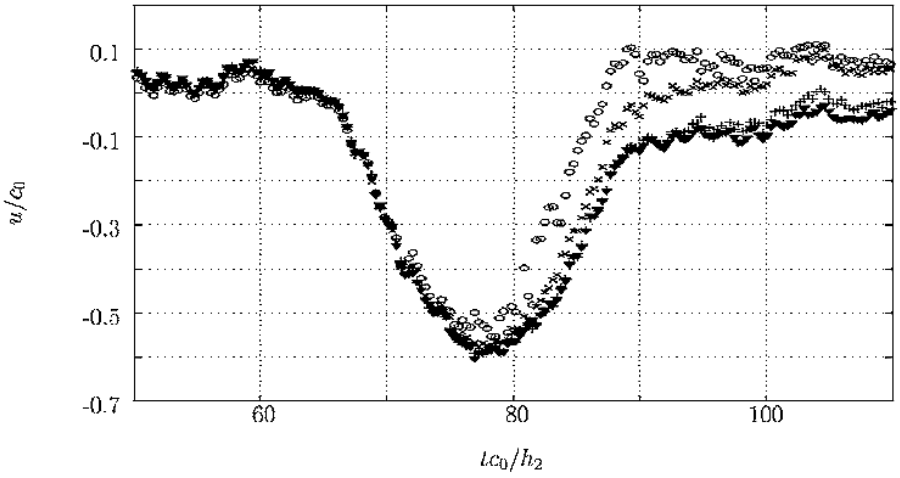

FIG. 7. Horizontal velocity u/c_0 vs time tc_0/h_2 for experiment 20538, x/L=0.66, and z/h_2=(○) 0.1, (×) 0.2, (+) 0.4, (▼) 0.6.

Figure 1.7: Horizontal velocity profiles for different distances from the wall vs time, from Carr and Davies (2006), figure 7

In 2008, Carr et al. [8] made an experimental study of global instability by looking at the ISW induced benthic velocity fields for Reynolds numbers and wave amplitudes larger then those used in Carr and Davies (2006) [7]. The experiments were performed in

an undisturbed density field that consisted of a homogenous upper layer, over a linear stratified pycnocline and a homogenous lower layer. The setup can be seen in figure (1.8).

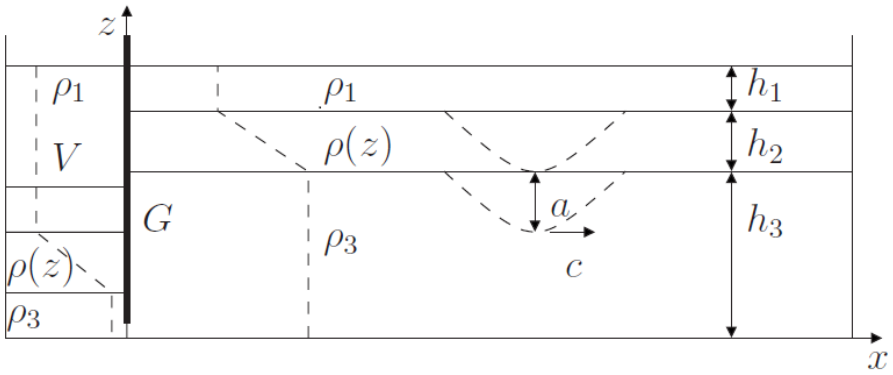

Figure 1.8: The experimental setup of Carr et al. (Figure 1 from [8])

A depression wave was created and global instability was observed in the super-critical cases. The vortex-structure that developed was similar to previous suggestions made by Diamessis and Redekopp (2006) [12]. By comparing their results with Diamessis and Redekopp (2006), they found qualitative similarities but quantitative differences. Carr et al. (2008) [8] found the critical wave amplitude for global instability to be approximately half of previously suggested by Diamessis and Redekopp (2006). They also found the vertical velocity of a general vortex to be two sizes of order smaller and the maximal vertical distance travelled by a vortex to be half of the results of Diamessis and Redekopp. The experiments of Carr et al. showed that if the reverse flow was sufficiently deep for a given time period, global instability could be spotted (generation of vortices along the bottom). The critical wave amplitude for global instability for Reynolds numbers in the area $Re_w \in [5.8, 6.6] \times 10^4$ was shown to be much smaller than previously suggested by Diamessis and Redekopp. A previous study by Grue et al. (1999) [18] stated that weakly nonlinear KdV theory was valid for amplitudes up to $a/h_1 = 0.4$ where a is the wave amplitude and h_1 the upper layer thickness. Some of the differences in the two results can then be explained by Diamessis and Redekopps use of soltions with amplitude exceeding $a/h_1 = 0.4$, an area where KdV theory compares bad to both experiments and fully nonlinear wave theory. Since the experimental work by Carr et al. were performed in a wave tank of limited length, it was impossible to compare some of the results obtained by Diamessis and Redekopp with their experimental work. One of these was the maximal height of a vortex due to global instability in the boundary layer. Carr et al. obtained a maximum lift of 17% of the total water column, while Diamessis and Redekopp had a maximum lift of approximately 30-35% as seen in figure 1.6.

In 2012, Aghsaee et al. [1] investigated global instability in a laminar boundary layer beneath an ISW of depression that propagated along a flat bottom in addition to a sloping topography. The study was done numerically by Direct Numerical Simulation (DNS). Two types of slopes were used:

1. $S = 0.05$: A mild slope

2. $S = 0.10$: A steep slope

They discovered that vortex shedding was more likely to occur in the event of a flat bottom for broader waves of large amplitudes, giving steeper wave profiles, larger velocities in the bottom layer and thereby stronger pressure gradients in comparison to more narrow-crested waves having smaller wave amplitudes. In the case of an internal solitary wave propagating over a sloping bottom, vortex shedding occurred in all simulations, due to the gradually increasing current along the bottom when the wave shoals. Their results showed a maximum lift of vortices of 33%. Similar simulations by Statsna and Lamb (2008) [38] showed a lift close to 25%. These were greater than the experimentally achieved 17% by Carr et al. (2008) [8] for a flat bottom, where three-dimensional effects are likely to affect the results, with a more rapid degeneration of the shed vortices. Aghsaee et al. also discovered that the vertical velocities and bed shear was increased for a shoaling wave and suggested that shoaling ISWs can have an important role in bed sediment resuspension along sloping regions of oceans and lakes.

Implications of breaking internal waves

Breaking internal waves have several implications on its surroundings, but its contribution towards mixing are considered the most important. Many authors have related ISWs of large amplitude as the main contributor towards mixing on the shelf. Jeans and Sherwin (2001) [24] concluded that ISWs were the prime source of mixing on the Portuguese shelf. St. Laurent (2008) [30] found that ISWs of large amplitude make the South China Sea one of the most dissipative shelf regions in the entire world. Several studies (Bogucki et al. 2005 [6], Carter et al. 2005 [11]) have also identified that internal waves can resuspend and transport sediments from the sea floor through global instabilities with its strong currents that develop beneath large ISWs. Quaresma et al. (2007) [35] have observed ISW induced resuspension in the coastal ocean to ascend as high as 50% of an 80m water column.

1.4 Motivation

We have now established that ISWs of large amplitude can contribute towards resuspension and transportation of sediments from the sea floor. This process are considered as a potentially big source of distributing nutrition for the ocean biology and contribute to recycling of the water. In this project, we will investigate the global instability that occurs on the bottom of the ocean. We will try to maximize the conditions for it to happen, in addition to track single particles to try to get an understanding of how sediments from the ocean floor are moved upwards in the water column. The study includes internal waves propagating over both a flat and a sloping bottom. Our main motivation for this study is to investigate whether ISWs can be considered a nutrition pump in the ocean, and try to discover the conditions where resuspension is at its largest. The research will be done both numerically using Basilisk, and experimentally in the hydrolab at UiO.

CHAPTER 2

Wave models

The linear theory of internal solitary waves in form of the motion of two fluids were first expressed by Stokes in 1947, with nonlinear extensions made by Boussinesq in the 1870's. In 1932, Dubreil-Jacotin developed the equations for nonlinear motion in a stratified fluid. Then followed the creation of the weakly nonlinear Korteweg de Vries (KdV) equations by Keulegan (1953) [26] and Long (1956) [31]. Weakly nonlinear and weakly dispersive theories are useful when modelling internal waves where the density lines have moderate excursion in relation to the zero-level and the waves are long compared to the depth. The presented equations are collected from Grue et al. (1997) [17] and chapter 5 of Grue and Trulsen (2006) [22].

2.1 Korteweg-De Vries equations

Continous stratification

The development of weakly nonlinear theory of internal waves in a continuous stratified fluid started with Benney (1966) [4] and was later extended to the KdV-equations and its higher order extensions. We start by introducing a coordinate system where x is directed horizontally and y vertically. The internal wave motion takes place in the fluid between two horizontal walls at $y = 0$ and $y = -H$. The density field is defined as $\bar{\rho}(y)$. We focus on 2D wave motion where the velocity field is given as $\vec{v}(x, y, t) = [u(x, y, t), v(x, y, t)]$ and the density perturbation as $\rho(x, y, t)$, which makes the total density field given as $\rho_s = \bar{\rho} + \rho$. The equations of motion and continuity equation is then given as:

$$\rho_{st} + u\rho_{sx} + v\rho_{sy} = 0 \tag{2.1}$$
$$\rho_s(u_t + uu_x + vu_y) = -p_x \tag{2.2}$$
$$\rho_s(v_t + uv_x + vv_y) = -p_y - g\rho_s \tag{2.3}$$
$$u_x + v_y = 0 \tag{2.4}$$

where p is pressure and g acceleration due to gravity. We define the wave amplitude a and wavelength λ. Next we introduce two non-dimensional numbers $\epsilon = a/H$ and $\mu = H^2/\lambda^2$, where ϵ gives a number on the nonlinearity of the problem and μ a number for the dispersive effects. We assume that both ϵ and μ are of the same order of magnitude. Next, we introduce non-dimensional quantities:

$$u = Uu', \quad v = Vv', \quad p = \rho_0 gHp', \quad \rho = \rho_0\rho', \quad t = \omega^{-1}t' \tag{2.5}$$

where we have the relations that $UH = V\lambda$ and $\omega\lambda = U$. Now, we introduce the inverse Froude number $G = gh/U^2$ and the stream function $\psi'(x, y, t)$. Since the fluid is assumed irrotational we achieve the relationship $(u', v') = (\psi'_y, -\psi'_x)$. The next step is to introduce the non-dimensional quantities into the equations of motion and continuity (2.1). This gives us the following equations:

$$\rho_t - \bar{\rho}_y\psi_x + \epsilon(\rho_x\psi_y - \rho_y\psi_x) = 0 \tag{2.6}$$

$$\begin{aligned}&(\bar{\rho}\psi_{yt})_y - G\rho_x + \epsilon[\rho\psi_{yt} + \bar{\rho}(\psi_y\psi_{xy} - \psi_x\psi_{yy})]_y + \mu\bar{\rho}\psi_{xxt}\\ &+\epsilon^2[\rho(\psi_y\psi_{xy} - \psi_x\psi_{yy})]_y + \mu\epsilon[\rho\psi_{xt} + \bar{\rho}(\psi_y\psi_{xx} - \psi_x\psi_{xy})]_x\\ &+\mu\epsilon^2[\rho(\psi_y\psi_{xx} - \psi_x\psi_{xy})]_x = 0\end{aligned} \tag{2.7}$$

The rigid lid condition $\psi_x = 0$ is then applied at $y = 0, -1$. We search wave solutions by introducing an amplitude function $A(x, t)$ in addition to expanding $\rho(x, y, t)$ and $\psi(x, y, t)$ by:

$$\rho(x, y, t) = A\varrho(y) + \epsilon A^2\tilde{\varrho}(y) + \mu A_{xx}\hat{\varrho}(y) \ + \ ..., \tag{2.8}$$

$$\psi(x, y, t) = A\phi(y) + \epsilon A^2\tilde{\phi}(y) + \mu A_{xx}\hat{\phi}(y) \ + \ ... \tag{2.9}$$

These expansions are then introduced into (2.6, 2.7), which by leading order gives us:

$$A_t + cA_x + \epsilon\alpha_0 AA_x + \mu\beta_0 A_{xxx} = 0, \tag{2.10}$$

$$(\bar{\rho}\phi_y)_y - \frac{G\bar{\rho}_y}{c^2}\phi = 0, \quad \phi(0) = \phi(-1) = 0. \tag{2.11}$$

Equation (2.11) is an eigenvalue problem that has an infinite set of eigenvalues $c_0 > c_1 > ... > 0$ with corresponding eigenfunctions $\phi_0(y), \phi_1(y), ...$ The eigenvalues represent the wave speed and the eigenfunctions the vertical structure of the n-th linear mode of hydrostatic internal wave motion. We will only use the lowest mode (c_0, ϕ_0), representing the longest waves. The boundary value problem for $\tilde{\phi}$ and $\hat{\phi}$ are used to determine the constants α_0 and β_0, and looks as following:

$$(\bar{\rho}\tilde{\phi}_y)_y - \frac{G\bar{\rho}_y}{c^2}\tilde{\phi} = -\alpha_0\frac{G\bar{\rho}_y}{c^3}\phi + \frac{1}{2c}(\bar{\rho}_y\phi\phi_y)_y + \frac{1}{2c}[\bar{\rho}(\phi_y^2 - \phi\phi_{yy})]_y - \frac{1}{2c}\bar{\rho}_{yy}\phi^2 \tag{2.12}$$

$$(\bar{\rho}\hat{\phi}_y)_y - \frac{G\bar{\rho}_y}{c^2}\hat{\phi} = -\bar{\rho}\phi - \frac{2\beta_0 G\bar{\rho}_y\phi}{c^3} \tag{2.13}$$

with the boundary conditions $\tilde{\phi}(0) = \tilde{\phi}(-1) = 0$ and $\hat{\phi}(0) = \hat{\phi}(-1) = 0$.

Equation (2.12) and (2.13) have unique solutions if the coefficients of α_0 and β_0 fulfill the requirements given by:

$$\int_{-1}^{0}\phi[(\bar{\rho}\tilde{\phi}_y)_y - G\frac{\bar{\rho}_y}{c^2}\tilde{\phi}]dy = 0 \tag{2.14}$$

$$\int_{-1}^{0}\phi[(\bar{\rho}\hat{\phi}_y)_y - G\frac{\bar{\rho}_y}{c^2}\hat{\phi}]dy = 0 \tag{2.15}$$

By inserting the R.H.S. of equation (2.12) into (2.14) and the R.H.S. of equation (2.13) into (2.15), we obtain in the last case:

$$\int_{-1}^{0} \phi[-\bar{\rho}\phi - \frac{2\beta_0 G\bar{\rho}_y}{c^3}\phi]dy = 0 \tag{2.16}$$

From equation (2.11) we have that:

$$\frac{G\bar{\rho}_y}{c^2}\phi = (\bar{\rho}\phi_y)_y \tag{2.17}$$

By inserting equation (2.17) into (2.16) and use partial integration with the given boundary conditions we obtain:

$$\begin{aligned}
\int_{-1}^{0} [-\bar{\rho}\phi^2 - \frac{2\beta_0 G\bar{\rho}_y}{c^3}\phi^2]dy = 0 \\
-\int_{-1}^{0} \frac{2\beta_0 G\bar{\rho}_y}{c^3}\phi^2 dy = \int_{-1}^{0} \bar{\rho}\phi^2 dy \\
-\int_{-1}^{0} 2\beta_0 \frac{(\bar{\rho}\phi_y)_y}{c}\phi dy = \int_{-1}^{0} \bar{\rho}\phi^2 dy \\
-2\beta_0 \frac{\bar{\rho}\phi_y}{c}\phi\Big|_{-1}^{0} + \int_{-1}^{0} 2\beta_0 \frac{\bar{\rho}\phi_y^2}{c} dy = \int_{-1}^{0} \bar{\rho}\phi^2 dy
\end{aligned} \tag{2.18}$$

Since the first term is zero when inserting the boundary conditions we obtain the following:

$$2\beta_0 \int_{-1}^{0} \bar{\rho}\phi_y^2 dy = c\int_{-1}^{0} \bar{\rho}\phi^2 dy \tag{2.19}$$

A similar relationship can be given for equation (2.14). For $\epsilon = \mu = 1$, the constants of α_0 and β_0 are then given as:

$$\alpha_0 = \frac{3c}{2}\frac{\int_{-1}^{0} \bar{\rho}\phi_y^3 dy}{\int_{-1}^{0} \bar{\rho}\phi_y^2 dy} \tag{2.20}$$

$$\beta_0 = \frac{c}{2}\frac{\int_{-1}^{0} \bar{\rho}\phi^2 dy}{\int_{-1}^{0} \bar{\rho}\phi_y^2 dy} \tag{2.21}$$

Two-layer interface

We now look at an example where we have a sharp pycnocline (two-layered fluid). The height and density of the upper layer is given as h_1, ρ_1 respectively and the lower layer as h_2, ρ_2. By putting $\epsilon = \mu = 1$ and use the assumption that $\frac{\rho_2 - \rho_1}{\rho_2} << 1$, we obtain:

$$\alpha_0 = -\frac{3}{2}\frac{c_0(\rho_1 h_2^2 - \rho_2 h_1^2)}{h_1 h_2(\rho_2 h_1 + \rho_1 h_2)} \simeq -\frac{3}{2}\frac{c_0(h_2 - h_1)}{h_1 h_2} \tag{2.22}$$

$$\beta_0 = \frac{1}{6}\frac{c_0 h_1 h_2(\rho_1 h_1 + \rho_2 h_2)}{\rho_2 h_1 + \rho_1 h_2} \simeq \frac{1}{6} c_0 h_1 h_2 \tag{2.23}$$

$$c_0^2 = \frac{g h_1 h_2(\rho_2 - \rho_1)}{\rho_2 h_1 + \rho_1 h_2} \simeq \frac{g' h_1 h_2}{h_1 + h_2} \tag{2.24}$$

where $g' = \frac{g(\rho_2 - \rho_1)}{\rho_2}$ is the reduced acceleration due to gravity in the two-layered case.

2.2 Weakly nonlinear solitary waves

KDV soliton, stratified ocean

We are now turning our attention towards KdV solitons in a stratified fluid. When there is balance between the nonlinearity and dispersion in equation (2.10), we have a solitary wave solution of permanent form. Using the longest mode, we then obtain:

$$A_0 = a_0 \operatorname{sech}^2\left(\frac{x - ct}{\lambda}\right) \tag{2.25}$$

where $c = c_0 + \Delta c$ and Δc is the excess velocity, a_0 is the amplitude. The coefficients are given as:

$$\frac{1}{\lambda^2} = \frac{a_0 \alpha_0}{12 \beta_0} \tag{2.26}$$

$$\Delta c = \frac{a_0 \alpha_0}{3} \tag{2.27}$$

where α_0, β_0 and c_0 are given as in equation (2.22), (2.23) and (2.24). β_0 is always a positive quantity, while α_0 can be both positive and negative depending on the stratification $\bar{\rho}$. The product $a_0 \alpha_0$ is however always positive.

To find the wavelength λ and wave excess speed Δc we need to solve equation (2.11). This equation can be rewritten to the Taylor-Goldstein equation. We start by inserting $G = gh/U^2$ into equation (2.11):

$$(\bar{\rho}\phi_y)_y - \frac{gh\bar{\rho}_y}{U^2 c^2}\phi = 0 \tag{2.28}$$

Next, we use the relation $c^2 = c_0^2/U^2$. By inserting this and expanding the first derivative we obtain:

$$\bar{\rho}_y \phi_y + \bar{\rho}\phi_{yy} - \frac{gh\bar{\rho}_y}{c_0^2}\phi = 0 \tag{2.29}$$

A change of variable is performed to simplify the equation with $y = z/H$. This changes the boundary conditions to $\phi(0) = \phi(-H) = 0$. We then get:

$$h^2\bar{\rho}_z\phi_z + \bar{\rho}\phi_{zz}h^2 - \frac{gh^2\bar{\rho}_z}{c_0^2}\phi = 0 \tag{2.30}$$

where the first term is assumed small and neglected. The equation known as the Taylor-Goldstein equation is then created:

$$\phi_{zz} + \frac{N^2}{c_0^2}\phi = 0, \quad \phi = 0 \quad for \quad z = 0, -H \tag{2.31}$$

Here N is the Brunt-Vaisala frequency defined as:

$$N^2 = -\frac{g\bar{\rho}_z}{\bar{\rho}} = -\frac{g}{\bar{\rho}}\frac{\partial\bar{\rho}}{\partial z} \tag{2.32}$$

We are now looking for an expression for the linear wave celerity. This can be found by only considering the first mode for equation (2.31), and applying the energy principle:

$$\phi_{zz}\phi_z + \frac{N^2}{c_0^2}\phi\phi_z = 0 \tag{2.33}$$

$$\frac{1}{2}\frac{d}{dz}(\phi_z^2) + \frac{N^2}{c_0^2}\frac{d}{dz}\frac{1}{2}(\phi)^2 = 0 \tag{2.34}$$

$$c_0^2 = -\frac{\int_{-H}^{0} N^2(\phi^2)_z dz}{\int_{-H}^{0}(\phi_z^2)_z dz} \tag{2.35}$$

Equation (2.35) gives us an additional way of finding the linear wave speed, that can be used for both two- and three-layered fluids.

KdV soliton on an interface

Several KdV models on an interface have been used to study weakly nonlinear interface waves (Keulegan, 1953 [26]; Long, 1956 [31]; Koop and Butler, 1981 [27]; Segur and Hammack, 1982 [37]). We look at the case where $\rho_2 > \rho_1$, where the upper layer is numbered 1 and the lower layer 2. Keulegan (1953) and Long (1956) looked at interfacial waves in a two-layered fluid assuming that the waves are long, the amplitude small compared to the total depth $kh << 1$ and $a/H << 1$ where k is the wavenumber and including weak dispersion. Then, as presented in Long (1956) [31], the coefficients of a solitary wave are given as:

$$\eta(x-ct) = -a\,\mathrm{sech}^2[(x-ct)/\lambda] \tag{2.36}$$

$$\frac{c^2}{c_0^2} - 1 = a\frac{\rho_2 h_1/h_2 - \rho_1 h_2/h_1}{\rho_2 h_1 + \rho_1 h_2} \tag{2.37}$$

$$\lambda^2 = \frac{4h_2^2 h_1}{3a}\frac{\rho_1/\rho_2 + h_2/h_1}{1-\rho_1 h_2^2/(\rho_2 h_1^2)} \tag{2.38}$$

The approximations made are valid for $\frac{\rho_2-\rho_1}{\rho_2} << 1$ and with c_0 given from equation (2.24). By looking at the equation for the excess velocity, we see that the amplitude a_0 is positive for $\rho_2 h_1^2 - \rho_1 h_2^2 > 0$ and negative for $\rho_1 h_2^2 - \rho_2 h_1^2 < 0$. The fluid velocity at the maximum depression (assuming $a_0 < 0$) of the wave can be obtained by KdV theory, which gives us the velocity profile in the upper layer for $-h_1 < y < 0$:

$$\frac{u_1(x=ct,y)}{c_0} \simeq \left[-\frac{\hat{\eta}}{h_1}\left(1+\frac{\Delta c}{c_0}\right) - \frac{\hat{\eta}^2}{h_1^2} - \frac{h_1\hat{\eta}''}{6} - \frac{h_1(\hat{\eta}')^2}{3} + \frac{\hat{\eta}'' y^2}{2h_1}\right]_{x=ct} \tag{2.39}$$

and for $-(h_1+h_2) = -H < y < -h_1$

$$\frac{u_2(x=ct,y)}{c_0} \simeq \left[-\frac{\hat{\eta}}{h_2}\left(1+\frac{\Delta c}{c_0}\right) - \frac{\hat{\eta}^2}{h_2^2} - \frac{h_2\hat{\eta}''}{6} - \frac{h_2(\hat{\eta}')^2}{3} + \frac{\hat{\eta}''(y+H)^2}{2h_2}\right]_{x=ct} \tag{2.40}$$

where we have neglected terms of $\mathcal{O}(a_0^3)$.

Deep water equations

Benjamin (1967) [3] looked at the case when $h_2 \to \infty$, $kh_1 << 1$ and $a/h_1 << 1$. He presented a solitary wave with algebraic decay (equations 5.3 - 5.7 [3]), given as:

$$\eta = -\frac{a}{1+(x-ct)^2/\lambda^2} \tag{2.41}$$

$$\lambda = \frac{4\rho_2}{3\rho_1}\frac{h_2^2}{a} \tag{2.42}$$

$$c_0^2 = \frac{(\rho_2-\rho_1)gh_2}{\rho_2} \tag{2.43}$$

$$\frac{c^2}{c_0^2} - 1 = \frac{3a}{4h_2} \tag{2.44}$$

Finite depth

Joseph (1977) [25] and Kubota et al. (1978) [28] provided a wave solution in a two-layer fluid of finite depth, achieving a connection between the KdV theory in shallow water with the Benjamin-Ono deep water equations. The finite depth theory was given for the

intermediate range $h_1/H << 1$, $kH = \mathcal{O}(1)$, $a/h_1 << 1$ (accounting for weak dispersion). The equations include both the KdV and Benjamin-Ono equations as limiting cases.

$$\eta(x-ct) = -\frac{a\,\mathrm{sech}^2(\frac{x-ct}{\lambda})}{1+\left(\tan\frac{H}{\lambda}\tanh(\frac{x-ct}{\lambda})\right)^2} \tag{2.45}$$

$$\lambda\cot\left(\frac{H}{\lambda}\right) = \frac{4\rho_2}{3\rho_1}\frac{h_2^2}{a} \tag{2.46}$$

$$\frac{c}{c_0} - 1 = \frac{h_2}{2H}\left(1 - \frac{2H}{\lambda}\cot\frac{2H}{\lambda}\right) \tag{2.47}$$

$$c_0^2 = \frac{\rho_2-\rho_1}{\rho_2}gh_2 \tag{2.48}$$

Interfacial waves of maximal amplitude

For finite upper and lower layer heights h_1 and h_2, interfacial solitary waves have a theoretical upper bound for the wave speed c_{max} and amplitude a_{max} (Amick and Turner (1986) [2]). The equations for the maximum wave speed and amplitude are given by Amick and Turner as:

$$c_{max}^2 = \frac{g(h_1+h_2)(\rho_2-\rho_1)}{(\rho_1^{1/2}+\rho_2^{1/2})^2}, \tag{2.49}$$

$$a_{max} = \frac{h_2\rho_1^{1/2} - h_1\rho_2^{1/2}}{\rho_1^{1/2}+\rho_2^{1/2}} \tag{2.50}$$

In addition, Turner and Vanden-Broeck (1988) [40] found that the volume of the wave may become infinitely large within this limit.

2.3 Fully nonlinear model for two-layered fluid

To find the theoretical solutions for internal solitary waves, the internal wave model IW2 [36] is used. This program is based on a fully nonlinear time-stepping method for interfacial waves as demonstrated in Grue et al. (1997) [17], where the complex fluid velocities are obtained using Cauchy's theorem. The coordinate system is defined with the x-axis at the level of the interface in the far field and the y-axis pointing upwards. The upper layer is numbered 2 and the lower layer as 1.

The following figure shows an illustration of a one-layered fluid (used as a simplification), where we have defined a point z' in the fluid. We will first present integral equations based on a one-layered fluid and then expand to a two-layered fluid.

We work in the complex plane and define:

$$\beta(z) = \phi(x,y) + i\psi(x,y) \tag{2.51}$$

$$z = x + iy \tag{2.52}$$

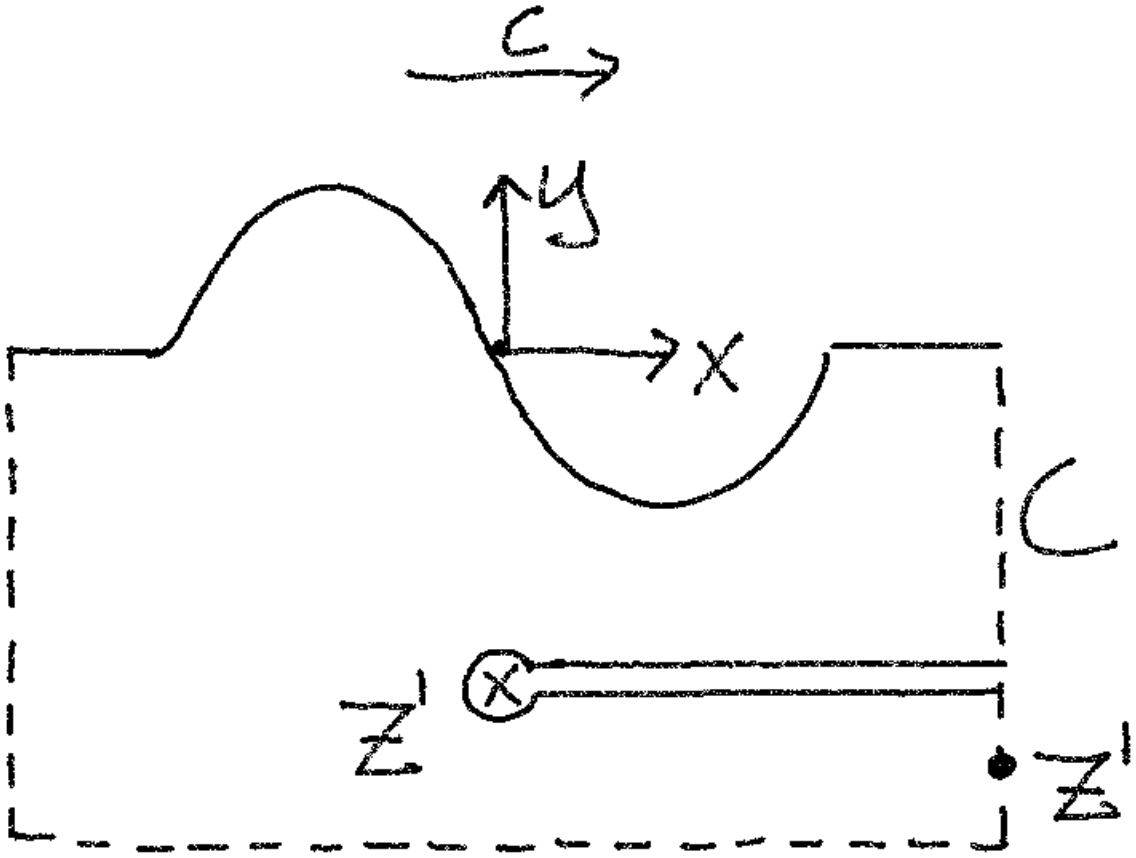

Figure 2.1: Illustration of a one-layered fluid

The complex velocity is defined as:

$$q(z) = \frac{d\beta}{dz} = u(x,y) - iv(x,y) \tag{2.53}$$

Where q is an analytical function. We then use Cauchy's theorem:

$$2\pi i q(z') = \oint_C \frac{q(z)}{z'-z} dz, \quad z' \in \Omega \tag{2.54}$$

On the boundary we get a similar result:

$$\begin{aligned} 0 = \oint_{C'} \frac{q(z)}{z'-z} dz + \oint_{C_\epsilon} \frac{q(z)}{z'-z} dz = \oint_{C'} \frac{q(z)}{z'-z} dz - \pi i q(z'), \qquad & z' \in \partial\Omega \\ \pi i q(z') = PV \int_I \frac{q(z)}{z'-z} dz, \qquad & z' \in \partial\Omega \end{aligned} \tag{2.55}$$

Where PV stands for principal value. Next step is to parameterize the interface I, $z = z(\xi)$.

Since we are working with stationary waves, we have the velocity field $q(z)-c$. Furthermore we define:

$$\begin{aligned} \gamma = (q(z)-c)\frac{dz}{d\xi} &= (q(z)-c)z_\xi \\ qz_\xi &= \gamma + cz_\xi \end{aligned} \tag{2.56}$$

Now, we multiply our integral with z'_ξ and use $dz = z_\xi d\xi$:

$$\begin{aligned} \pi i q(z')z'_\xi &= z'_\xi PV \int_I \frac{q(z)z_\xi}{z'-z} d\xi \\ \pi i(\gamma' + cz'_\xi) &= z'_\xi PV \int_I \frac{\gamma + cz_\xi}{z'-z} d\xi \end{aligned} \tag{2.57}$$

We then use the fact that $z_\xi = x_\xi + iy_\xi$ and insert into our integral equation:

$$\pi i(\gamma' + cx'_\xi + icy'_\xi) = PV \int_I \left(\frac{z'_\xi}{z'-z}\right)(\gamma + cx_\xi + icy_\xi)d\xi \tag{2.58}$$

By looking at the imaginary part we then get:

$$\pi(\gamma' + cx'_\xi) = PV \int_I Re\left(\frac{z'_\xi}{z'-z}\right) cy_\xi d\xi + \int_I Im\left(\frac{z'_\xi}{z'-z}\right)(\gamma + cx_\xi)d\xi \tag{2.59}$$

To fulfill the boundary conditions we use the method of images and use the Green function:

$$G(x,y) = \frac{1}{z'-z} + \frac{1}{z^* - z' - 2ih} \tag{2.60}$$

Here the asterix (*) stands for complex conjugate. By adding the image we get similar integrals, but without the principal value since the image is situated outside the domain of singularity.

The integrals for a one- and a two-layered fluid are very similar. The only difference is the sign of the LHS and we use the local fluid velocities. We then have the two following equations, one for each layer:

$$\begin{aligned} \pi(\gamma'_1 + cx'_\xi) =& PV \int_I Re\left(\frac{z'_\xi}{z'-z}\right) cy_\xi d\xi - \int_I Re\left(\frac{z'_\xi}{z^* - 2ih_1 - z'}\right) cy_\xi d\xi \\ &+ \int_I Im\left(\frac{z'_\xi}{z'-z} + \frac{z'_\xi}{z^* - 2ih_1 - z'}\right)(\gamma_1 + cx_\xi)d\xi, \quad z' \in I \end{aligned} \tag{2.61}$$

$$
\begin{aligned}
-\pi(\gamma_2' + cx_\xi') =& PV\int_I Re\left(\frac{z_\xi'}{z'-z}\right)cy_\xi d\xi - \int_I Re\left(\frac{z_\xi'}{z^*+2ih_2-z'}\right)cy_\xi d\xi \\
&+ \int_I Im\left(\frac{z_\xi'}{z'-z} + \frac{z_\xi'}{z^*+2ih_2-z'}\right)(\gamma_2 + cx_\xi)d\xi, \quad z' \in I
\end{aligned}
\tag{2.62}
$$

From the Bernoulli equation we get:

$$
\begin{aligned}
&p + \frac{1}{2}\rho\vec{v}^2 + \rho gy = p_\infty + \frac{1}{2}\rho\vec{v}_\infty^2 + \rho gy|_{y=\infty} \\
&\frac{1}{2}\rho q^2 + \rho gy = \frac{1}{2}\rho c^2 \\
&\frac{1}{2}\rho(q^2 - c^2) + \rho gy = 0
\end{aligned}
\tag{2.63}
$$

The tangential velocities at I are determined by $\frac{\gamma_1}{|z_\xi|} = \frac{q_1 z_\xi}{|z_\xi|}$ and $\frac{\gamma_2}{|z_\xi|} = \frac{q_2 z_\xi}{|z_\xi|}$. Inserting this into Bernoulli and demand continuity of the pressure at the interface, we get:

$$
\frac{1}{2|z_\xi|^2}(\gamma_1^2 - \mu\gamma_2^2) - \frac{1}{2}(1-\mu)c^2 + (1-\mu)gy = 0, \quad at\ I \tag{2.64}
$$

where $\mu = \frac{\rho_2}{\rho_1}$ and g denotes acceleration due to gravity.

Numerical procedure

Due to symmetric wave profiles with respect to x = 0, we get the relation $z(-x) = -z^*(x)$. We define I_+ that denotes the part of I where $x \geq 0$. This results in the following equations as presented by Grue et al. (1999) [18]:

$$
\begin{aligned}
&\pi(\gamma_1' + cx_\xi') = PV\int_{I_+} Re\left(\frac{z_\xi'}{z'-z}\right)cy_\xi d\xi - \int_{I_+} Re\left(\frac{z_\xi'}{z'+z^*}\right)cy_\xi d\xi \\
&- \int_{I_+} Re\left(\frac{z_\xi'}{z^*-2ih_1-z'} + \frac{z_\xi'}{z+2ih_1+z'}\right)cy_\xi d\xi \\
&+ \int_{I_+} Im\left(\frac{z_\xi'}{z'-z} + \frac{z_\xi'}{z'+z^*} + \frac{z_\xi'}{z^*-2ih_1-z'} - \frac{z_\xi'}{z+2ih_1+z'}\right)(\gamma_1 + cx_\xi)d\xi
\end{aligned}
\tag{2.65}
$$

$$
\begin{aligned}
&-\pi(\gamma_2' + cx_\xi') = PV\int_{I_+} Re\left(\frac{z_\xi'}{z'-z}\right)cy_\xi d\xi - \int_{I_+} Re\left(\frac{z_\xi'}{z'+z^*}\right)cy_\xi d\xi \\
&- \int_{I_+} Re\left(\frac{z_\xi'}{z^*+2ih_2-z'} + \frac{z_\xi'}{z-2ih_2+z'}\right)cy_\xi d\xi \\
&+ \int_{I_+} Im\left(\frac{z_\xi'}{z'-z} + \frac{z_\xi'}{z'+z^*} + \frac{z_\xi'}{z^*+2ih_2-z'} - \frac{z_\xi'}{z-2ih_2+z'}\right)(\gamma_2 + cx_\xi)d\xi
\end{aligned}
\tag{2.66}
$$

for z' at I_+.

The interface I_+ is then discretized by N points, $\xi = 1, 2, ..., N$. Next, we evaluate the principal value integrals by expanding the integrand in a series in the vicinity of the pole at $z' = z$, and then using the trapezoidal rule. The expansion is performed using the following relation by Dold and Peregrine (1985) [13]:

$$\frac{\Omega_\xi}{\Omega - \Omega'} = \frac{1}{\xi - \xi'} + \frac{\Omega_{\xi\xi}}{2\Omega_\xi} + \mathcal{O}(\xi - \xi') \tag{2.67}$$

We apply the trapezoidal rule to the regular integrals as well. In addition, we take into account the symmetry of y, γ_1 and γ_2 and the anti-symmetry of γ_ξ. The discrete version of equation (2.65) and (2.66) becomes:

$$\begin{aligned}\pi\Big(\gamma_1(\xi') + cx_\xi(\xi')\Big) =& c\sum_{\xi=1}^{N}\Big(A(\xi',\xi) - A_1(\xi',\xi)\Big)y_\xi(\xi) - cy_{\xi\xi}(\xi') \\ &+ \sum_{\xi=1}^{N}\Big(B(\xi',\xi) - B_1(\xi',\xi)\Big)\Big(\gamma_1(\xi) + cx_\xi(\xi)\Big)\end{aligned} \tag{2.68}$$

$$\begin{aligned}-\pi\Big(\gamma_2(\xi') + cx_\xi(\xi')\Big) =& c\sum_{\xi=1}^{N}\Big(A(\xi',\xi) - A_2(\xi',\xi)\Big)y_\xi(\xi) - cy_{\xi\xi}(\xi') \\ &+ \sum_{\xi=1}^{N}\Big(B(\xi',\xi) - B_2(\xi',\xi)\Big)\Big(\gamma_2(\xi) + cx_\xi(\xi)\Big)\end{aligned} \tag{2.69}$$

where:

$$A(\xi',\xi) + iB(\xi',\xi) = \begin{cases} z_{\xi\xi}/2z_\xi, & \xi = \xi' = 1 \\ \frac{1}{2}[z'_\xi/(z'-z) - \Big(z'_\xi/(z'+z^*)\Big)^*], & \xi = 1,\ \xi' > 1 \\ z'_\xi/(z'-z) - \Big(z'_\xi/(z'+z^*)\Big)^*, & \xi > 1,\ \xi' \neq \xi \\ z_{\xi\xi}/2z_\xi - \Big(z'_\xi/(z'+z^*)\Big)^*, & \xi > 1,\ \xi' = \xi \end{cases} \tag{2.70}$$

and for the image part we get:

$$\begin{aligned}&A_k(\xi',\xi) - iB_k(\xi',\xi) \\ &\quad= \begin{cases} \frac{1}{2}[z'_\xi/(z^* + 2(-1)^k ih_k - z') - \Big(z'_\xi/(-z + 2(-1)^k h_k - z')\Big)^*], & \xi = 1 \\ z'_\xi/(z^* + 2(-1)^k ih_k - z') - \Big(z'_\xi/(-z + 2(-1)^k h_k - z')\Big)^*, & \xi > 1 \end{cases}\end{aligned} \tag{2.71}$$

for $k = 1, 2$. We also discretize the dynamic boundary condition on the interface and obtain:

$$\frac{1}{2|z_\xi(\xi)|^2}\Big(\gamma_1^2(\xi) - \mu\gamma_2^2(\xi)\Big) - \frac{1}{2}(1-\mu)c^2 + (1-\mu)gy(\xi) = 0, \quad \xi = 1, 2, ..., N \tag{2.72}$$

Here $\mu = \rho_2/\rho_1$. The derivatives with respect to ξ are obtained by using a five-point Lagrangian differentiation formula. This first and second derivative of a function $f(\xi)$ are then given as:

$$f_\xi(\xi) = \frac{1}{12}(-f(\xi+2) + 8f(\xi+1) - 8f(\xi-1) + f(\xi-2)), \tag{2.73}$$

$$f_{\xi\xi}(\xi) = \frac{1}{12}(-f(\xi+2) + 16(f(\xi+1) - 30f(\xi) + 16(\xi-1) - f(\xi-2) \tag{2.74}$$

The boundary conditions are given as $y(N) = 0$ and $y_{\xi\xi}(N) = 0$. A final requirement is for the horizontal tangent at x(N) which gives $y_\xi(N) = 0$. This gives us 3N equations for 3N + 1 unknowns, $\gamma_1(\xi)$, $\gamma_2(\xi)$, $y(\xi)$ and c. In order to close the set of equations, we either give the volume V or the amplitude a for the solitary wave as initial condition. The equations are then solved iteratively with a weakly nonlinear start guess.

IW2

IW2 is a numerical model for calculating stationary internal waves in a two-layered fluid and is developed by Per-Olav Rusaas [36]. The program is written in Matlab and solves a set of fully nonlinear equations (see section (2.3)) in an iterative way. The program uses solitary waves of permanent form and is modelled in a frame of reference moving with the wave speed c. The interface is therefore to be considered as "frozen", with a horizontal current in the far field with velocity -c. The layers are assumed homogenous, incompressible and inviscid, and the motion is irrotational.

The program is used by choosing your parameters inside *setpar.m*. An illustration of this function can be seen in figure (2.2). Here you can define the density of the upper and lower layer, their respective height, the wave amplitude, propagation speed, volume etc. The height of the upper and lower layer are scaled towards the upper layer. In IW2, the upper layer is numbered 2 and the lower layer 1. The program is then started by running *iw2.m*, which return the results in one single cell array of structs. The results can then be plotted by using the built-in post-processing tools found in the *postPlot* folder, which also includes functions for calculating and plotting streamlines and velocity profiles.

The struct returned by the solver includes all the results for the given input parameters. Plotting x towards y gives us the wave profile where both the x and y axis are dimensionless, y towards the upper layer height and x towards the linear wave propagation speed and the upper layer height. The solution is assumed symmetric. The model does not include instabilities that may develop. This means that the rear part of the wave remains unchanged even for large waves where Kelvin-Helmholtz instabilities have a large impact on the wave form (Grue et al. 1999 [18]). The wave front on the other hand remains an important quantity that should be reproduced by both the numerical and experimental work for all simulations. The relationship c/c_0 can be found directly in the *solI* struct. IW2 also comes with the possibility to calculate fluid velocities. This can be done at any point by using the function *hast()*. This function returns a new updated solution struct. The results can then be found in the solution struct named p_i where i is the number 1 for lower layer or 2 for upper layer.

```
function [fyspar,numpar]=setpar(fyspar,numpar)
% SETPAR - Sets the parametres that descripe the problem
%    [fyspar,numpar]=setpar(fyspar,numpar)

fyspar.Bgrensen  = 0;

% 1 gives KdV-start, 0 gives BO-start
fyspar.KdVstart = 1;

antall=8;
fyspar.y0tab     = [-0.31 -0.57 -0.84 -1.12 -1.33 -1.52 -1.67 -1.79];
fyspar.volumtab  = 0 * ones(1,antall);
fyspar.ctab  = 0     *ones(1,antall);
fyspar.rho1tab   = 1.047*ones(1,antall);
fyspar.rho2tab   = 0.999*ones(1,antall);
fyspar.h1tab     = 5.23     *ones(1,antall);
fyspar.h2tab     = 1        *ones(1,antall);

fyspar.lambda = 80;

numpar.fastI=0;
numpar.maxjac=15;
numpar.eps=1.0e-6;
numpar.toleranse=1.0e-10;
numpar.likdx=0;
numpar.N=64;
```

Figure 2.2: Illustration of *setpar.m* from the IW2 program in Matlab

The program is used as a comparison against both experimental and numerical results for the wave profile η, the propagation velocity c and velocities (u,w) plotted against the dimensionless amplitude.

CHAPTER 3

Methods

We will now give an introduction to the tools used in our study. This includes the numerical tool Basilisk and experiments performed in the hydrolab at UiO.

3.1 Basilisk

Basilisk is a free software used to solve partial differential equations on adaptive Cartesian grids. Basilisk contains a second order accurate finite volume solver for the Navier-Stokes equation, making it a good choice when dealing with internal waves. The code is developed by Stephane Popinet et al. and is the successor of Gerris. The code is developed for Linux and is written in C. Basilisk comes with an additional supported programming language "Basilisk C", which is an extension of C and is used to write code in Basilisk. This extension is created to make it easier to perform general operations in your own programs. The program comes with several solvers that are ready to use, such as Navier-Stokes, Saint-Venant, advection and more. The program has previously been used on several different problems such as the Indian Tsunami from 2004, bubbles rising in a large tank, measuring Kelvin-Helmholtz instabilities, atmospheric flows and much more.

Introduction

Installation

The program is downloaded from "www.basilisk.fr", which is a complementary website where you find all information that is necessary to install the program and start to use it. Here you find help from tutorials, examples, solvers, tests and more information. Basilisk also comes with its own user forum where users can ask questions to other users or even the developers of Basilisk. The program is installed in Linux. If you are using either Windows or Mac, Linux can be run by downloading Oracle VirtualBox and Ubuntu, to create a virtual desktop of Linux. The easiest way to install Basilisk is by using darcs to download the source code from the website. The tutorial found on the website gives a quick introduction on how to write your own code in Basilisk.

How to get started

The programming language used in Basilisk is based on C and is created to simplify standardized operations. To perform a task in Basilisk, you create an event. The main

event in each code is called *main*. The grid is always created as a quadratic domain where each side has length equal to 1. This domain can be stretched and modified by specifying the locked keyword L_0. The number of grid points are defined by N and the grid resolution is put equal in all directions for most solvers in Basilisk. This is always the case throughout our study on ISWs. The timestep is defined in each iteration to satisfy the Courant-Friedrichs-Lewy (CFL) condition. The origin of the coordinate system is specified in the vector *origin*. This vector specifies the bottom left corner of the coordinate system. The main function always ends with the keyword *run*, which starts the program. To perform operations during the simulation, you specify events. This can either be done for each iteration, each timestep or to your own chosen time. During a simulation, data can be saved to files as images, text files, movies or similar for post-processing.

One of the main advantages of using Basilisk is its ability to adapt the grid during a simulation, which can save both a lot of simulation time and computer memory. The grid can be refined either locally or more dynamically based on parameters such as the velocity, pressure, etc.

Numerical features

Adaptive grid in Basilisk

Basilisk uses a tree-structure to adapt to local refinement or coarsening. The tree-structure introduces a hierarchy between cells of different levels of refinement. Basilisk allows a difference of one level between two neighbouring cells, where the levels of refinement differs with a factor of two. In several dimensions this is equal to a refinement of n^2. Due to the difficulties with an uneven grid, Basilisk uses ghost cells that allows simple Cartesian stencil operations for cells near the resolution boundaries. The ghost cells work as virtual cells and are defined such that all cells have neighbours on the same level of refinement as seen in figure 3.1. The field values in the ghost cells are defined through interpolation of the original field values.

The tree-grid structure gives a convenient and effective structure to decide whether to refine or coarsen a grid cell. As an example we can introduce a signal f with an even number of evaluation points n, f_n. We then perform two operations. First, we use a downsampling operator D, which approximates f on a coarser grid

$$f_{n/2} = D(f_n) \tag{3.1}$$

Next, we use an upsampling operator U, which samples the coarsened signal back to f_n, defined as

$$g_n = U(f_{n/2}) \tag{3.2}$$

We now have two signals for the same number of elements that most often have the following property $f_n \neq g_n$. This means we can define the absolute error given as:

$$\chi_n^i = ||f_n^i - g_n^i||, \quad f_n \neq g_n \tag{3.3}$$

The downsampling operator in Basilisk is defined as a local volume averaging to obtain the field value for a corresponding coarser grid. This is an exact formulation since Basilisk uses a finite-volume formulation that defines grid cells representing averaged volume quantities. Since the solver is second order, we use a second order interpolation scheme

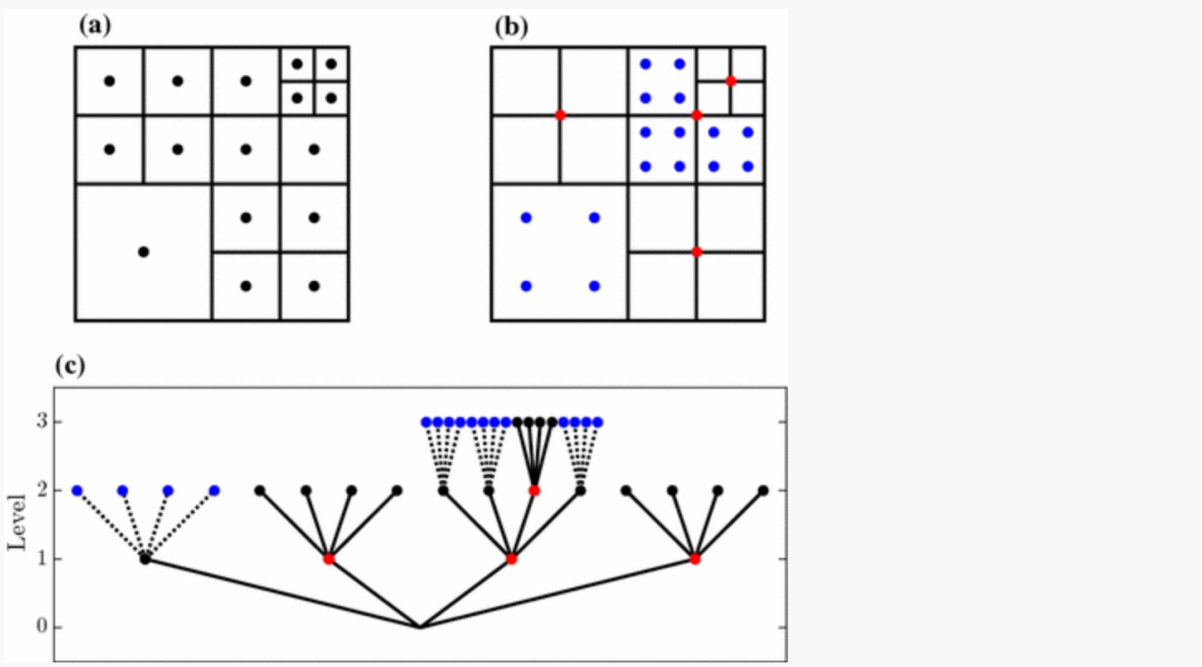

Fig. 2
Example of a tree-grid structure. The top row presents the spatial structure of the grid cells with varying levels of refinement (**a**) and the locations of two types of ghost points whose field values are defined by the downsampling (red dots) and upsampling (blue dots) operations (**b**, see text). The plot on the bottom row presents a corresponding tree representation of the various grid cells and ghost points at different levels (**c**)

Figure 3.1: *Figure 2* of Van Hooft et al. (2018) [23]

for the upsampling operator on the downsampled solution. When both operations are performed, we can check the relative error in each cell. The criterion for refinement or coarsening is then defined as

$$\text{The i'th grid cell is} \begin{cases} \text{too coarse}, & \chi_n^i > \zeta \\ \text{too fine}, & \chi_n^i < \frac{2\zeta}{3} \\ \text{just fine}, & \text{else} \end{cases}$$

where ζ is the threshold given by the user.

Additional information on the adaptive grid in Basilisk can be found in Van Hooft et al. (2018) [23].

Volume of fluid (VOF)

The volume of fluid method (VOF) is in computational fluid dynamics a numerical technique for tracking and locating the free surface or fluid - fluid interfaces. The method can be used for both a moving or stationary mesh to represent the evolution of the interface. VOF is an advection scheme, but it is not a standalone flow solving algorithm. VOF is therefore solved separately beside the Navier-Stokes equations, which describes the motion of the flow.

The method is based on a fraction function C. This is a scalar function that is defined as the volume of a computational grid cell. The scalar function C is defined as zero when a cell is empty and $C = 1$ when the cell is full. A cell can also have a value $0 < C < 1$ if there is a fluid interface in the cell. When using the VOF method, the free surface is not defined sharply, but distributed over the height of a cell. Therefore, local grid refinements have to be done to attain accurate results. Cells are refined if a cell contains a fluid interface $0 < C < 1$. All cells have to satisfy the following constraint, which says that the volume of the fluid is constant:

$$\sum_{m=1}^{n} C_m = 1 \tag{3.4}$$

The density in each cell are defined by.

$$\rho = \sum_{m=1}^{n} \rho_m C_m \tag{3.5}$$

Here n denotes the number of fluids. To ensure stability of the solution, the CFL condition must be smaller than 0.5.

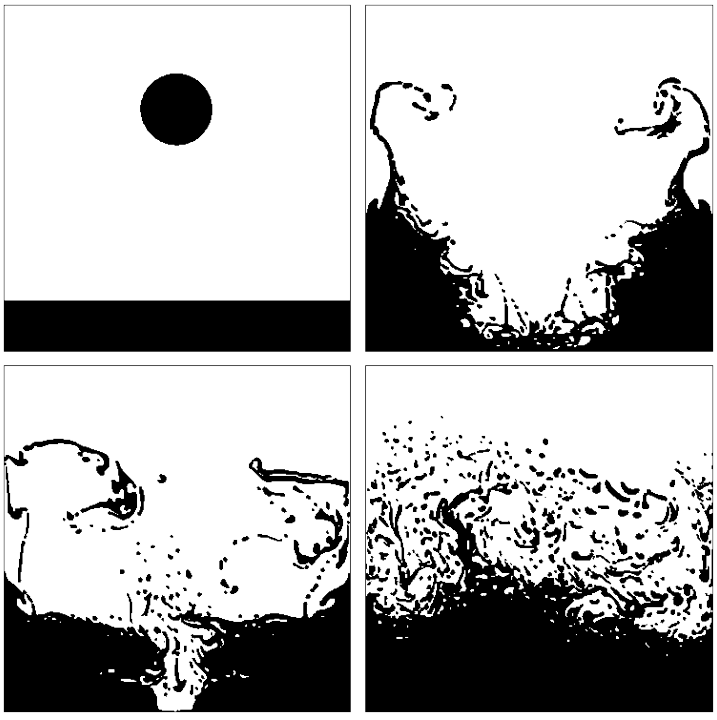

Figure 3.2: Illustration of a fluid simulation using VOF

Two-phase flow

A two-phase flow is in fluid mechanics a flow of gas and liquid. A two-phase flow can occur in several forms:

(a) Transient two-phase flow, a flow transitioning from pure liquid to vapor due to external heating

(b) Separated two-phase flow, which is the form we use for internal waves.

(c) Dispersed two-phase flow, where one phase is present in the form of droplets or bubbles in a continuous carrier phase.

In Basilisk, the two-phase flow is used by defining the density ρ_i and dynamic viscosity μ_i, where $i = 1, 2$, 1 for the upper layer and 2 for the lower layer. The interface between the two layers is then tracked with VOF. Basilisk uses arithmetic averages by default for both the density and viscosity, but this can be overloaded by the user.

Navier-Stokes centered

When solving for internal waves in Basilisk, we use the incompressible, variable-density Navier-Stokes equations:

$$\frac{\partial u}{\partial t} + \nabla \cdot (u \times u) = \frac{1}{\rho}[-\nabla p + \nabla \cdot (2\mu D)] + a \tag{3.6}$$

Together with the continuity equation

$$\nabla \cdot u = 0 \tag{3.7}$$

The deformation tensor is given as

$$D = \frac{\nabla u + (\nabla u)T}{2} \tag{3.8}$$

To solve for advection we use the Bell-Collela-Glaz advection scheme, which is second order accurate and an implicit viscosity solver. If we use embedded boundaries, a different scheme is used for the viscosity.

The variables used are the centered pressure and velocity field, p and u. The centered vector field g contains pressure gradients and acceleration terms. For numerical purposes we also define an auxiliary face velocity field *uf* and an associated centered pressure field *pf*. The viscosity is defined as the dynamic viscosity μ and the default value is zero. The acceleration a is given as a face field and default is zero. A boolean variable *stokes* decides whether to omit the velocity advection term $\nabla \cdot (u \times u)$. This is helpful when working with Stokes flows, where inertia is negligible compared to viscosity.

The pressures are never dumped in the solver. The timestep in each iteration is controlled by the CFL condition, applied to the face centered velocity field *uf*. In two dimensions, the CFL condition is given as:

$$C = \frac{u_x \Delta t}{\Delta x} + \frac{u_y \Delta t}{\Delta y} \leq C_{max} \tag{3.9}$$

The maximum allowed value C_{max} is given by the user or defined in imported solvers. For explicit solvers, $C_{max} = 1$ is common to use. Implicit are often more stable than explicit solvers and larger values of C_{max} may be tolerated. When solving for internal waves in this project, the maximum value is $C_{max} \leq 0.5$, to ensure stability when using the VOF method.

Embedded boundaries

Embedded boundaries (EB) are a numerical method that can be used to include complex geometries in a numerical grid. In this project, embedded boundaries are used to create a sloping bottom of constant angle (figure 3.3). In Basilisk, the EB method uses a Cartesian grid and the boundary is allowed to "cut" cells. Each cell is labeled. They can either be *regular*, *cut* or *covered*. A regular cell is a normal grid cell, with no boundary present. The cut cell contains a value between 0 and 1 and is used to create a slope. Finally, the covered label tells us that the cell is not to be included in the grid. The EB method can generate complex geometries quickly and robustly due to its relatively simple grid generation technique. Combined with an adaptive grid, embedded boundaries can give precise results of flow around complex geometries. The problem with using EB is that it can produce arbitrarily small cut cells in the domain, that can have a significant impact on the stability and robustness of traditional finite-volume methods. An example of an embedded boundaries grid combined with adaptive grid refinement can be seen in figure (3.3).

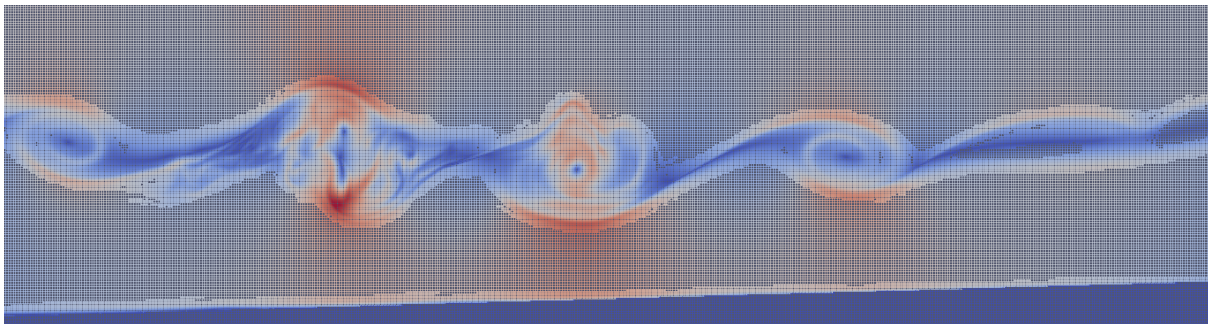

Figure 3.3: Illustration of velocity field with visible grid lines created with embedded boundaries and adaptive grid in Basilisk

Internal waves in Basilisk

In this project, Basilisk is used to create internal waves in 2D. This is done by using the built-in Navier-Stokes centered solver and include a two-phase simulation. The two-phase function uses VOF to define the interface. To be able to extract the position of the interface, we include a function called curvature, which returns the exact position of the density interface. A problem with using VOF arises if we want to solve for a three-layered fluid. Here the pycnocline starts to diffuse and the three-layered fluid gradually moves over to a two-layered fluid. Based on this, a modification on the two-phase solver was performed where the VOF method used to track the fluid interface got substituted with a passive tracer. This modification proved to be suitable for the operations performed in this study as the results compared well to both theory and experiments.

A wave tank was created in Basilisk by defining its length L_0, the origin of the coordinate system in *origin* and the number of grid points in each direction N. This creates initially a quadratic grid, but a rectangular wave tank was then created by removing the excess grid in the vertical direction using a function named *mask*. An imaginary gate was created at a position named x_0. The content of the wave tank was then defined by specifying a scalar named f, that were used to track the fluid and is defined as $0 \leq f \leq 1$. The upper layer is defined as $f = 1$ and the lower layer as $f = 0$. The density and viscosity are

defined by specifying the values for both the upper and lower layer. Intermediate values are then calculated from the volume fraction f. The acceleration term is given by the acceleration of gravity at $g = 9.81$. The acceleration term is initially created as a constant scalar. This means that it can only be overwritten by another constant scalar and not adjusted directly. The numerical parameters are initialized in an event called *main*. Here we also define the simulation length, the CFL criteria, the wanted tolerance, which we believe controls the residual for pressure, and the maximum allowed timestep DT.

All simulations are performed with a rigid lid at the upper boundary. This is a valid approximation since the movements in the vertical direction are considered small at the surface. The boundary conditions are given as no-slip on the bottom boundary and free slip on the vertical walls and the upper boundary. The horizontal velocity is also put to zero at the start of our simulation.

Grid adaption can be performed both locally or more dynamically based on the evolution of the simulation. Both approaches have been performed in this study. A weakness with local refinement proved to be an increase in the vortex shedding in the transfer from a fine to a coarser grid, resulting in similar behaviour as when a wave propagates over a step. This made it a poor choice when investigating the vortices that developed behind the propagating ISW. When using dynamic grid adaption, we changed the resolution based on the presence of a sloping bottom and the velocity field.

Embedded boundaries are included by adding *embed.h* to our program. The boundary is then created by defining a vector called ϕ. If $\phi < 0$ the grid point is considered outside the domain. The embedded boundaries method does at this point not work for variable viscosity. This means that all of our simulations including embedded boundaries have been solved with a constant viscosity. To include particles in our simulations we have included a function from Basilisk named *particles.h*. This function creates tracer particles that are advected using a forward Euler method or in 2D the split semi-implicit Euler method. This method is similar to Lagrangian particle tracking where a particle at initial position $\vec{x}_0$ is moved to its new position based on the local velocity field as $\vec{x} = \vec{x}_0 + \vec{v}\Delta t$. Several functions can be called to place the particles in the wave tank at the start of the simulation, either in a circular, quadratic or linear formation.

3.2 Experimental procedure

The experiments were performed in the hydrolab at UiO. We have used a 7m long wave tank with a width of 0.25m. A gate is situated x_0 m away from the start of the tank. To create internal waves, we fill the tank with water and supply with salt to create a density of approximately $\rho_2 = 1.047\frac{g}{cm^3}$. Next, we gently fill up a layer of fresh water on the top with density $\rho_1 = 0.999\frac{g}{cm^3}$. To measure the density, we use a Density Meter DE 40 Mettler Toledo that gives a measure of the water based on its weight with up to four decimal precision. The height of the upper layer and the initial volume behind the gate are varied to achieve ISWs with different non-dimensional amplitudes. When adding the upper layer, we use a technique involving wetted sponges to make the process as gently as possible, since we want a sharp pycnocline. This process can last up to one hour depending on the thickness of the upper layer. When this is done, the gate is lowered gently to make sure the layers do not mix. Next, we add more fresh water behind the

gate. This extra added volume approximately becomes the total volume of the internal wave. When adding the extra water behind the gate, some salt water travels to the other side of the gate by moving through a small opening at the bottom of the paddle. To start the experiment, the paddle is raised and an internal solitary wave of depression is quickly established and starts propagating. Our main objective is to create only one solitary wave. This can be done by carefully adjusting the gate position and the height of the extra water behind the gate.

To track the wave, we use particles of pliolite VTAC, a granular material used in white paint, due to its good reflective properties and density of approximately $1.0228\frac{g}{cm^3}$. The particles are created by crushing and sieving the pliolite to the wanted size. Next, the particles are wetted by using a rinse aid and then washed to remove surface tension. If this process is done correctly we obtain particles that effectively are naturally buoyant throughout the water column. The particle size used is in the range from $400 - 500\mu m$.

When creating a three-layered fluid, we start by making a two-layered fluid, which then is left to diffuse for approximately 16 hours. The density field is then measured using probes to measure the conductivity of the water throughout the water column. The probes are connected to a voltmeter, which returns the voltage of each wanted height of the water column. The results are then converted to density to give us the density profile of the three-layered fluid.

CHAPTER 4

Results

Definitions used in Basilisk

Before we present the results, we will give a clarification of the definitions we have used throughout the study. In addition, we will explain how the different numerical studies can be used to build a better understanding of the behaviour of internal solitary waves.

When a numerical simulation has been performed, our first objective is to check that the numerical wave compares good to analytical theory. If this is not the case, the numerical results can not be used as they do not represent real world physics. In order to represent a wave profile from Basilisk, a density field is returned for the entire wave tank. We have chosen to represent the wave profile by using the density lines (isolines) following the salt water. This gives a good representation of the wave width when we compare it to fully nonlinear theory. When using the isolines following the fresh water, the wave width becomes too narrow in comparison to theory. One more option would be to choose a mid-value for the density, but this results in fewer grid points satisfying our criteria, making it harder to represent our wave profile in a good way. We have used the smoothing function in Matlab on the data to remove small distractions. The wave amplitudes are given as the maximal displacement for the isoline following the salt water. The numerical program IW2 programmed by P. O. Rusaas ([36]) shows that the isolines get compressed around the wave crest. This means that if we choose a different isoline, the non-dimensional amplitude will change.

We have in this study used the upper layer thickness to make length scales dimensionless. This is easy when we solve for a two-layered fluid but can be defined in different ways for a three-layered fluid. We have therefore chosen to use the length from the surface to the middle of the pycnocline $\tilde{h}_1 = h_1 + h_2/2$ as the scaling factor.

The wave profiles, the velocities in the upper layer and the horizontal velocity at the maximal displacement of the wave, have throughout this study been calculated by taking a snapshot at a given time and investigate the results. The wave celerity has been calculated by using the crest position in two consecutive snapshots and divide by the difference in time. All other figures are calculated by using data evolving with time. The linear wave speed c_0 has been calculated for both a two- and three-layered fluid. In most of our results, the two-layered linear wave speed has been used to perform comparisons with previous studies. If the linear wave speed of a three-layered fluid has been used, it is highlighted.

In our study, we have performed simulations for both a two- and three-layered fluid. The motivation for this comes from results presented by Grue et al. (1999) [18]. They showed that the shear instability evolving in the interface between the upper and lower layer makes the tail of the wave profile wider compared to fully nonlinear theory. We have therefore decided to perform three-layered simulations in order to decrease the Kelvin-Helmholtz instability and by this better retain the wave profile also for larger waves.

The additional volume of fresh water added behind the gate is important when deciding the magnitude of our wave. When we increase the nonlinearity of our problem by increasing H/h_1, a larger volume is necessary in order to create a max wave. A max wave is a wave that fulfills the following requirement: $\frac{a+h_1}{H} \approx \frac{1}{2}$. The initial volume necessary to create a wave of a given amplitude is found using the numerical program IW2 [36]. A single solitary wave can be made by carefully adjusting the gate position and the initial amplitude height h_0. When we start our simulations for the largest waves, the distance between the fresh water and bottom of the wave tank is small behind the gate. This creates some large vortices that get lifted high up into the water column. When looking at the global instability, it is therefore important to chose a point in the wave tank where the instabilities get created due to the wave motion and not the initial condition. We have chosen to use the same point as Carr et al. (2008) [8] at $x/H \approx 7.6$. This is sufficient to avoid vortices created from our initial condition, unless we include a sloping bottom. In these conditions, the initial motion travels further with the wave and may result in an increased global instability in our measurement point. We have in this case included a second measurement point.

We have in this work included a study where we investigate how a change in the pycnocline thickness affects the velocity profiles at the bottom of the wave tank, in addition to the wave profile itself. This study gives us a better understanding of how different wave profiles affect the fluid motion and the global instabilities.

In order to validate our numerical results, two questions need to be answered. Does the results relate to a physical interpretation and does it compare well to similar experiments? To be able to answer our first question, we need to perform a lot of simulations from different angles in order to build up an understanding of how different parameters affect the solution. In addition, it is necessary to read up on similar experiments done before to build a good understanding of the problem. To answer our second question, we have several possibilities. We can compare our results to analytical theory. In our case, we have used fully nonlinear theory and some weakly nonlinear KdV theory. Another opportunity is to compare numerical results to experiments. This has been done with a comparison to experiments performed by Carr et al. (2008) [8] and experiments performed in the hydrolab at UiO. A final possibility is to use the numerical model itself as validation. This is done by performing several simulations where small adjustments are made on either the timestep, resolution or the tolerance. Basilisk uses an iterative Navier-Stokes solver. By adjusting these parameters, we can check whether our numerical results converge. If convergence is achieved, we know that numerical errors are kept to a minimum. This means that eventual errors lay in the numerical solver itself or in the usage of it.

In order to capture the global instability from the bottom of the wave tank, a fine numerical resolution has to be used. If this criteria is invalidated, no global instability is observed. The simulations in this study have been performed using Ubuntu on a VM

VirtualBox created by Oracle. This creates a virtual laptop on your computer where additional operational systems can be installed. One of the problems with performing simulations on a virtual machine is that the total allocated memory is small, which gives restrictions on the total number of nodes used. The maximum amount of nodes used in the beginning of our adaptive simulations are approximately 0.7 million nodes, but since we use an adaptive grid, the number of grid points are a bit higher.

4.1 Validation and verification of Basilisk

When you work on highly nonlinear problems it is difficult to tell whether your results are correct. Analytic theory is good for linear cases, but once the equations become nonlinear they soon gets much harder to solve. We have therefore made several tests to validate if the results produced by Basilisk can be used in our study.

In the first test, we looked at the internal wave properties produced by Basilisk and compared them to theory. We then had to use small amplitudes to be closer to the linear case and have a good reference for comparisons. We have chosen to use both weakly nonlinear KdV theory and fully nonlinear theory in our comparisons. For the fully nonlinear theory we used a program named *IW2* [36] created by P. O. Rusaas. In this comparison we looked at the wave profile η, wave propagation speed c, the horizontal wave velocity u and the wave width at $\eta/2$.

If we increase the wave amplitude, it is more difficult to verify the results. This is why we chose to do a reproduction of experiments performed by Carr et al. [8]. In 2008, Carr et al. [8] made experiments looking at the boundary layer induced by an ISW of depression in a stable stratified shallow water with use of PIV. The experiments proved that a wave-induced boundary layer separates in the adverse pressure gradient region aft of the wave, which induces a reverse flow along the bottom. If the reverse flow was deep enough for a period, global instabilities could be observed. A reproduction of these results would therefore give a good reference to see the accuracy of our numerical model on a study with the same focus as us. We focus on the experiment known as *08.02.07* from [8].

Comparison between Basilisk, KdV theory and fully nonlinear theory

Our first validation test is to see how good Basilisk compares to both weakly nonlinear KdV and fully nonlinear theory. Comparisons have been made for the wave profile η, the horizontal velocity in the upper layer $u(z = h_1/2)$, the wave propagation speed c, the wave width evaluated at $\eta/2$ and the horizontal velocity $u(z)$ at the maximal displacement of the wave. We have used the VOF solver from Basilisk in our comparisons.

Wave profile

We start by comparing the wave profile for different wave amplitudes. The non-dimensional wave amplitude is given as $\frac{a}{h_1}$. We made eight simulations for different wave amplitudes, but will only present four of these, which is seen in table (4.1). h_0 is defined as the depth of the extra volume added behind the gate in meters.

h_0 (m)	0.025	0.10	0.15	0.207
$\frac{a}{h_1}$	0.29	1.11	1.50	1.67

Table 4.1: Numerical parameters, Basilisk

We can see from figure (4.1) that the wave profiles computed by Basilisk compares well to fully nonlinear theory for all wave amplitudes. The wave profile computed by Basilisk differs a bit in the rear of the wave. This is due to some dispersion that is present in all cases, but also Kelvin-Helmholtz instabilities that appear for the largest amplitudes. The dispersion could be avoided by adjusting the gate position relative to the initial height of the extra added fresh water behind the gate. We can see that KdV theory compares well to the other models for the lowest wave amplitude, but differs with increase in amplitude. This is also in agreement with work presented by Grue et al. (1999) [18], which found weakly nonlinear theory to be valid for dimensionless amplitudes up to $a/h_1 = 0.4$.

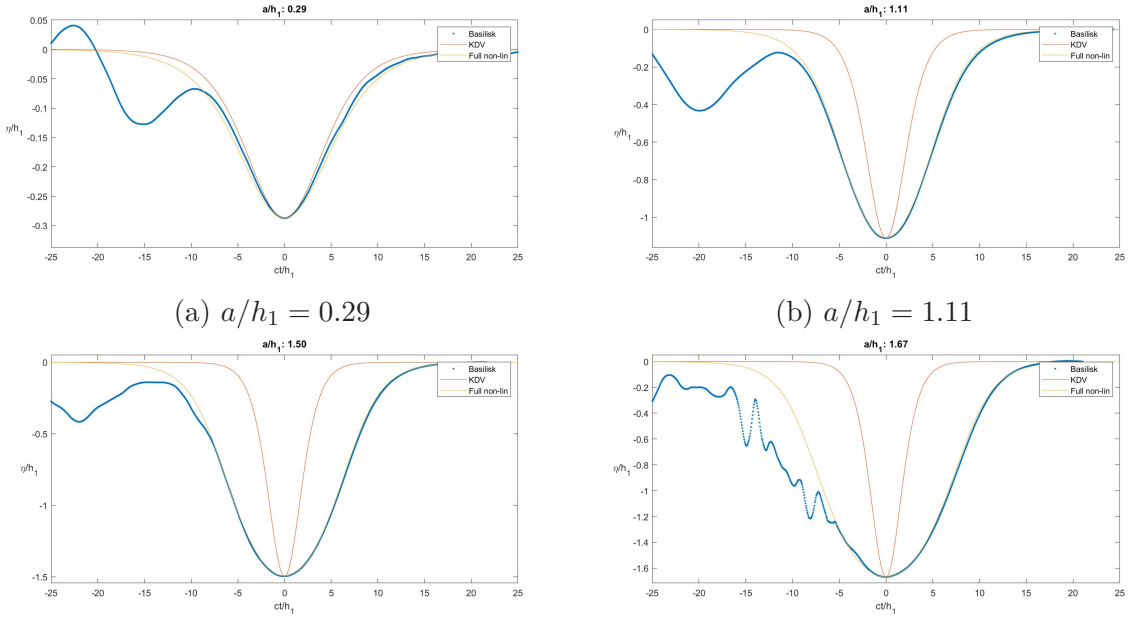

(a) $a/h_1 = 0.29$

(b) $a/h_1 = 1.11$

(c) $a/h_1 = 1.50$

(d) $a/h_1 = 1.67$

Figure 4.1: Wave profiles compared to KdV theory and fully nonlinear theory for different dimensionless wave amplitudes

Horizontal velocity

Next we look at the horizontal velocities in the middle of the upper layer at $u_1(h_1/2)$ and the horizontal velocity beneath the maximal displacement of the wave. Looking at the velocity in the upper layer, there is once more good agreement between Basilisk and the nonlinear theory, but with Basilisk slightly overestimating the fully nonlinear theory for the largest waves. Once more, we observe that the tail of the wave in figure d) differs from the fully nonlinear theory.

Moving over to the horizontal velocity profile $u(z)/c_0$ at the maximal displacement of the wave (figure 4.3), we see that Basilisk slightly overestimates the horizontal velocity compared to theory in the lower layer. This also occurs near the surface.

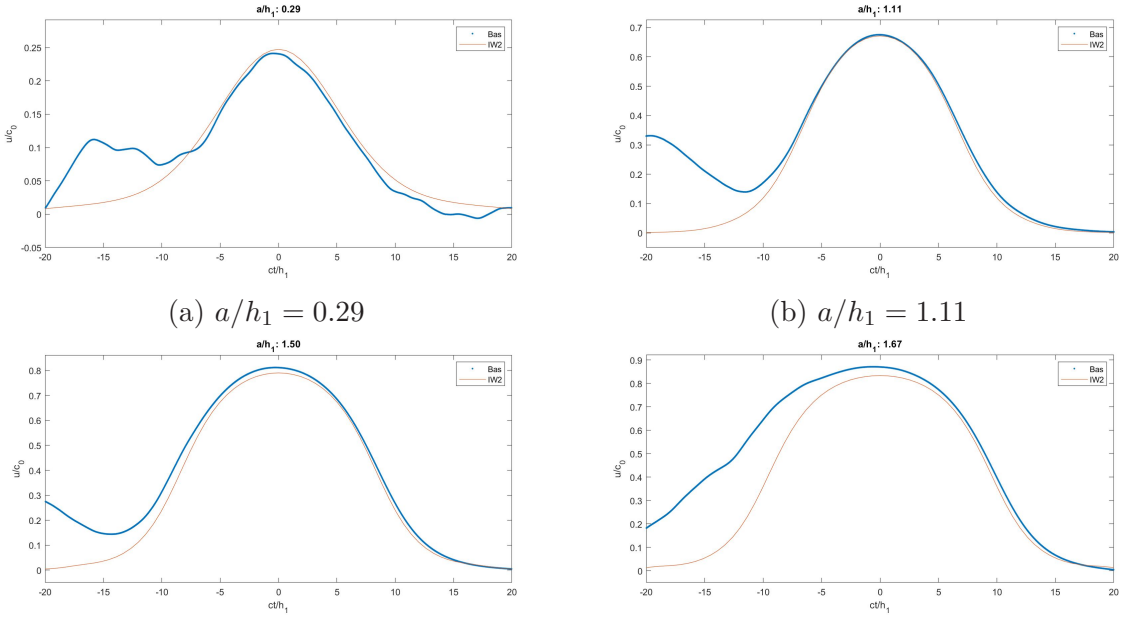

(a) $a/h_1 = 0.29$ (b) $a/h_1 = 1.11$

(c) $a/h_1 = 1.50$ (d) $a/h_1 = 1.67$

Figure 4.2: Horizontal velocity in upper layer $u_1(h_1/2)$ compared to fully nonlinear theory for different dimensionless wave amplitudes

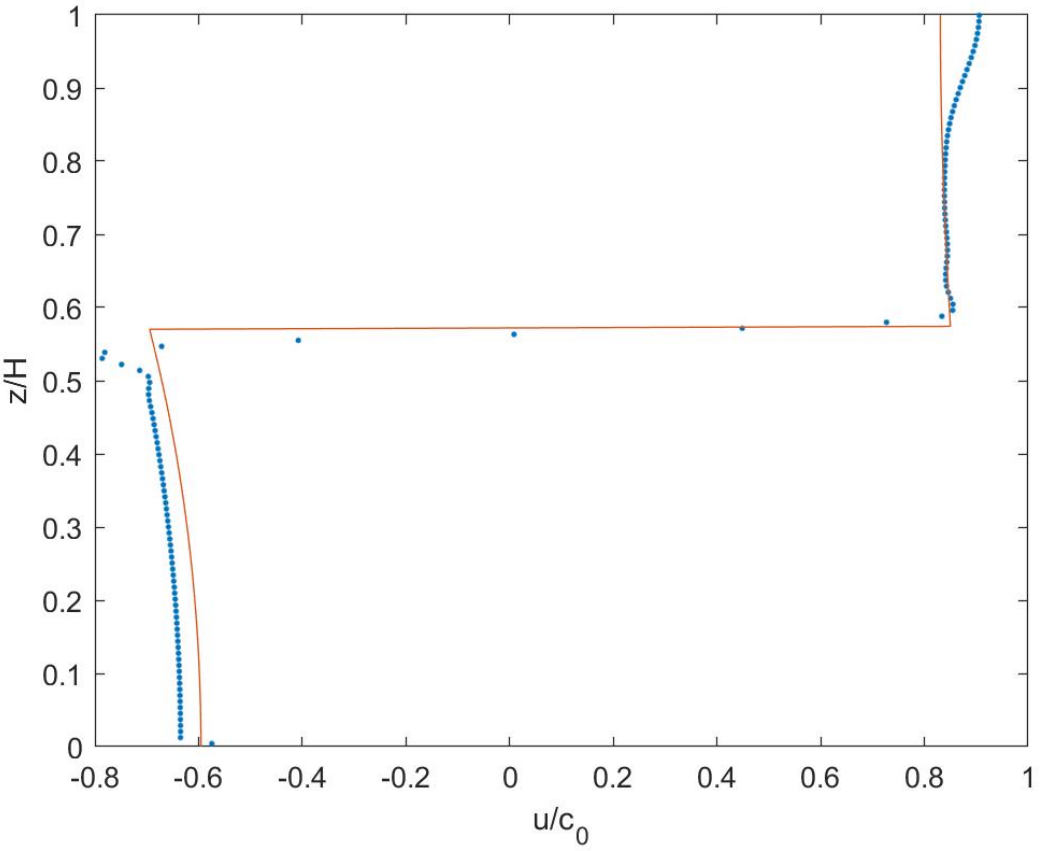

Figure 4.3: Horizontal velocity profile $u(z)/c_0$ vs non-dimensional height z/H at the maximal displacement of the wave

Comparison for wave propagation speed and wave width

At last we look at a comparison between the wave propagation speed and the wave width at $\eta/2$ for different amplitudes. The propagation speed compares very well to fully nonlinear theory for all amplitudes, while KdV theory is good for the lowest value, before it starts to differ. This is in accordance with results from Grue et al. (1999) [18]. Looking at the wave width, the comparison is again good to the fully nonlinear model, but it differs for the largest value. This happens due to Kelvin-Helmholtz instabilities that are present for the largest wave, making the tail of the wave longer.

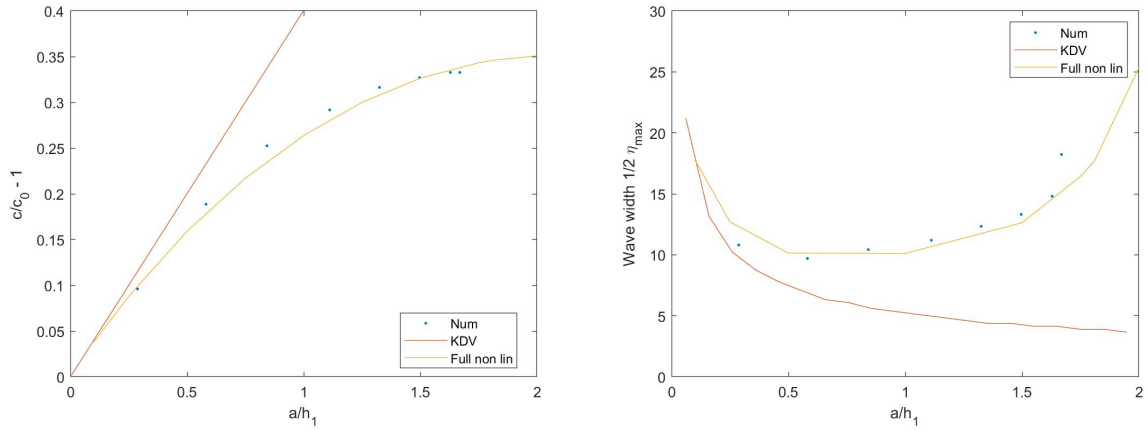

(a) Propagation speed

(b) Wave width

Figure 4.4: Comparison for the wave propagation speed $c/c_0 - 1$ and wave width at $\eta/2$ versus non-dimensional wave amplitude a/h_1 found using the VOF method in Basilisk. Red indicates KdV theory, yellow fully nonlinear theory and blue results from Basilisk

Our validation tests have shown that Basilisk compares well to fully nonlinear theory for nearly all measured parameters. Weakly nonlinear theory compares well for amplitudes up to $a/h_1 = 0.4$ before it starts to differ. This is in accordance with experiments performed by Grue et al. (1999) [18]. Basilisk overestimated the horizontal velocity in the lower layer and near the surface, at the position of max displacement compared to fully nonlinear theory.

Reproduction of Carr et al., (2008) [8]

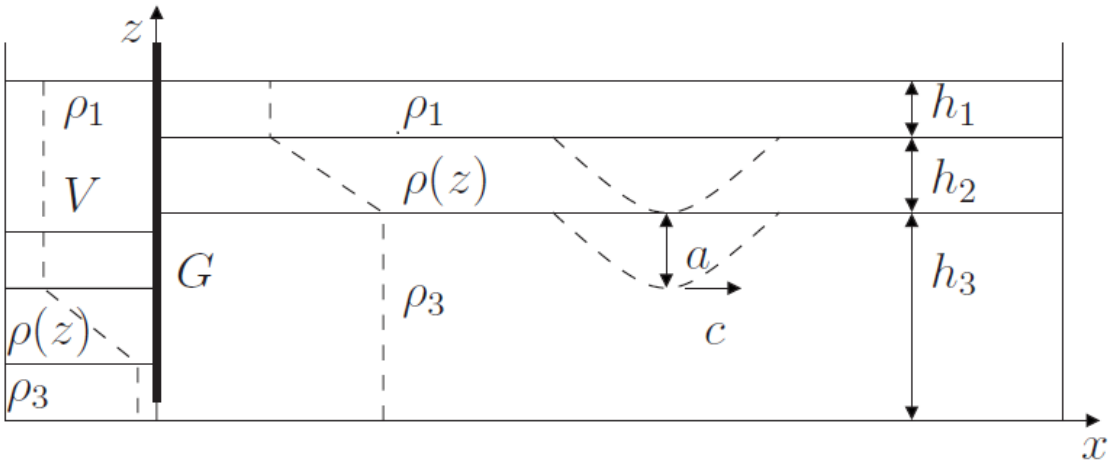

Figure 4.5: Illustration of experimental setup in a wave tank, figure 1 from Carr et al. (2008) [8]

Figure (4.5) shows the experimental setup used by Carr et al. They used a three-layered model, in a wave tank with dimensions of $6.4 \times 0.4 \times 0.6\text{m}^3$. The gate was situated 0.6m away from one end of the wave tank, with a small opening at the bottom of the gate making it possible for water to move from one side of the gate to the other, when adding the additional volume. The experimental parameters are presented in table (4.2), where ρ is the density, 1 denotes the upper layer, 3 the bottom layer, and H is the total height of the water column. h_0 denotes the height of the additional fresh water behind the gate and is given as $h_0 = 0.207\text{m}$. This value was found using the numerical program for internal waves called IW2, developed by P. O. Rusaas [36].

ρ_1 (g/cm^3)	ρ_3 (g/cm^3)	h_1 (m)	h_2 (m)	h_3 (m)	H (m)
0.999	1.047	0.035	0.052	0.0293	0.38

Table 4.2: Experimental parameters, Carr et al. (2008)

The same parameters were inserted into Basilisk, which gave the density profiles seen in figure (4.6).

Reverse flow

First, we look at the depth of the reverse flow due to an internal wave of depression at a fixed location along the x-axis. A reverse flow is defined as a flow in the same direction as the wave, but opposite the direction of the interior flow in the lower layer beneath the wave. We look at the non-dimensional height z/H against the non-dimensional time tc_0/H. Counting of the non-dimensional time starts when the wave crest passes the point $x/H \approx 7.6$. The height of the reverse flow is in our calculations taken as the maximum height of a horizontal velocity in the same direction as the wave. The reverse flow appears first after approximately one non-dimensional time unit, before it starts increasing almost linearly as time increases. The slope steepness from Basilisk is similar to that produced

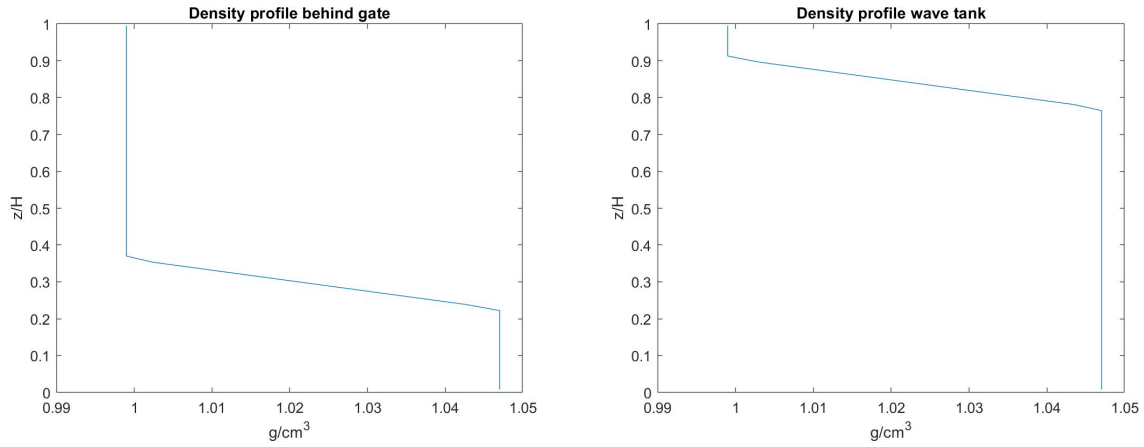

(a) Behind gate (b) Rest of wave tank

Figure 4.6: Density profiles from Basilisk

in figure 4 of Carr et al. (2008) [8]. The only difference is a small period of time in the experiments from Carr et al. where the reverse flow remains constant for a period of time, before it starts to increase again with similar steepness as before.

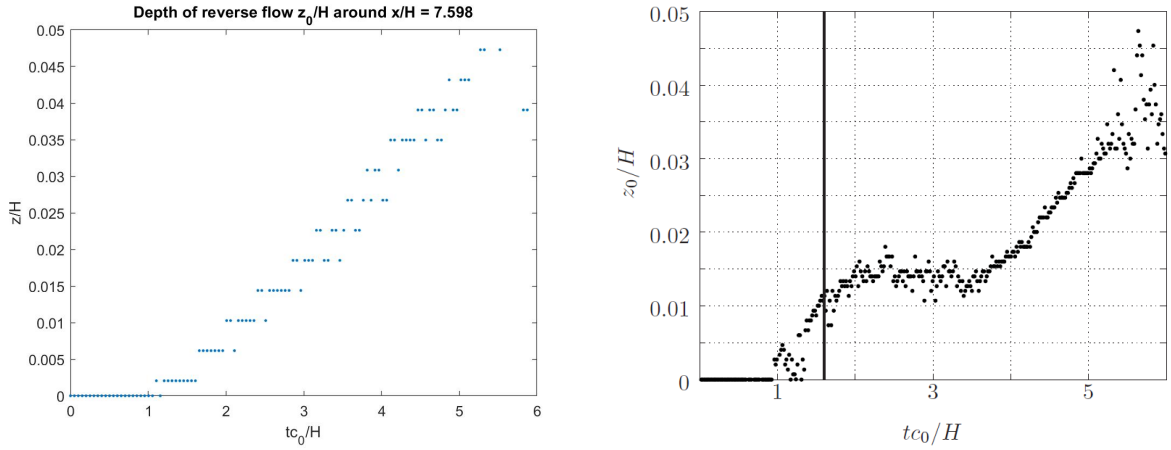

(a) Basilisk (b) Figure 4 from Carr et al. (2008) [8]

Figure 4.7: Comparison of the depth of the reverse flow at $x/H \approx 7.6$ versus non-dimensional time tc_0/H

Velocities at the bottom

Next, we look at the wave-induced velocities at fixed locations in the wave tank. We start looking at the non-dimensional horizontal velocity taken at $x/H \approx 7.6$ and $z/H \approx 0.013$. From figure (4.8) we can see an increased negative velocity that increases in magnitude prior to the wave crest passing our location, reaching a magnitude near $u/c_0 = -0.7$. The magnitude then decreases before it stabilizes itself positively, but close to zero. The magnitude is similar to the results shown in figure 5 presented in Carr et al. (2008) [8].

Figure (4.9) presents the non-dimensional vertical velocity taken at a fixed location $x/H \approx 7.6$ and $z/H \approx 0.052$ above the bottom of the tank. When the wave approaches

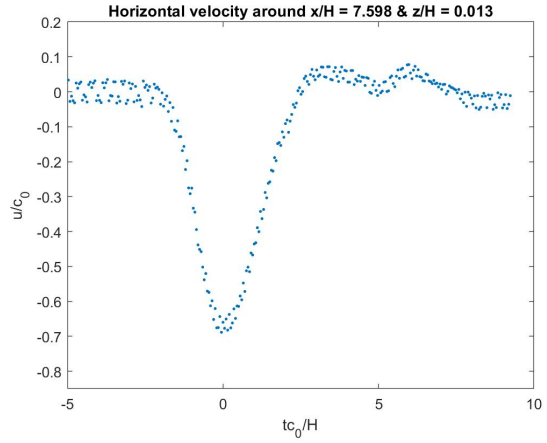

(a) Basilisk

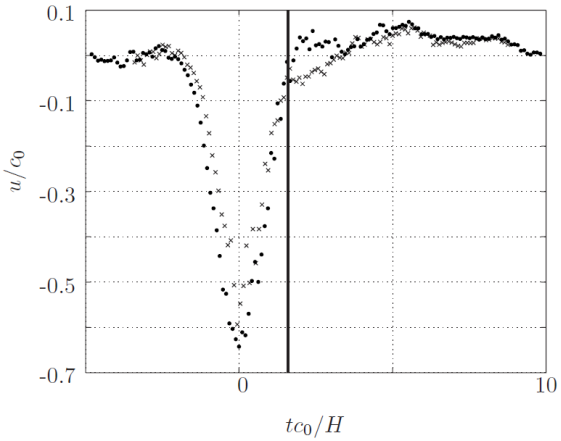

(b) Figure 5 from Carr et al. (2008) [8]

Figure 4.8: Comparison of the horizontal velocity u/c_0 versus non-dimensional time tc_0/H at $x/H \approx 7.6$ and $z/H \approx 0.013$, between Basilisk and Carr et al. (2008) [8]

our location, the wave induces a negative velocity, but as the wave crest approaches, the magnitude decreases to zero. As the wave propagates away, a positive velocity is induced reaching a smaller maximum value than the maximum negative induced velocity. After this point, vortices start to develop, and the flow gets chaotic. The results from Basilisk get more vigorous than those predicted by Carr et al., but the maximal velocities measured compare well to those presented in figure 6 of Carr et al. (2008) [8].

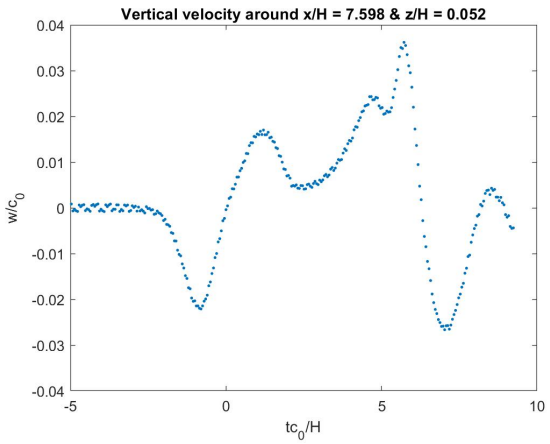

(a) Basilisk

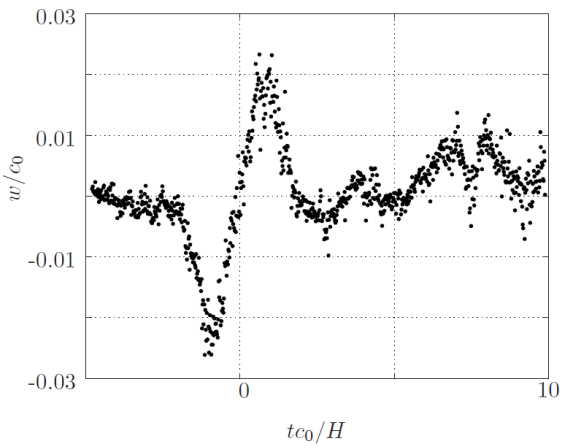

(b) Figure 5 from Carr et al. (2008) [8]

Figure 4.9: Comparison of the vertical velocity versus non-dimensional time tc_0/H at $x/H \approx 7.6$ and $z/H \approx 0.052$, between Basilisk and Carr et al. (2008) [8]

Velocity vector fields

At last, we look at the velocity vector fields developing behind the propagating wave. The following figures show the development for the velocity vector field as the non-dimensional time tc_0/H increases. The vortices appear at an earlier stage in Basilisk than those presented by Carr et al. (2008) ([8]) (figure 4.10), but the highest vortex measured is

at the same level at $\sim 6\%$ (figure 4.11). When we looked at the reverse flow, we saw that the results from Basilisk had a linear slope, while the experiments from Carr et al. had a period of zero slope steepness around $tc_0/H = 2$. The vortices developing at the bottom of the ocean gets created when the reverse flow gets strong enough. This might be the reason why vortices are created at an earlier point in Basilisk compared to the experiments.

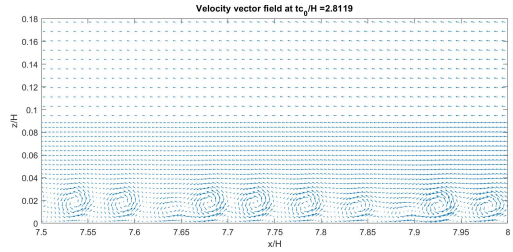

(a) Basilisk

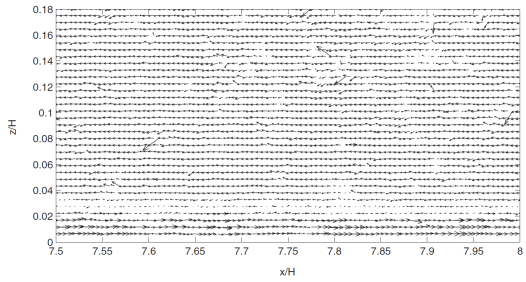

(b) Figure 8 from Carr et al. (2008) [8]

Figure 4.10: Comparison of the velocity vector field at $tc_0/H \approx 2.812$ between Basilisk and Carr et al. (2008) [8]

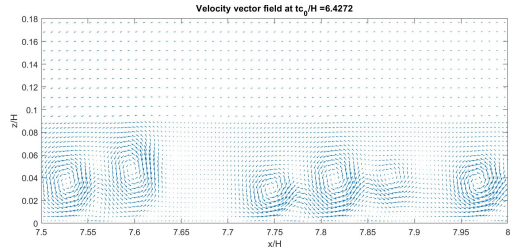

(a) Basilisk

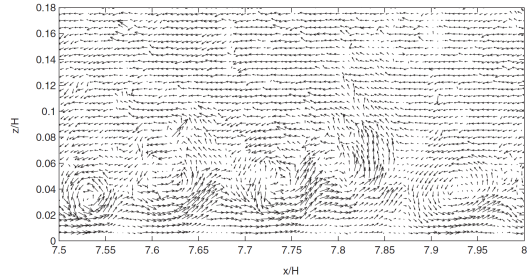

(b) Figure 10 from Carr et al. (2008) [8]

Figure 4.11: Comparison of the velocity vector field at $tc_0/H \approx 6.427$ between Basilisk and Carr et al. (2008) [8]

Comparison to experiments

Beside the numerical work with Basilisk, I have also contributed to experimental work performed at UiO by fellow master students Laila Andersland and Jon Alexander Pirolt. Together, we have run experiments where our goal has been to compare the experimental work to numerical results from Basilisk. As previously mentioned, we have used two different solvers in Basilisk. The first is a VOF solver that defines the interface sharply. Secondly, we have replaced the VOF solver with a passive tracer to track the interface. The reproduction of Carr et al. (2008) [8] (section 4.1) has been performed with both solvers in addition to experiments performed in the hydrolab at UiO. We will now perform a comparison between the three and see which solver is best at reproducing the experimental results.

We have performed comparisons for both the horizontal velocity profile situated at $x/H \approx 7.6$ and $z/H \approx 0.013$ (same as before) and the vertical velocity profile at $x/H \approx 7.6$ and $z/H \approx 0.052$. The horizontal velocity profile comparison as seen in figure (4.12), showed that the modified solver in Basilisk induces a slightly larger velocity compared to the experiments, but the wave shape is similar. If we look at the results in yellow (VOF solver), we see that the velocity profile follows the modified solver at the beginning of the wave, but the maximal obtained induced velocity is smaller. The VOF solver also differed from the other two in its rear part, due to the presence of Kelvin-Helmholtz instabilities, making the wave broader. This meant that the modified solver was better at recreating the experimental velocity profile.

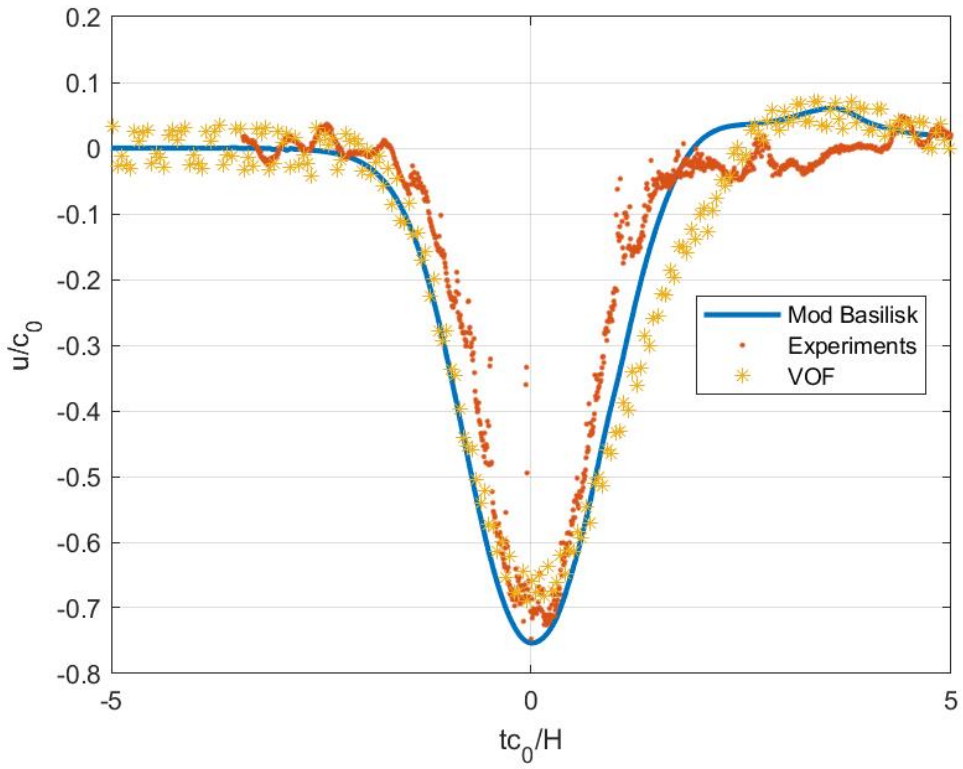

Figure 4.12: Comparison of the horizontal velocity at $x/H \approx 7.6$ and $z/H = 0.013$ between Basilisk using a: 1) Modified solver, 2) Experiments, 3) VOF solver

Secondly, we look at a comparison for the vertical velocity profile as seen in figure (4.13). Once more we see that the modified solver from Basilisk is better at retaining the induced velocity profile in addition to reaching the maximal induced velocities. The VOF solver does once more obtain smaller maximal velocities, and we see that the broadening of the wave affects the shape of the velocity profile.

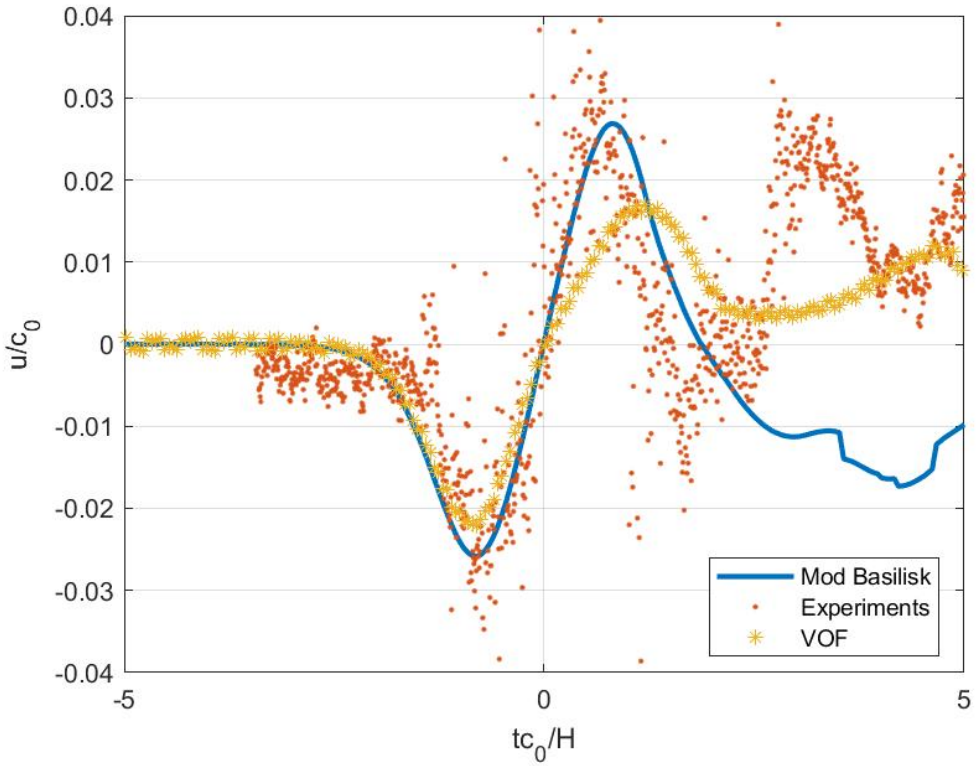

Figure 4.13: Comparison of the vertical velocity at $x/H \approx 7.6$ and $z/H = 0.052$ between Basilisk using a: 1) Modified solver, 2) Experiments, 3) VOF solver

This comparison has showed us that the modified solver from Basilisk is better at retaining the wave shape we saw from experiments. It does also better approximate the maximum induced velocities in the fluid. However, it looks like our modified solver induces a slightly larger velocity overall for the horizontal velocities.

4.2 Two- vs three-layered fluid

We have chosen to investigate both a two- and three-layered fluid when looking at the global instabilities. The problem with running simulations of large ISWs for a two-layered fluid is the presence of Kelvin-Helmholtz instabilities, which deform the internal wave and make the tail of the wave become steeper (Grue et al. 1999 [18]). To minimize the effect of Kelvin-Helmholtz we therefore perform simulations for a three-layered fluid.

Solving for a three-layered fluid in Basilisk using VOF proved to be difficult since the fluid interface started to diffuse, which changed the three- towards a two-layered fluid. This motivated us to modify the solver in order to maintain a three-layered fluid throughout the simulation. From this point, only our modified solver has been used. If we compare the wave profile in figure (4.14b) with a simulation using VOF with the same parameters as in figure (4.1d), we see that the non-dimensional amplitude increases a bit with our modified solver. The wave shape is also better retained with the modified solver, and Kelvin-Helmholtz looks to appear at a later stage compared to the wave profile found using a VOF solver.

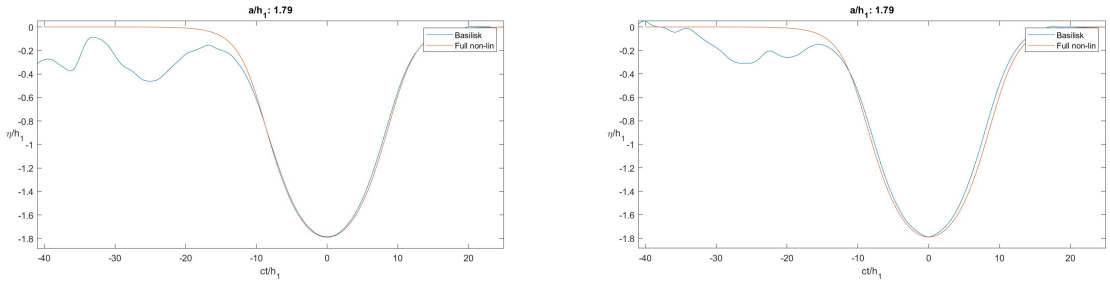

(a) Two-layered fluid (b) Three-layered fluid

Figure 4.14: Comparison of wave profiles to fully nonlinear theory for two- and three-layered fluid simulations using Basilisk

We start by comparing the wave profiles found in figure (4.14). Here we can see that results using a two-layered fluid better approximates the wave profile compared to fully nonlinear theory. The wave profile using a three-layered fluid is similar to the fully nonlinear theory, but the wave width becomes smaller. The fully nonlinear theory is however given for two-layered fluids and we should not expect a perfect match to our three-layered simulations.

Moving over to the horizontal velocities in the upper layer at $z = h_1/2$, the differences become significant as seen in figure (4.15). The two-layered fluid simulations compare well to fully nonlinear theory, while the three-layered fluid deviates significantly with a more pointy shape and a larger maximal velocity. This can however be explained by the conservation law for fluid velocities along a horizontal column.

$$\int_{-H}^{0} u dz = \int_{-H}^{0} \frac{\partial \psi}{\partial z} dz = \psi|_0 - \psi|_{-H} = 0 \tag{4.1}$$

This is true due to the fact that the stream function ψ is zero along the upper and lower boundary.

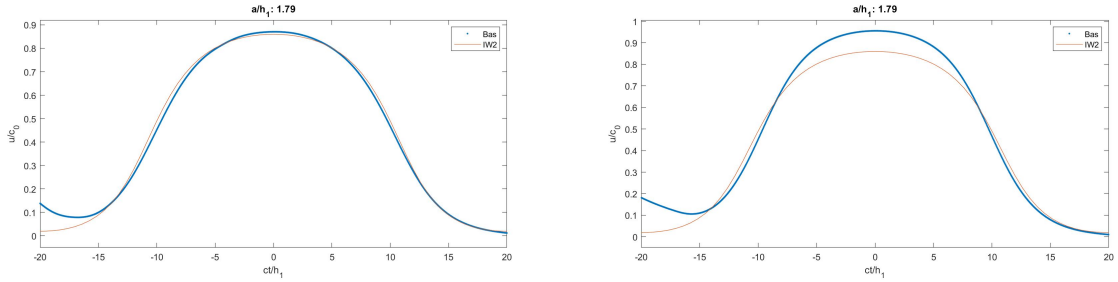

(a) Two-layered fluid (b) Three-layered fluid

Figure 4.15: Comparison of wave velocities at $z = h_1/2$ to fully nonlinear theory for two- and three-layered fluid simulations using Basilisk

Equation (4.1) tells us that the amount of fluid entering the horizontal column must also leave the horizontal column. Knowing this fact, we see that for a three-layered fluid, the horizontal velocity must increase in the upper layer for the integral to be zero. This is confirmed in figure (4.16), where the three-layered fluid has an increase in the horizontal velocity near the surface compared to the two-layered fluid. We have in figure (4.16) also compared fully nonlinear theory for a two-layered fluid (red line) to the results from Basilisk (blue dots) for the non-dimensional horizontal velocity profile u/c_0 at the maximal displacement of the wave. The two-layered simulations from Basilisk compare very well to theory, but slightly underestimate the velocities in the lower layer, while the three-layered fluid obtains a larger velocity in both the lower and upper layer. By comparing the results using the modified solver to the VOF solver used in figure (4.4), we see that the modified solver better approximates the horizontal velocity in the entire water column for a two-layered fluid.

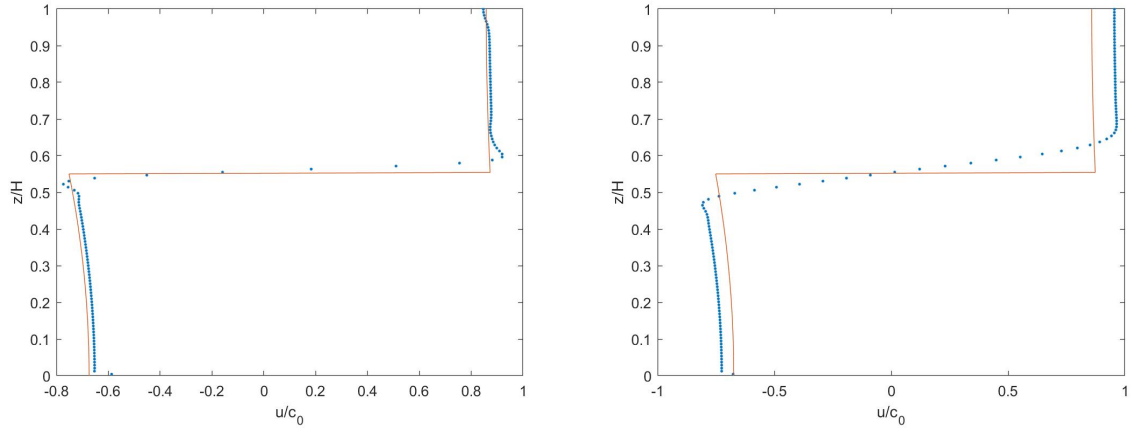

(a) Two-layered fluid (b) Three-layered fluid

Figure 4.16: Comparison of the non-dimensional horizontal velocities at the maximal displacement of the wave to fully nonlinear theory for two- and three-layered fluid simulations using Basilisk

The linear wave speed is in the two-layered case given as in equation (2.24) while the three-layered linear wave speed is found from equation (2.35). The ratio between these for the experimental parameters used by Carr et al. [8] is $\frac{c_{0,2lay}}{c_{0,3lay}} = 1.0962$. For figure (4.17), we scaled the horizontal velocity u in the two-layered fluid with $c_{0,2lay}$ and the

three-layered fluid with $c_{0,3lay}$. The relationship $c/c_0 - 1$ becomes larger in the three-layered case compared to the two-layered case. This tells us that the excess propagation speed is stronger for a three- than a two-layered fluid. We see from figure (4.17) that our modified solver compares well to fully nonlinear theory for most amplitudes, but as the non-dimensional amplitude increases, Basilisk starts to underestimate the predicted wave speeds.

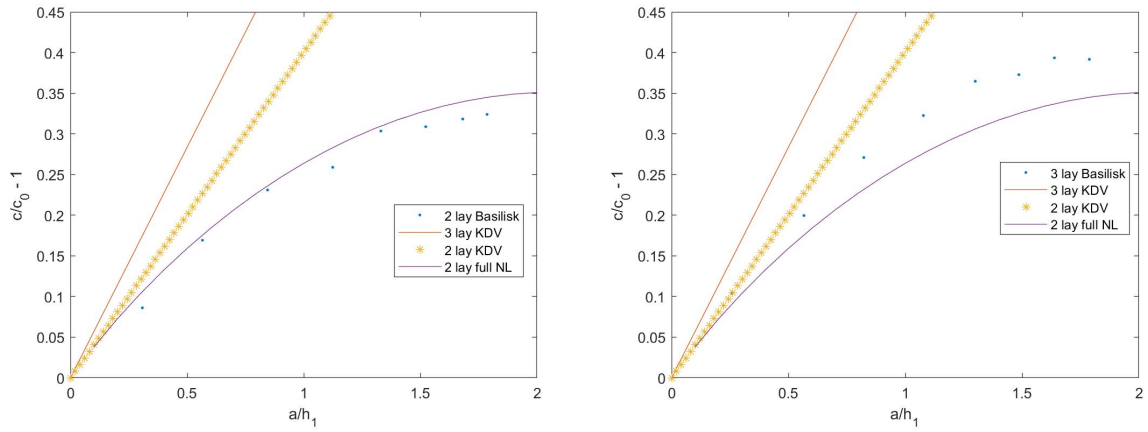

(a) Two-layered fluid

(b) Three-layered fluid

Figure 4.17: Comparison of the wave propagation speed between a) two-layered simulations in Basilisk, b) three-layered KdV equations, c) two-layered KdV equations and d) two-layered fully nonlinear theory for both a two- and three-layered fluid. The modified solver of Basilisk was used

4.3 Maximum wave

To maximize the vortex shedding along the bottom, we increase the nonlinearity of the wave and increase the initial amplitude h_0. The nonlinearity is now chosen to be $H/h_1 = 10$ where H is the total depth and h_1 the upper layer thickness. A max wave is defined as a wave amplitude satisfying the relation $(a + h_1)/H \approx 1/2$. If we perform a three-layered simulation, the upper layer thickness used in scaling is chosen to be $\tilde{h}_1 = h_1 + h_2/2$, where h_2 is the length of the mid-layer. The wave parameters used are given in table (4.3). When we run a two-layered simulation, half of the middle layer h_2 is added to both the upper and lower layer heights, to make the total wave height H unchanged.

We start by comparing the wave profiles for a two- and three-layered fluid simulation. Since the initial wave amplitude has been maximized we expect Kelvin-Helmholtz instabilities to have a large impact on the wave profiles. Figure (4.18) shows us that for a two-layered simulation (figure 4.18a), the shear-instabilities along the interface have a large impact on the wave profile and make the wave very broad. In the three-layered fluid (figure 4.18b), we see that the wave shape is much better retained, but also here Kelvin-Helmholtz instabilities are present due to the strongly nonlinear wave created. We notice that the wave amplitudes for the two- an three-layered fluids have become very different. Both simulations had the same initial conditions, with an amplitude of $a/h_1 = 4.0$. We see that a/h_1 in the simulated waves are smaller than this. This happens due to the broadening of the wave. When Kelvin-Helmholtz instabilities become strong enough, the wave profile

Upper density (g/cm^3)	ρ_1	0.999
Lower density (g/cm^3)	ρ_3	1.047
Upper layer (m)	h_1	$0.012/H$
Mid layer (m)	h_2	$0.052/H$
Lower layer (m)	h_3	$0.316/H$
Total depth (m)	H	0.38
Initial amplitude (m)	h_0	$0.278/H$
Gate position (m)	x_0	$0.90/H$
Tank length (m)	L_0	$12.0/H$

Table 4.3: Wave parameters, three-layer case for maximum wave in Basilisk

is changed, and the wave broadens. For such large waves, this also effects the wave amplitude and it decreases. Since the Kelvin-Helmholtz instabilities are strongest for the two-layered simulation, we see that this also has the smallest value of the nonlinear amplitude $a/h_1 = 3.20$ compared to $a/h_1 = 3.75$ for the three-layered simulation. The long tail seen in figure (4.18a) comes from our definition of the wave profile η, which follows the isoline of the salt water. The same effect occurs if we choose a different isoline, but the tail becomes more moderate.

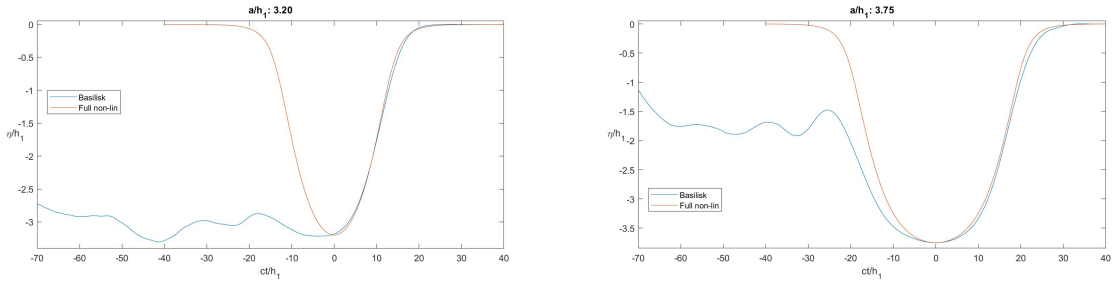

(a) Two-layered fluid

(b) Three-layered fluid

Figure 4.18: Comparison of wave profiles for a maximum wave for two- vs three-layered simulations to fully nonlinear theory

Next, we look at the reverse flow in figure (4.19). Here we see that the reverse flow is strongest for the three-layered fluid in the beginning and increases almost linearly until $tc_0/H = 10$. The two-layered fluid has on the other hand a more gentle start before it increases rapidly to the same level as in the three-layered fluid.

Bigger differences start to appear when we look at the horizontal velocity just above the bottom of the wave tank at $z/H \approx 0.013$ and $x/H \approx 7.60$. We saw in figure (4.18) that the wave profile became very different for a two- compared to a three-layered fluid. The effect of a smaller non-dimensional wave amplitude a/h_1 can also be seen in figure (4.20) with a decreased maximal horizontal velocity at $u/c_0 \approx 1.1$ for the two-layered fluid compared to $u/c_0 \approx 1.3$ for the three-layered simulation. Where a perfect solitary wave would give a symmetric horizontal velocity profile, we see from figure (4.20a) that the long tail of the wave makes the horizontal velocity profile of the two-layered fluid anti-symmetric.

Looking at the vertical velocity profiles at $x/H \approx 7.6$ and $z/H \approx 0.52$ in figure (4.21), we

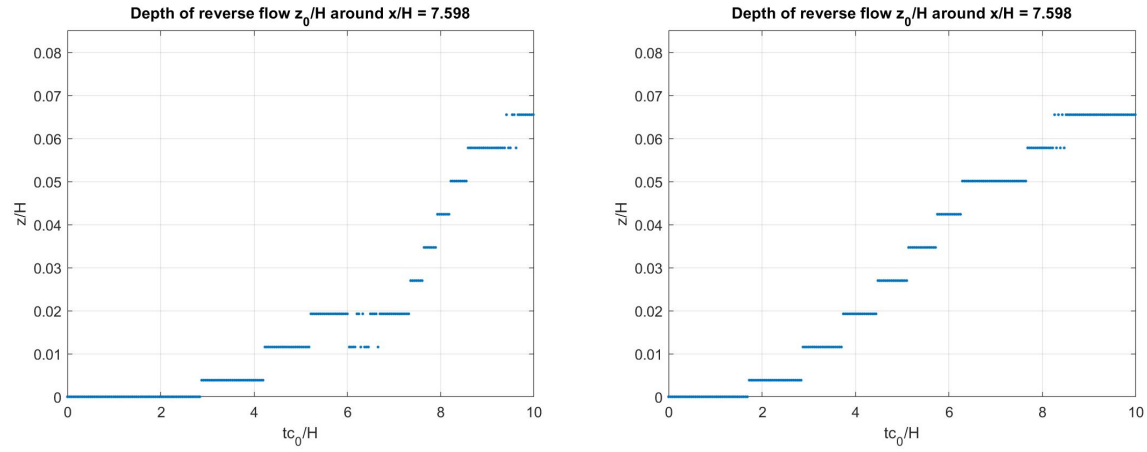

(a) Two-layered fluid (b) Three-layered fluid

Figure 4.19: Comparison of reverse flow for a maximum wave for two- vs three-layered simulations

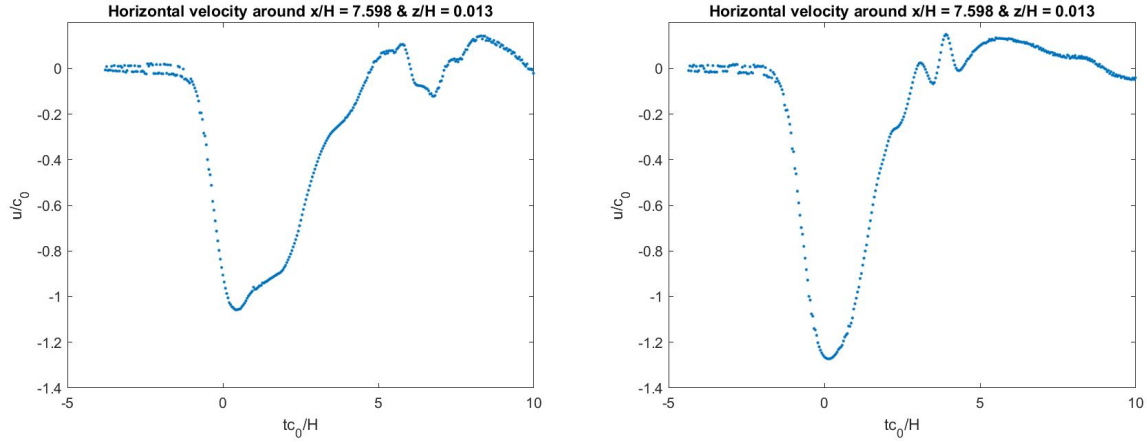

(a) Two-layered fluid (b) Three-layered fluid

Figure 4.20: Comparison of horizontal velocities near the bottom for a maximum wave for two- vs three-layered simulations

see that the three-layered fluid obtains the largest velocity once more. When we created similar profiles in the reproduction of Carr et al. (2008) [8] (section 4.1), we saw the ISW first induced a negative vertical velocity, before passing and inducing a positive vertical velocity. This time, we see that the positive induced vertical velocity appears at a later stage for the three-layered fluid, and even later for the two-layered fluid to what we saw earlier. The reason for this could be due to the broadening of the wave, making the tail of the wave longer. This means that it takes longer time for the wave to pass, making the fluid motion at the bottom more horizontal than vertical.

The next figure (4.22) shows a comparison for the vorticity at time $tc_0/H \approx 16$. Both simulations give vortices of approximately the same size. The difference of the height of the upper vortex is small, but with the three-layered simulation as the highest one. Another observation is the presence of a third vortex in figure (4.22b).

As an attempt on looking at how sediments from the bottom of the sea floor move in the

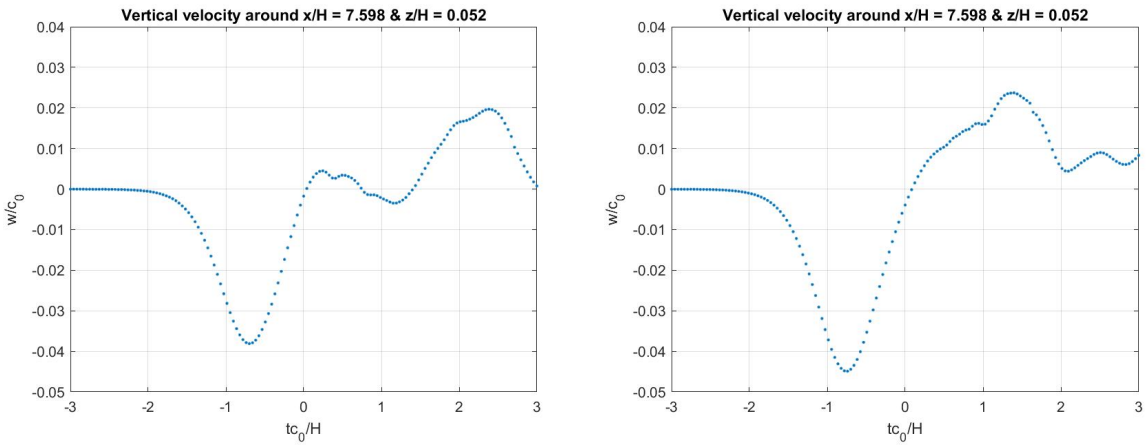

(a) Two-layered fluid (b) Three-layered fluid

Figure 4.21: Comparison of vertical velocities near the bottom for a maximum wave for two- vs three-layered simulations

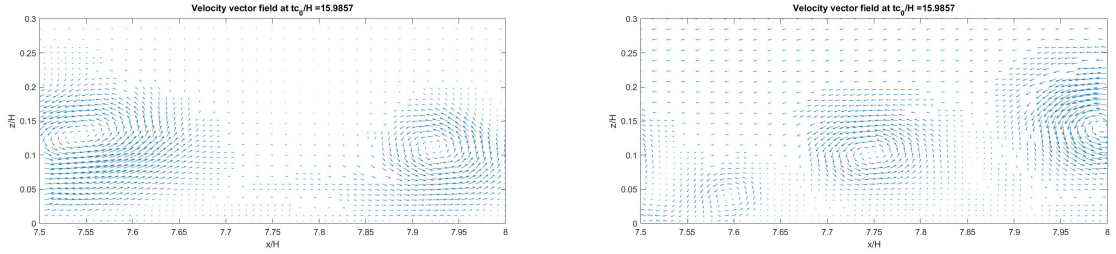

(a) Two-layered fluid (b) Three-layered fluid

Figure 4.22: Comparison of vorticity at $tc_0/H \approx 16$ for a maximum wave for two- vs three-layered simulations

water column, we have tracked particles using Lagrangian particle tracking. This is done by placing a number of particles along a horizontal line situated just above the bottom of the tank between $9.0 < x/H < 11.0$ at $z/H = 0.005$. The particles are then moved in the fluid by using the local velocity vector field for each timestep, and the results can be seen in figure (4.23). Here we see that the maximal attained height are similar for the two- and three-layered fluid, but the two-layered fluid are obtaining the largest value of $z/H \approx 0.25$, while the three-layered simulation are more consistent around $z/H \approx 0.20$. The main difference for the two fluids can be seen by the quantity of particles getting lifted. In the two-layered simulation, the most consistent particle trajectories can be seen between $8.5 < x/H < 9.0$ with a lift of approximately 10%. The three-layered fluid has however a much larger number of particles reaching the maximal obtained height of $z/H \approx 0.20$ or 20% of the height of the water column.

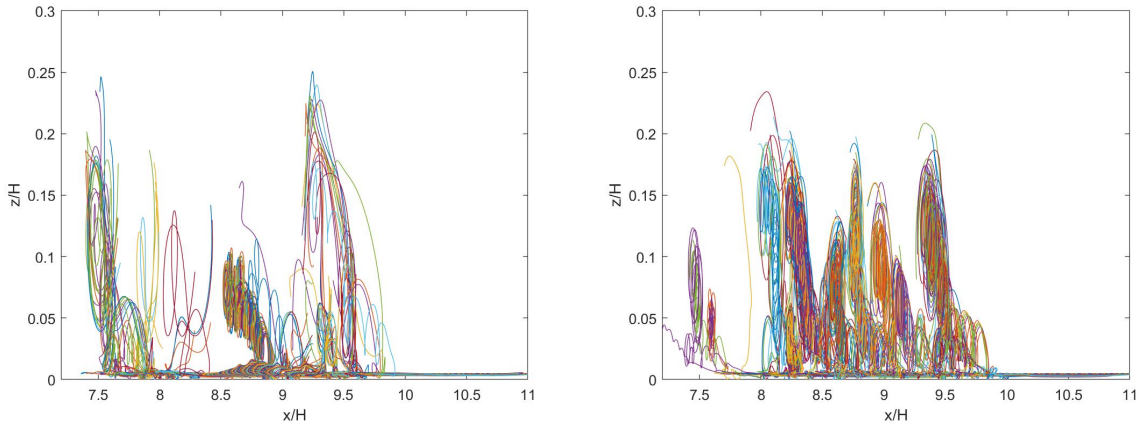

(a) Two-layered fluid (b) Three-layered fluid

Figure 4.23: Comparison of particle paths tracked with Lagrangian Particle Tracking for two- and three-layered fluid

Convergence of max wave

To validate the results for the max wave, we performed several simulations with a slight modification on the numerical parameters to look for convergence. We started by changing the relative tolerance in our simulations. This term is believed to give a restriction for the maximum allowed residual for pressure. If this condition is not fulfilled, the simulation is stopped. Our standard tolerance criteria of *Tolerance = 1e-4* was refined to *Tolerance = 1e-6*. We also modified the standard criteria of our maximum allowed timestep $\Delta t = 0.01$ to $\Delta t = 0.005$. Since we already are using the maximum allowed resolution for our computer, it could not be changed. A smaller resolution could have been used, but since the global instability occurs on a small scale, we need the finer resolution to catch them.

Before we look at the different particle paths, we have to make sure that we have created similar waves with the different numerical parameters. Looking at figure (4.24) we see that both the wave profiles and horizontal velocities in the upper layer are very similar.

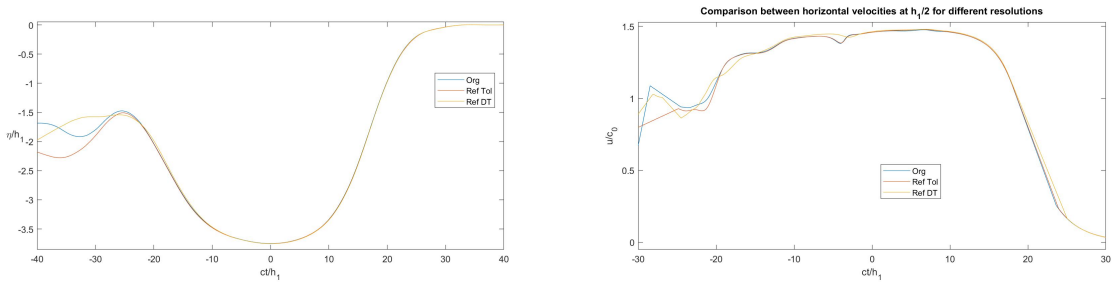

(a) Wave profile (b) Velocity in the upper layer at $u(y = h_1/2)$

Figure 4.24: Comparison of wave profile and the upper layer velocity for a max wave of different numerical parameters. Blue indicates our standard run, red refined tolerance and yellow refined timestep ΔT

In figure (4.25), we have compared the particle paths for the three simulations. The particles are initially placed at the same location for all cases. We see that all simulations

give similar results. Both the run named *Original* and *Refined timestep* have similarities when it comes to the amount and height travelled for the particles. The final simulation named *Refined tolerance* differs from the other two with a smaller quantity of particles getting lifted, but obtains a larger maximum height for a large quantity of particles at approximately $z/H = 0.3$. Based on our results we can clearly see a trend where particles get lifted high up into the water column beneath a propagating ISW. A lift of 20% the total water depth is achieved in all cases.

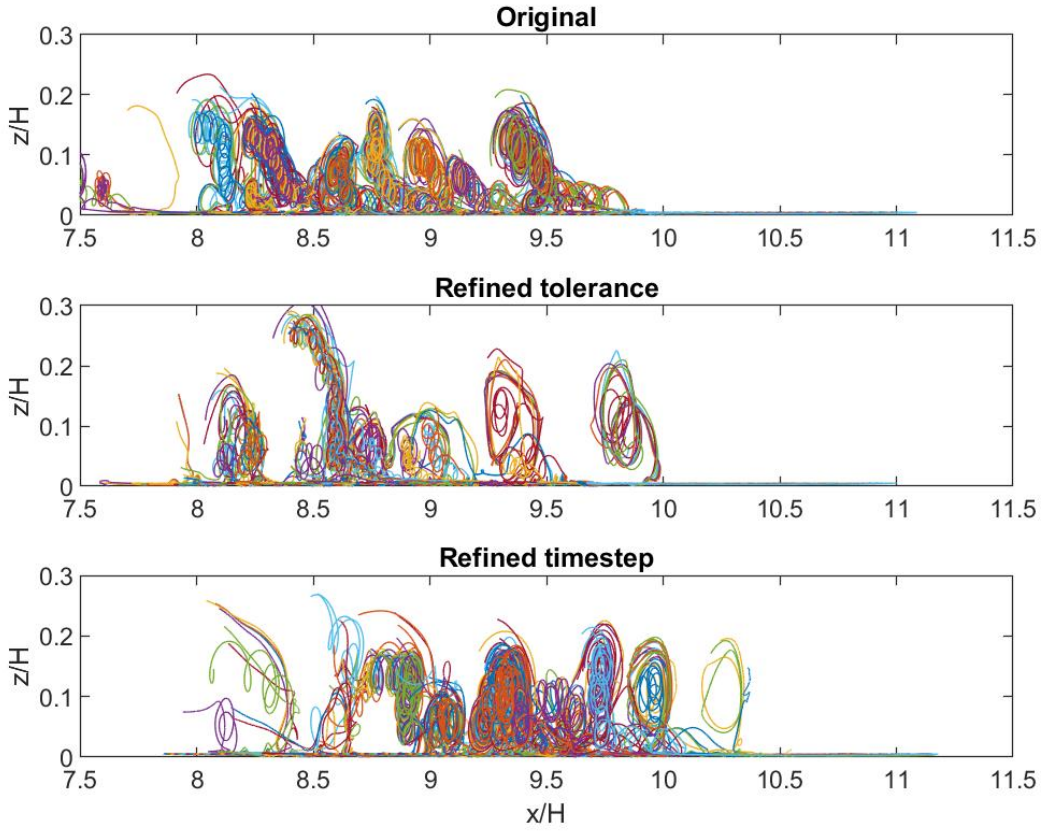

Figure 4.25: Comparison of particle paths for a max wave with small adjustments for the numerical parameters

4.4 Slope

Until now, we have only simulated ISWs propagating over a flat bottom. As an attempt to strengthen the global instability we attached a sloping bottom to the numerical wave tank. The slope has a maximum height of $H_{max} = 0.45H$ or half the lower layer $h_2/2$ (figure 4.26), where H is the total depth. The slope starts in one end of the wave tank and ends at the other end, which gives an amplitude of $\alpha = H_{max}/L_0 = 0.014$. The wave parameters are the same as for the max wave given in table (4.3), where x_0 is the gate position.

First, we look at how the wave profile is affected by the sloping bottom. Two wave profiles are given in figure (4.27). The red line indicates the wave profile created by the numerical program IW2 and is plotted as a reference for how a solitary wave of the given size should

Figure 4.26: Illustration of a sloping bottom created with EB in Basilisk

look like. We can see that the results from Basilisk give a very broad wave compared to the fully nonlinear theory used in IW2. Our results show that as the wave propagates up the sloping bottom, the wave is constantly broadening while the dimensionless wave amplitude a/h_1 is constantly decreasing. Similar behaviour was also seen in our study of how the pycnocline thickness affected the wave shape for large waves (see section 5.2).

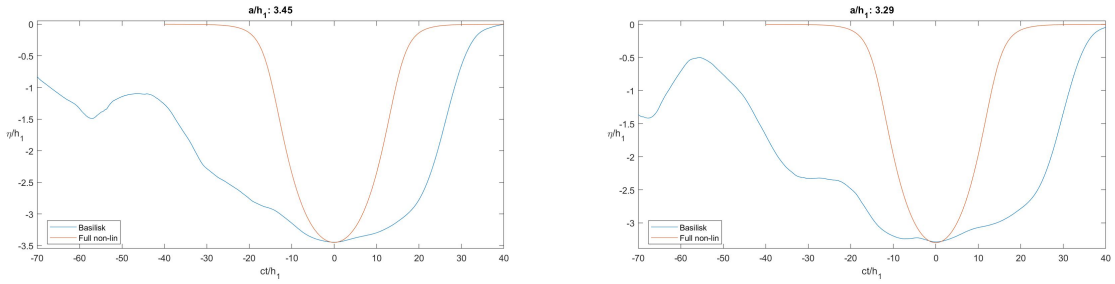

(a) $tc_0/H \approx 2.38$ (b) $tc_0/H \approx 5.47$

Figure 4.27: Wave profiles for two different dimensionless times tc_0/H. Red indicates the wave profile from fully nonlinear theory and is given as a reference

To get knowledge of the strength of the velocity field we look at the horizontal and vertical velocity profiles at the bottom of the wave tank. The velocities are made dimensionless by dividing with the linear wave speed c_0. By comparing the maximal velocities given in figure (4.28) with previous velocity profiles, we notice a small increase for the horizontal velocities, but twice as strong max velocity for the vertical velocities. Since we have included a slope, the measurement point is situated higher in the water column, which can have affected the strength of the velocities. However, since the maximal horizontal velocity is similar to earlier results (figure 4.20a) the large change in vertical velocities are worth noticing.

When including a sloping bottom, the maximal height reached by a vortex (figure 4.29) is similar to the simulations of the max wave (section 4.3). The vortex strength is in this case larger than in the maximum wave simulations seen in figure (4.22b). The increased vortex strength results in a large quantity of particles getting lifted from the bottom floor (figure 4.30a). Now, a larger amount of particles are moved higher up into the water column, with a maximal vertical distance of approximately $z/H \approx 0.45$.

Particles were also initialized further up the slope between $13 < x/H < 15$ and $z/H = 0.22$, with the results given in figure (4.30b). Here we see similar behaviour as in figure (4.30a), with a large amount of particles getting lifted up into the water column. The maximum distance travelled vertically for particles in figure (4.30b) are smaller than in figure (4.30a). This could be due to the fact that as the wave propagates up the slope, its length increases and its nonlinear amplitude decreases. Since both figures are created from the same simulation, the non-dimensional time that the particles in figure (4.30b) have travelled are

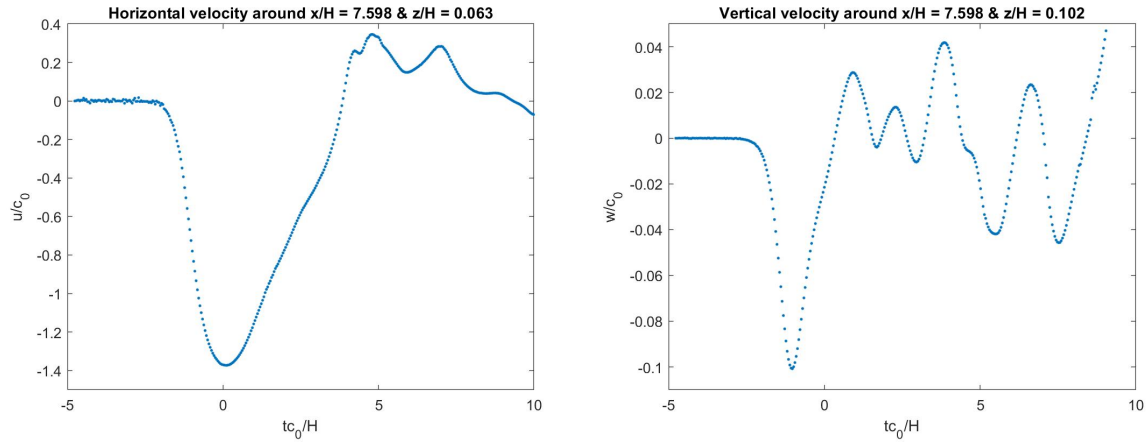

(a) Horizontal velocity (b) Vertical velocity

Figure 4.28: Velocity profiles at a fixed point situated at the bottom of the wave tank. (a) Horizontal velocity at $x/H \approx 7.60$ and $z/H \approx 0.063$. (b) Vertical velocity at $x/H \approx 7.60$ and $z/H \approx 0.102$

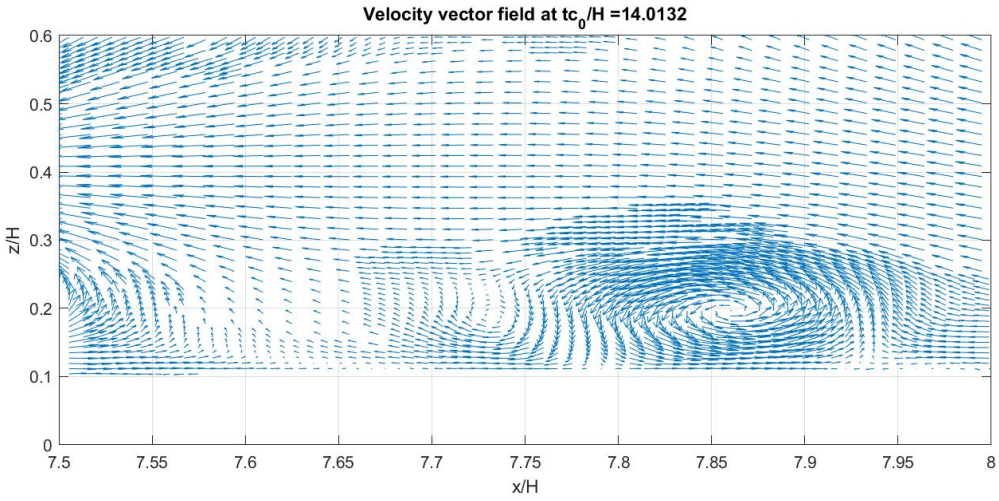

Figure 4.29: Velocity vector field at $tc_0/H \approx 14$ for an area near the bottom of the slope

also smaller than in figure (4.30a). This affects the particle trajectories, since the vortices as seen in figure (4.29) are at their strongest at the end of the simulations.

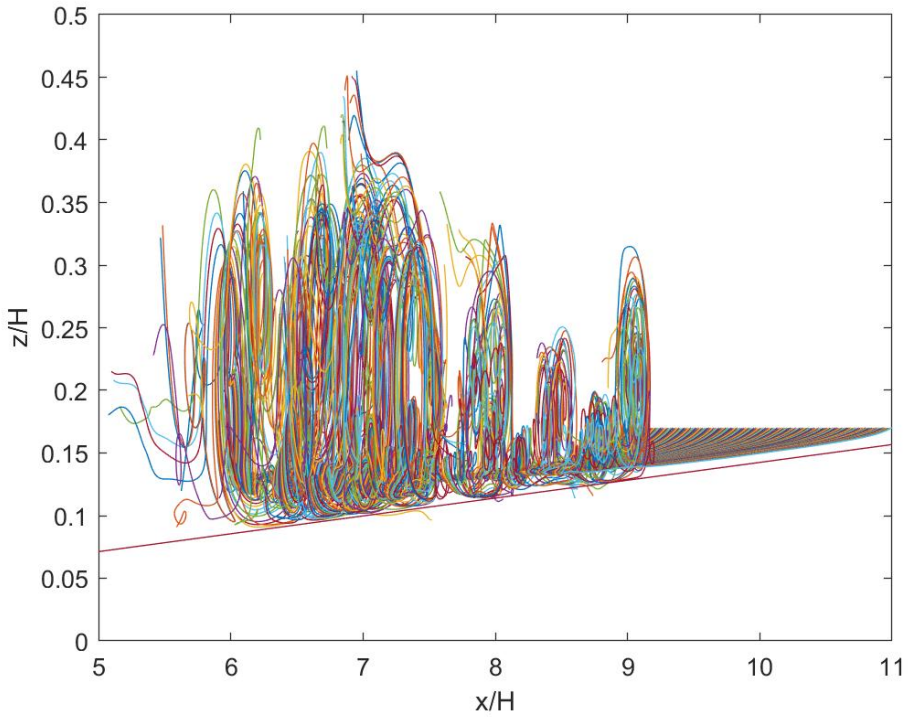

(a) Position nr 1

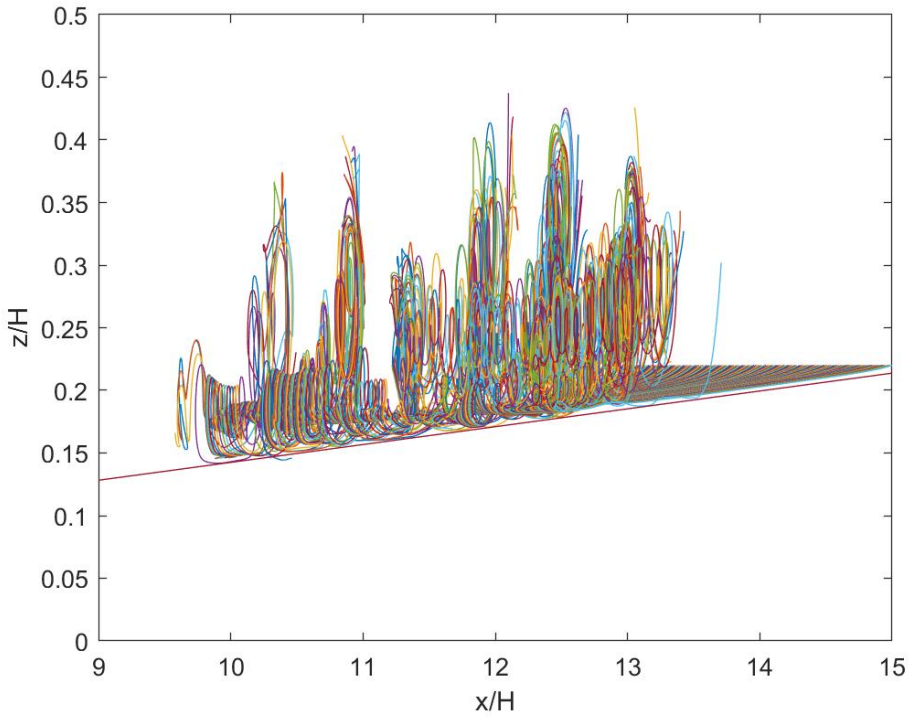

(b) Position nr 2

Figure 4.30: Particle paths found with Lagrangian particle tracking for two different positions with $\alpha = 0.014$

Increasing the steepness

After including a sloping bottom in the previous section, we increased the slope steepness to see how this affected the results. The slope steepness was therefore increased to $\alpha = 0.028$ by decreasing the length of the wave tank L_0 to half of its original value. The simulations with the steeper sloping bottom were performed for two different resolutions, as a verification of the results. The wave profile found when using the finest resolution can be seen in figure (4.31). Once more, we see how the sloping bottom appears to change the wave profile, by decreasing the amplitude and increasing its length.

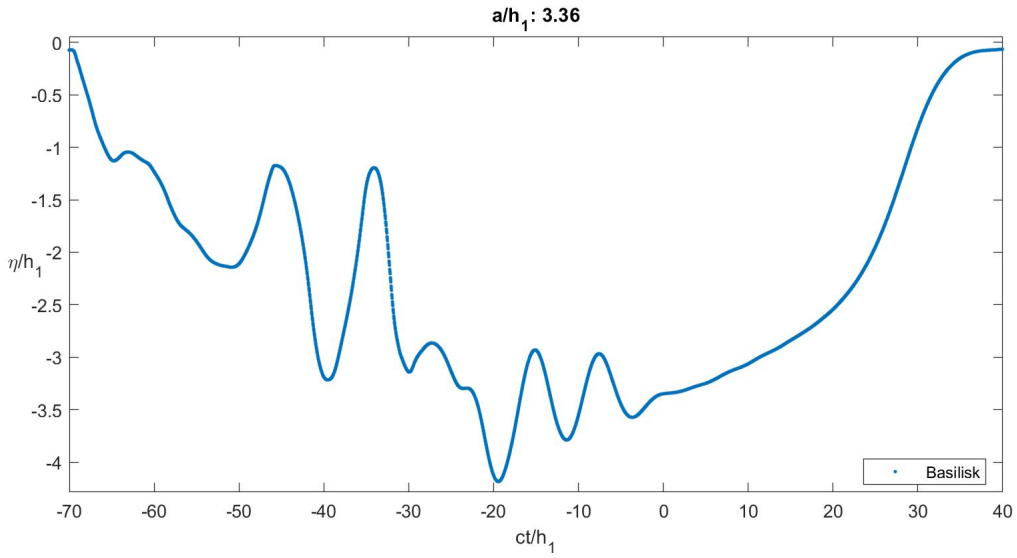

Figure 4.31: Wave profile from Basilisk taken at $tc_0/H \approx 2.38$ for the finest resolution

Figure (4.32) shows one of the vortices that evolved as the internal wave propagated uphill. The magnitude of this vortex is large, and it has a vertical extension just beneath 30% of the total wave depth. This is 50% larger than the vortex seen in figure (4.29), for a slope of steepness $\alpha = 0.014$. A vortex of this size can contribute massively towards lifting sediments from the bottom up in the water column. In figure (4.33) we see the particle paths for both a "coarse" and "fine" resolution for a sloping bottom of amplitude $\alpha = 0.028$. We can see from both figures that a large amount of particles reach a height of minimum 60% of the total water depth H. Since the particles are moved vertically more than 50% of the total water depth, a complete mixing of the water column is expected to occur for such large waves. In figure (4.33) we can even see particles reaching a maximum height of 80% of the total water depth H.

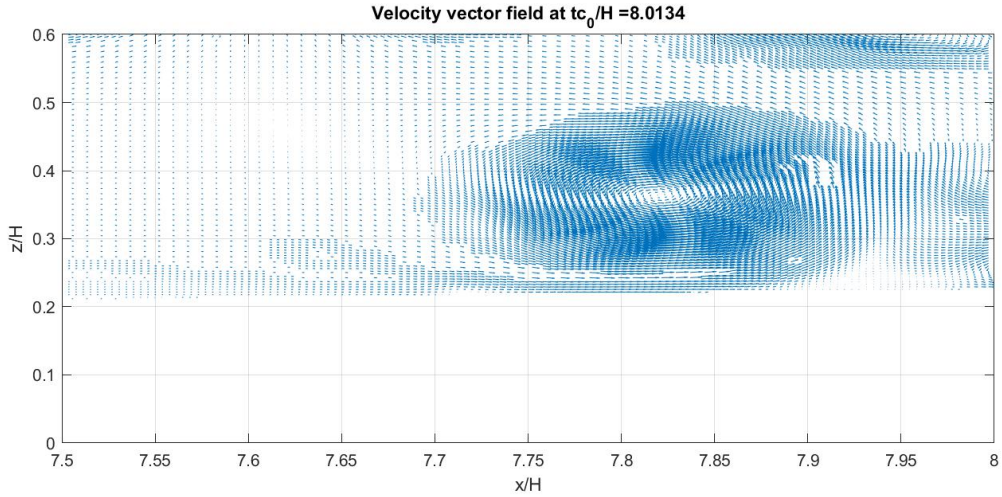

Figure 4.32: Velocity vector field from Basilisk at $tc_0/H \approx 8$ for a sloping bottom of steepness $\alpha = 0.028$

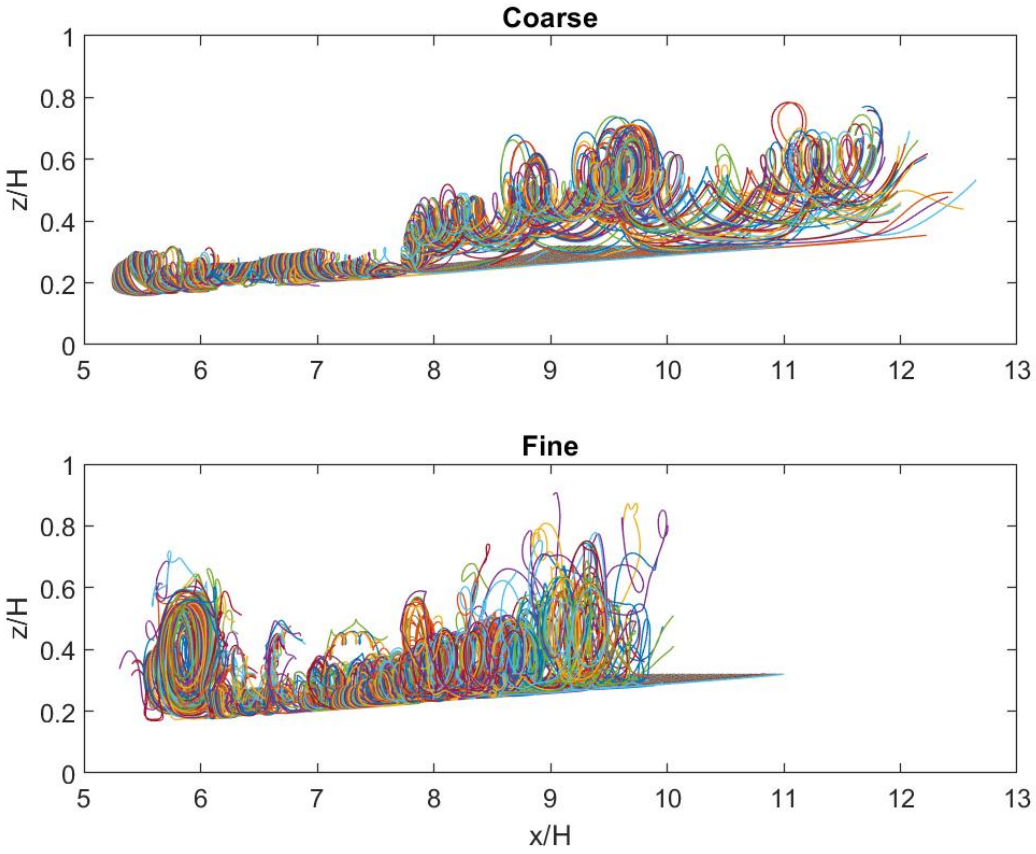

Figure 4.33: Particle paths from Basilisk for two different resolutions with $\alpha = 0.028$

We have in this section shown that a steeper slope results in larger vortices and due to this, particles are lifted higher up into the water column. As an attempt to explain the reason behind this, we look at the horizontal velocity u just above the sloping bottom. We have previously looked at the reverse flow that develops behind the propagating ISW,

but we have not looked at its magnitude. This has been done using the image viewer *Paraview* and the maximum measured velocity can be seen in table (4.4). Here we see that the horizontal velocity u has a maximum positive velocity of almost twice the size for $\alpha = 0.028$ compared to $\alpha = 0.014$. Since the strength of the reverse flow is increased with an increase in the slope steepness α, the shear tension will also increase along the reverse flow. The increase in shear tension could be the reason why vortices become larger in size with slope steepness.

α	$u_{rev,max}$
0.014	0.28 m/s
0.028	0.54 m/s

Table 4.4: The strength of the reverse flow for different slope steepness

CHAPTER 5

Further results and further discussions

5.1 Convergence of Basilisk

When using a numerical model, it is important to control the truncation errors. This is done through convergence of the numerical method. Convergence is reached if the truncation error decreases with resolution. We will now perform a convergence test for the modified solver in Basilisk. The parameters used are the same as in our comparison between a two- and three-layered fluid. We will investigate convergence for several different aspects of the simulation, such as wave profile, horizontal velocity in the upper layer and the velocity profiles at the bottom of the wave tank. In this test, the height of the layers are put to constant values, and two-layered simulations are performed by adding half of the middle layer h_2 to the upper and lower layer heights. We have run three simulations for both two- and three-layered fluids. We use the same number of cells in all simulations, but vary the tank length to obtain the different resolutions. The step-length is given as $\Delta x = L_0/N$. The numerical parameters are given in table (5.1):

Number of horizontal cells (Const val)	N	2048
Original tank length	$L_{0,org}$	10.0/H
Refined tank length	$L_{0,ref}$	0.7*10/H
Coarse tank length	$L_{0,cor}$	2.0*10/H
Total height	H	0.38
Upper layer thickness	h_1	0.035/H
Middle layer thickness	h_2	0.052/H
Lower layer thickness	h_3	0.293/H

Table 5.1: Numerical parameters for convergence runs in Basilisk

Two-layered fluid

First, we look at the wave profile and the horizontal velocity at $z = h_1/2$ in figure (5.1). As the step size Δx decreases, we see that the differences between the different resolutions decrease, and convergence is obtained.

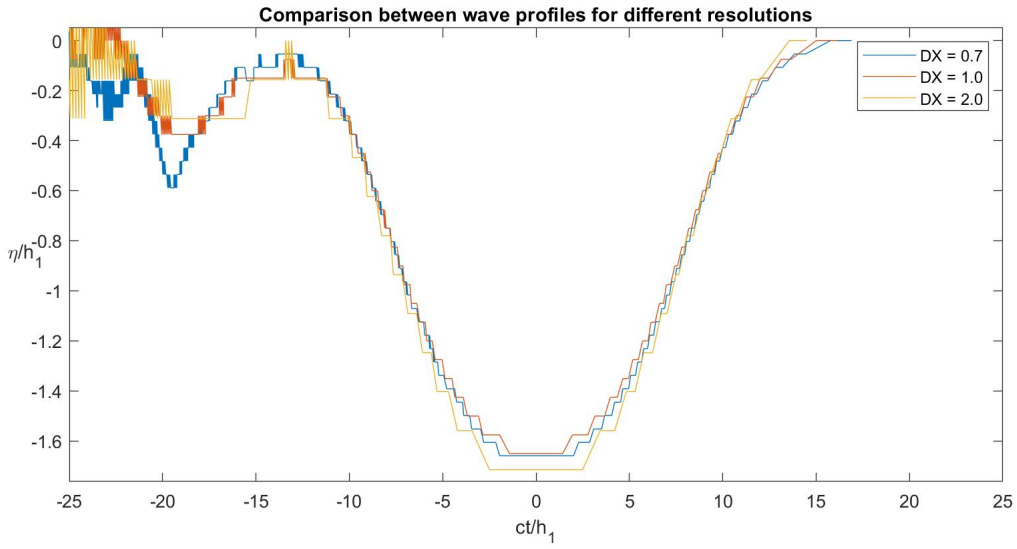

(a) Wave profile

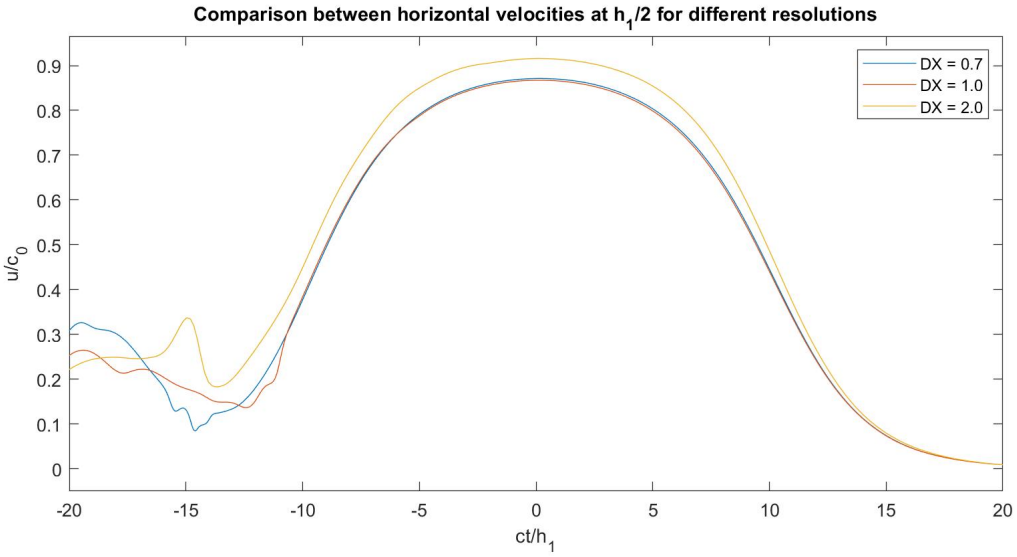

(b) Horizontal velocity at $z = h_1/2$

Figure 5.1: (a) Wave profile and (b) horizontal velocity in the upper layer for different resolutions (Two-layered simulations)

Next, we look for convergence for the velocities near the bottom of the wave tank as seen in figure (5.2). Here we see that different Δx provides very similar results. One thing to note is that an increase in the resolution results in a slightly smaller maximal value. Since the results converge towards the same result, we know that the truncation errors are kept to a minimum.

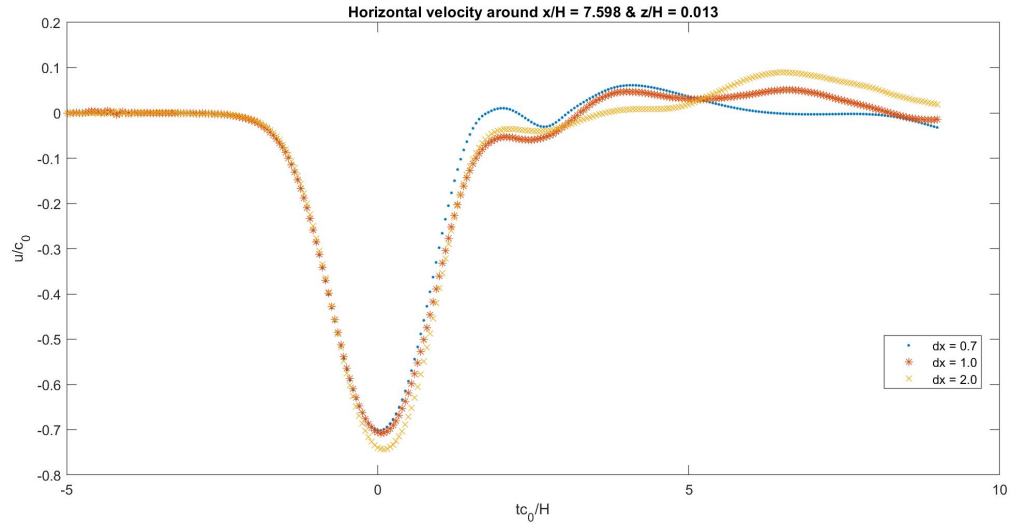

(a) Horizontal velocities

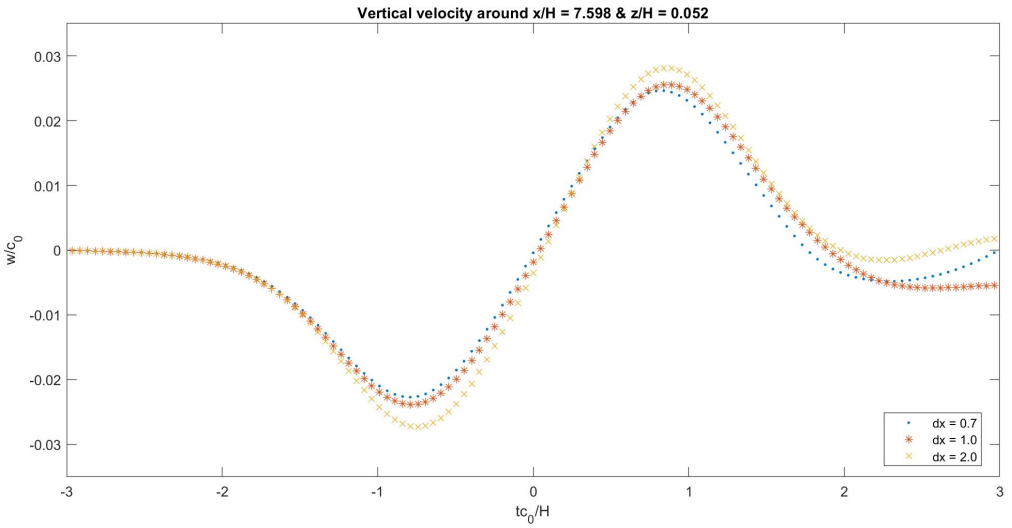

(b) Vertical velocities

Figure 5.2: (a) Horizontal velocities and (b) vertical velocities at the bottom of the wave tank for different resolutions (Two-layered simulations)

Three-layered fluid

A check for convergence was also performed for a three-layered fluid. By decreasing the length of the wave tank and hence increasing the resolution, we obtain convergence for the wave profile and the horizontal velocity in the upper layer for a three-layered fluid (figure 5.3).

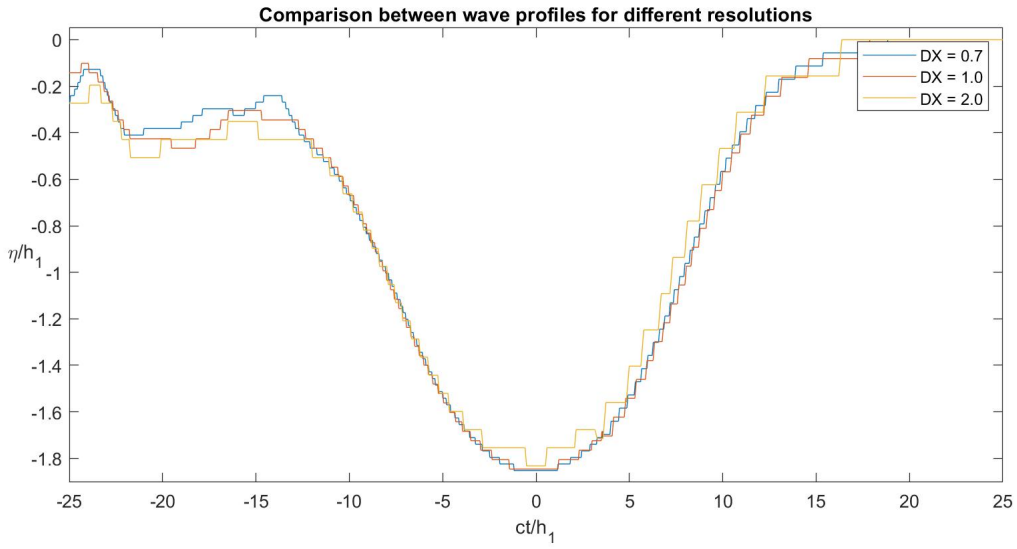

(a) Wave profile

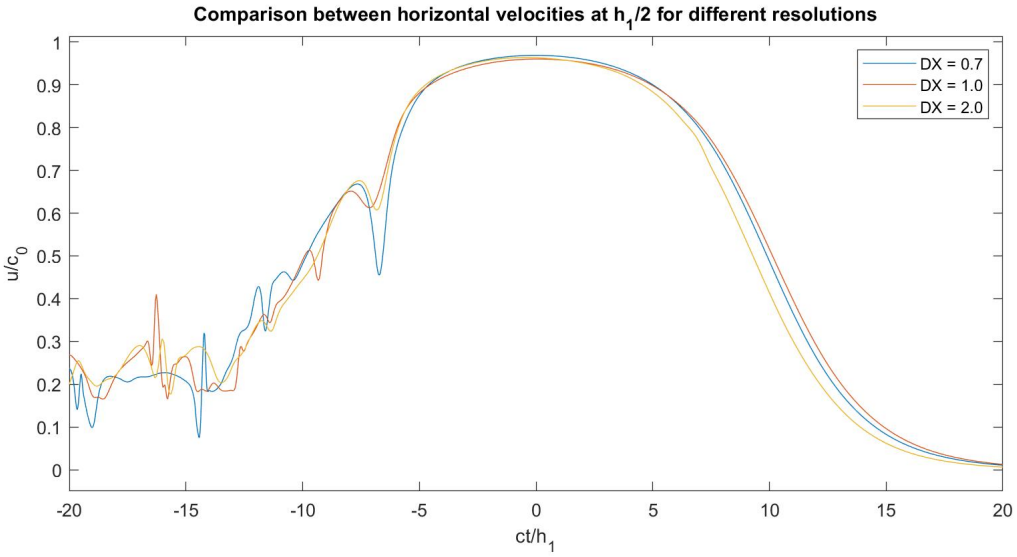

(b) Horizontal velocity at $z = h_1/2$

Figure 5.3: (a) Wave profile and (b) horizontal velocity in the upper layer for different resolutions (Three-layered simulations)

Finally, we look at a comparison for the horizontal and vertical velocity profiles at the bottom of the wave tank. We can see from figure (5.4) that the different resolutions give very similar results. This means that we will create similar waves despite differences in the numerical solver, and we know that the truncation errors are small.

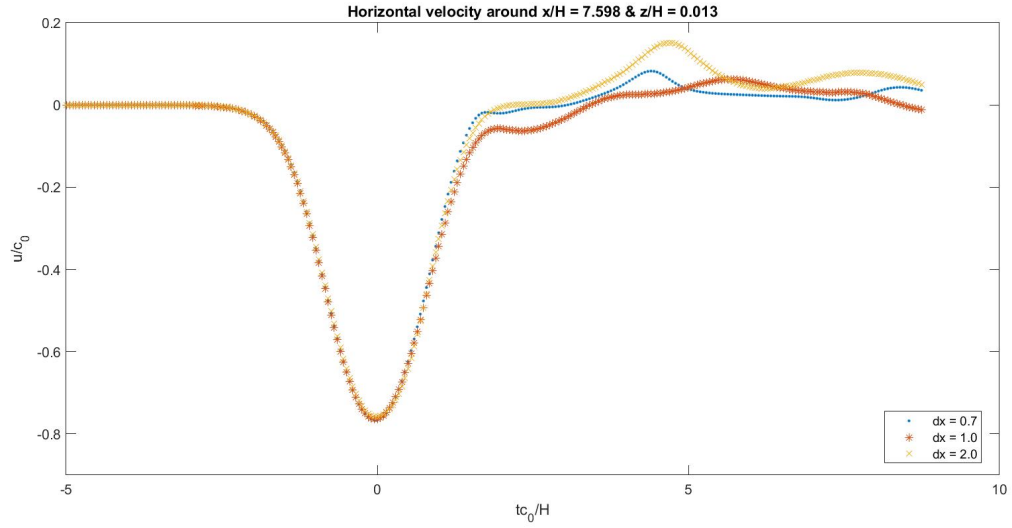

(a) Horizontal velocities

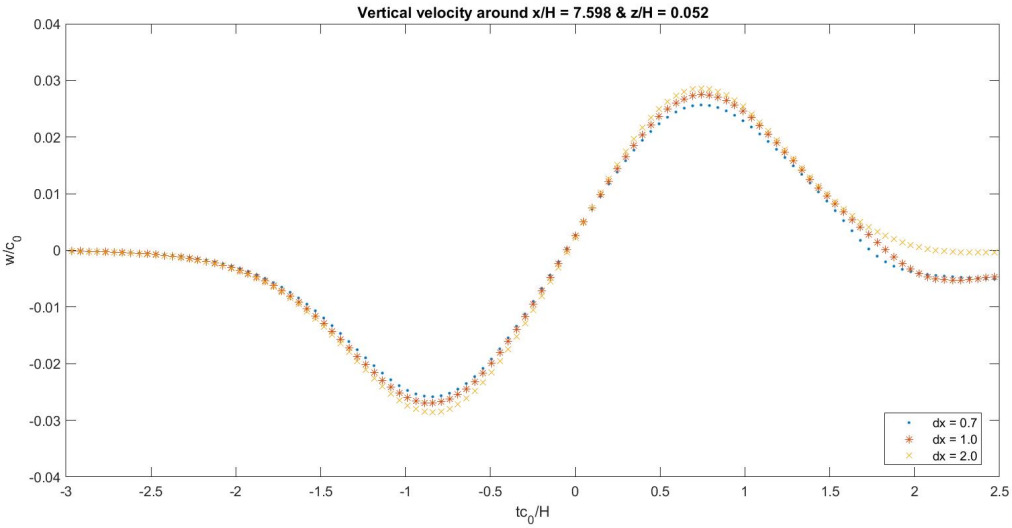

(b) Vertical velocities

Figure 5.4: (a) Horizontal velocities and (b) vertical velocities at the bottom of the wave tank for different resolutions (Three-layered simulations)

5.2 Notes on Kelvin-Helmholtz instabilities

In this section, we are going to investigate how different pycnocline thicknesses affects Kelvin-Helmholtz instabilities at the interface and the instabilities and wave characteristics at the bottom of the wave tank for large ISWs of non-dimensional amplitude $a/h_1 \approx 2.75$. This is done by adjusting the thickness of the pycnocline from a two-layered simulation $h_2 = 0$, to a large pycnocline at $h_2 = 0.08/H$ (21% of the total water depth) for a three-layered simulation. The different layer thicknesses are chosen to satisfy $H/\bar{h}_1 = 8$, where $H = h_1 + h_2 + h_3$ and $\bar{h}_1 = h_1 + h_2/2$. All numerical parameters are given in table (5.2).

No pycnocline	$h_2 = 0$
Small pycnocline	$h_2 = 0.02/H$
Medium pycnocline	$h_2 = 0.04/H$
Large pycnocline	$h_2 = 0.08/H$
Nonlinearity	$H/\bar{h}_1 = 8$
Initial amplitude	$h_0 = 0.25/H$
Gate position	$x_0 = 0.9/H$
Tank length	$L_0 = 10.0/H$

Table 5.2: Wave parameters for investigating different pycnocline thicknesses

We start by looking at the wave profile for different pycnocline thicknesses. The graphs are named *N - Two-layer fluid*, *S - small pycnocline*, *M - medium pycnocline* and *L - large pycnocline*. We can see from figure (5.5a) that as the pycnocline decreases, the wave profile is broadening. This is expected since a large pycnocline decreases the shear tension and therefore also the broadening of the wave due to Kelvin-Helmholtz instabilities. Looking at the horizontal velocity in the upper layer (figure 5.5b), we see that the thickest pycnocline also have the largest horizontal velocity in the upper layer, which is the same result as we found in section (4.2).

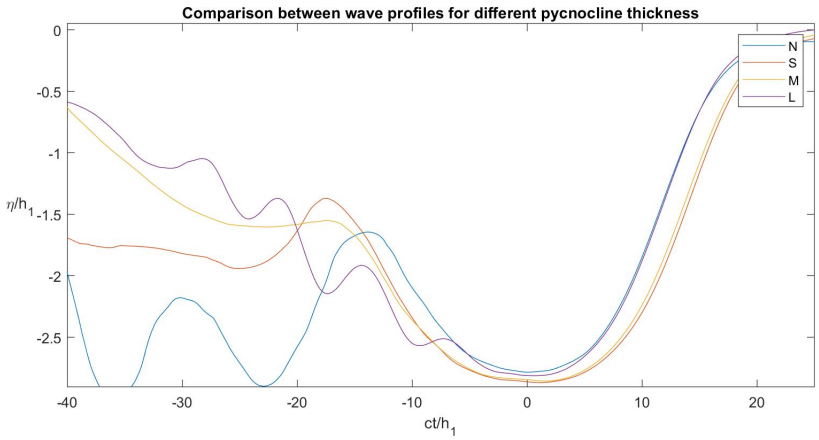

(a) Wave profile η

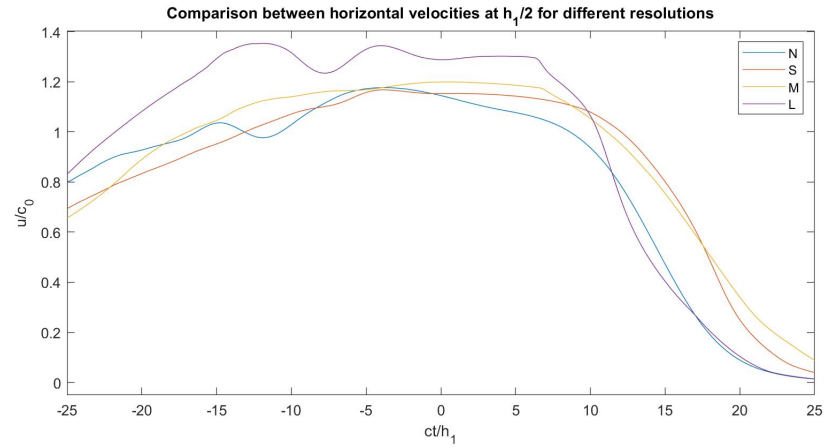

(b) $u(z = h_1/2)$

Figure 5.5: (a) Wave profile and (b) horizontal velocity in the upper layer at $z = h_1/2$ for different pycnocline thicknesses

Next, we investigate the velocity profiles at the bottom of the wave tank at a fixed point. Figure (5.6a) shows a comparison between both the horizontal and vertical velocity profiles for different pycnocline thicknesses. From this figure, we see that the maximum velocity increases with the pycnocline thickness. If we combine these results together with the results from figure (5.5) showing the wave profiles, this observation tells us that a small pycnocline thickness gives a broad wave profile, which results in smaller maximal velocities along the bottom of the wave tank. This figure also shows that the relative difference between the different pycnocline thicknesses is largest in for the horizontal velocity, where the velocity profile becomes very broad in its upper rear part.

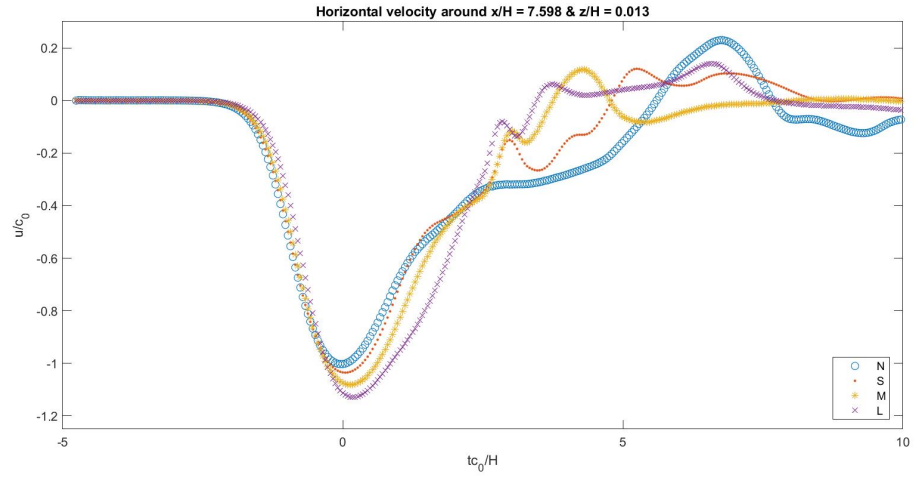

(a) Horizontal velocity

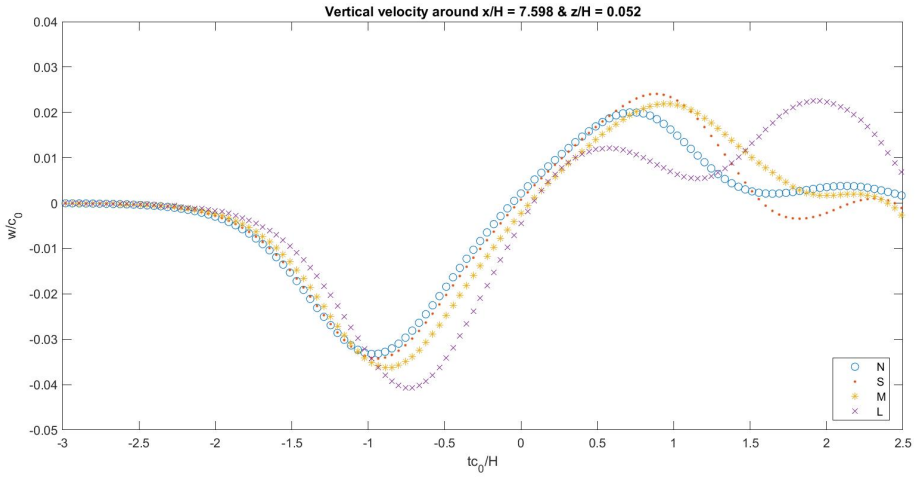

(b) Vertical velocity

Figure 5.6: (a) Horizontal and (b) vertical velocity measured along the bottom for different pycnocline thicknesses. Both is measured at $x/H \approx 7.6$ with a) at $y/H \approx 0.013$ and b) at $y/H \approx 0.052$

To understand the evolution of instabilities at the bottom of the wave tank, we plot the velocity vector fields for two different non-dimensional times. The times chosen are $tc_0/H \approx (6, 12)$. From figure (5.7) we see that a thicker pycnocline results in more vortices. If we increase the time to $tc_0/H \approx 12$ as shown in figure (5.8) we see that the difference is large between a two-layered simulation (no pycnocline) and having a pycnocline of any size. Where figure (5.8a) has very weak vortices, figure (5.8b) has a lift of $\sim 15\%$. The figures do not show whether a thicker pycnocline results in a larger lift of vortices from the bottom of the water column. Our investigation indicates that future simulations should be run with a three-layered fluid to increase the vortex shedding and global instabilities at the bottom of the wave tank.

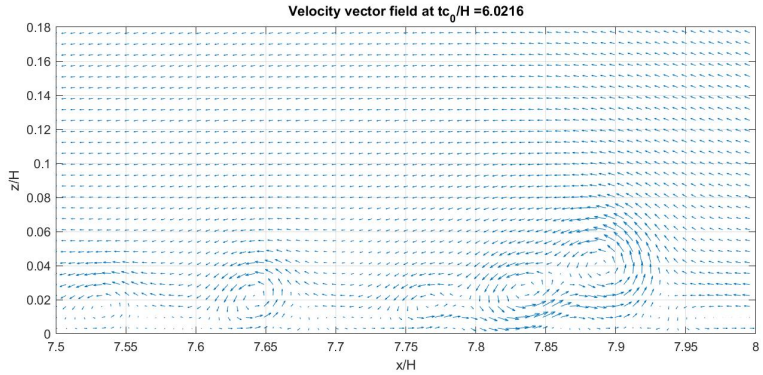

(a) No pycnocline

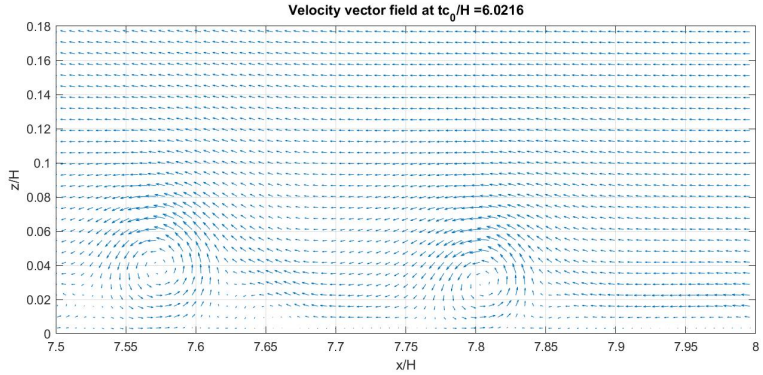

(b) Small pycnocline

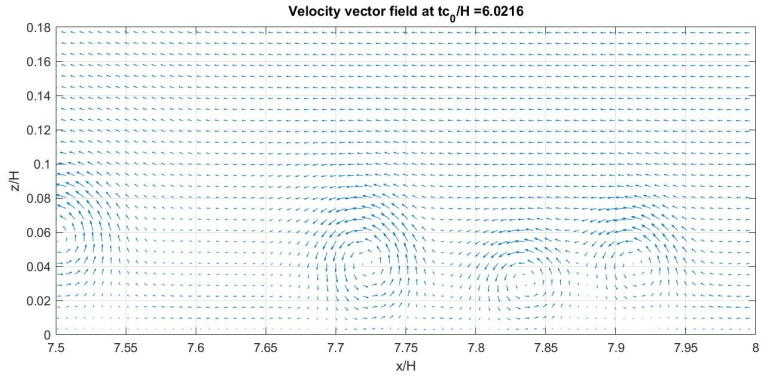

(c) Medium pycnocline

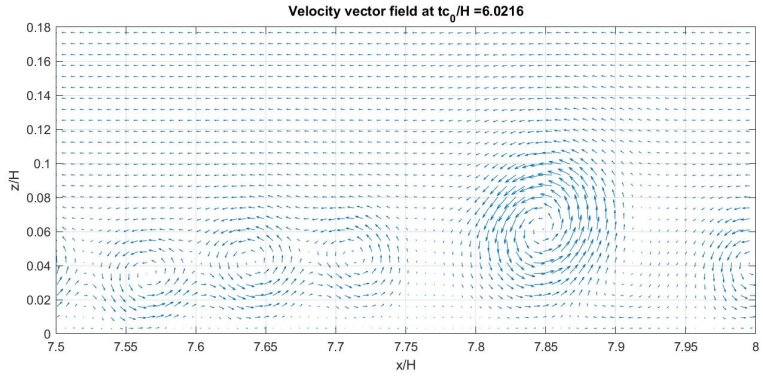

(d) Large pycnocline

Figure 5.7: Velocity vector field at $tc_0/H \approx 6.0$ for different pycnocline thicknesses

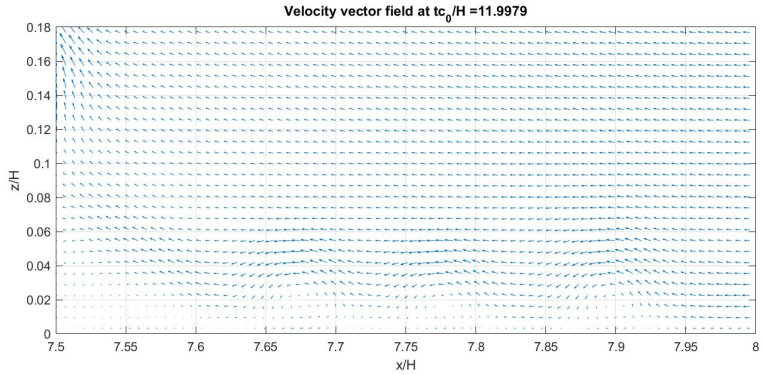

(a) No pycnocline

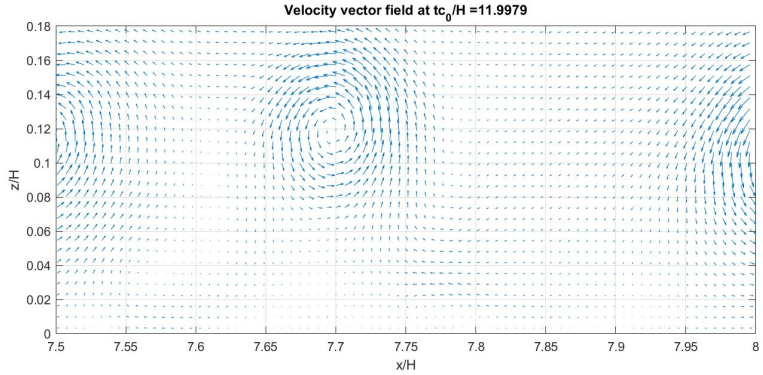

(b) Small pycnocline

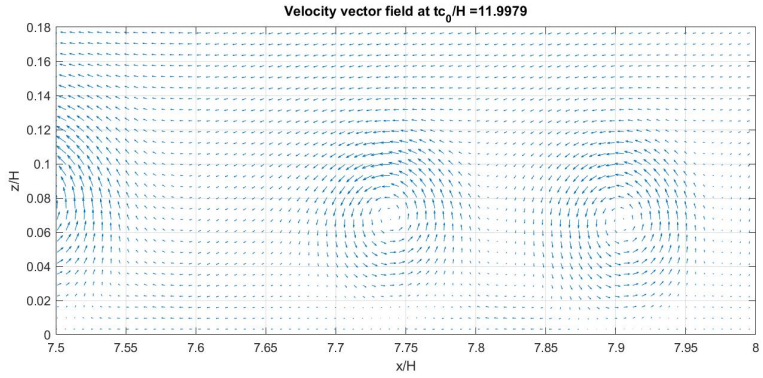

(c) Medium pycnocline

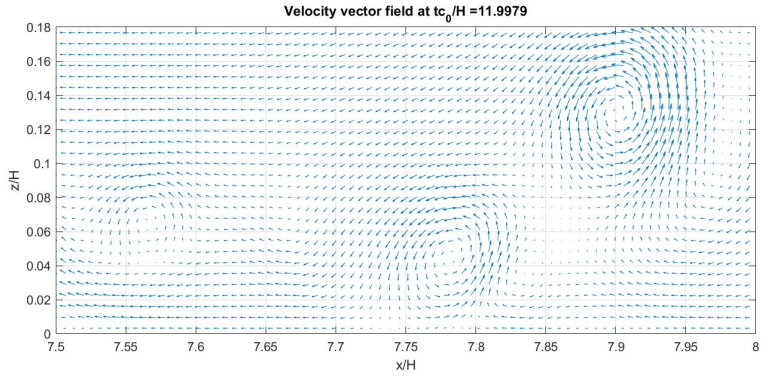

(d) Large pycnocline

Figure 5.8: Velocity vector field at $tc_0/H \approx 12.0$ for different pycnocline thicknesses

5.3 Implications of changing the upper-layer thickness

In this project, the relative upper layer thickness h_1 has been varied. To get a better understanding of the consequences of these changes, a comparison has been made for various upper layer thicknesses. The only parameter changed in this test was the different layer heights to obtain the wanted nonlinearities. This means that the initial volume and total height H were kept constant for all simulations. The different nonlinearities used are given in table (5.3).

H/h_1	6.23
H/h_1	8
H/h_1	10

Table 5.3: The different nonlinearities investigated

The linear wave speed is, as mentioned before, given as $c_0 = \frac{gh_1h_2(\rho_2-\rho_1)}{\rho_1h_2+\rho_2h_1}$ for a two-layered fluid. From this equation, we see that a decrease in the upper-layer thickness results in a smaller linear wave speed. We will now investigate the horizontal velocity profile at the bottom of the wave tank. From figure (5.9) we see that as the nonlinearity increases, the induced fluid velocities also increase in the lower layer. Since we know that an increase of the nonlinearity decreases the linear wave speed c_0 we wanted to investigate the differences if we assumed a constant linear wave speed. This resulted in figure (5.10). Here we see that the induced fluid velocities becomes very equal. This means that as the nonlinearity of a wave increases, the relative velocities in the fluid increases compared to the linear wave speed, while the observed velocities becomes similar in size.

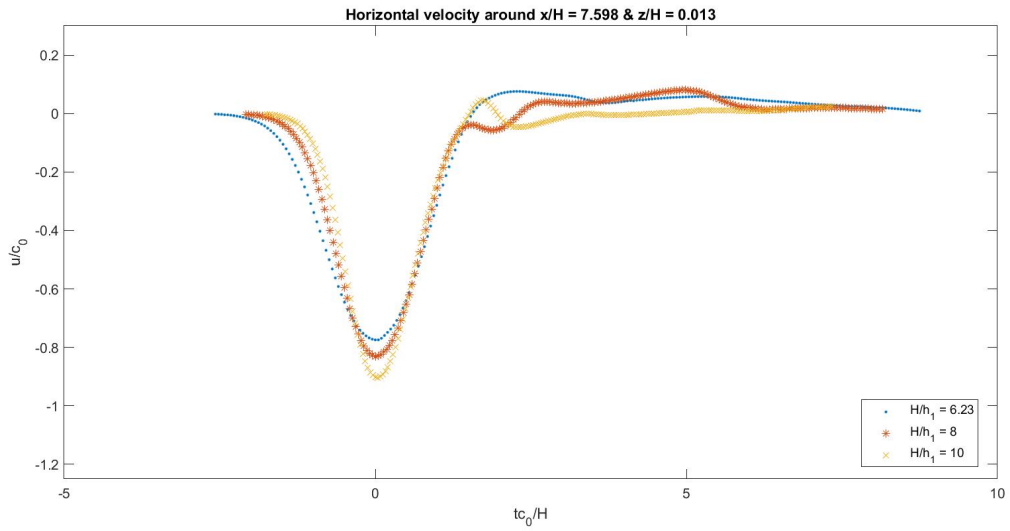

Figure 5.9: Comparison of horizontal velocity at the bottom of the wave tank for different upper-layer thicknesses

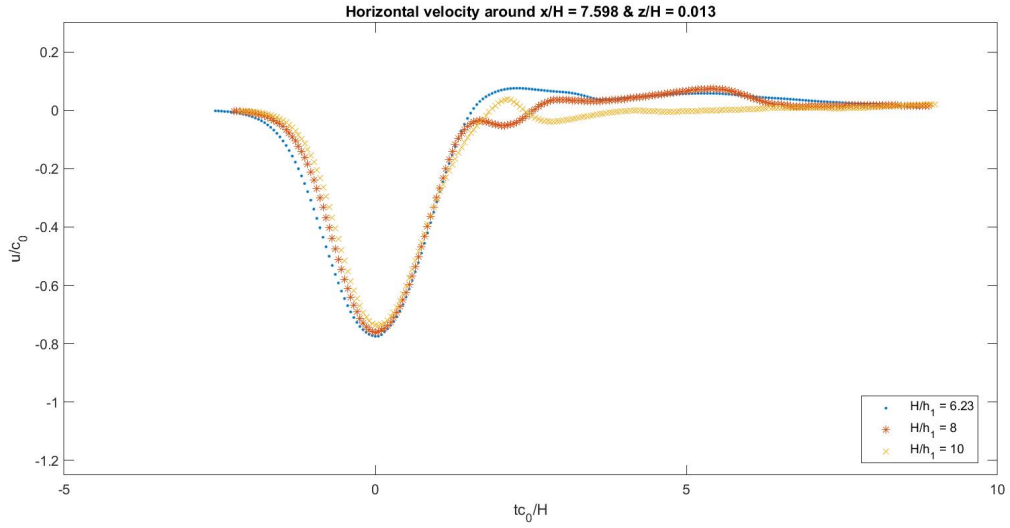

Figure 5.10: Comparison of horizontal velocity at the bottom of the wave tank for different upper-layer thicknesses, constant c_0

At last, we wanted to see whether an increase in the nonlinearity resulted in stronger global instabilities in the wave tank. We have therefore plotted the velocity vector field for the three different nonlinearities as seen in figure (5.11). The vortices that develop looks to have the same size and height for all three thicknesses of h_1. Longer simulations should be performed to see if the behaviour changes as time increases.

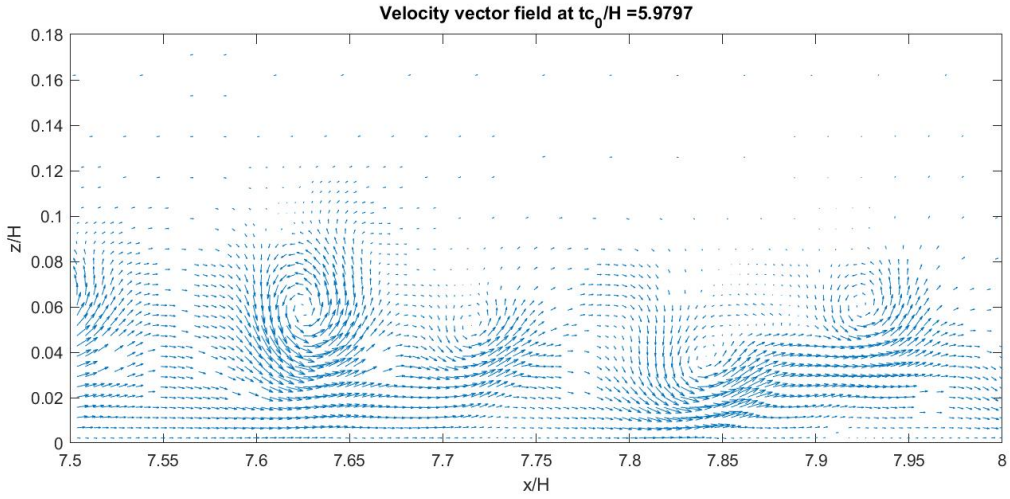

(a) $H/h_1 = 6.23$

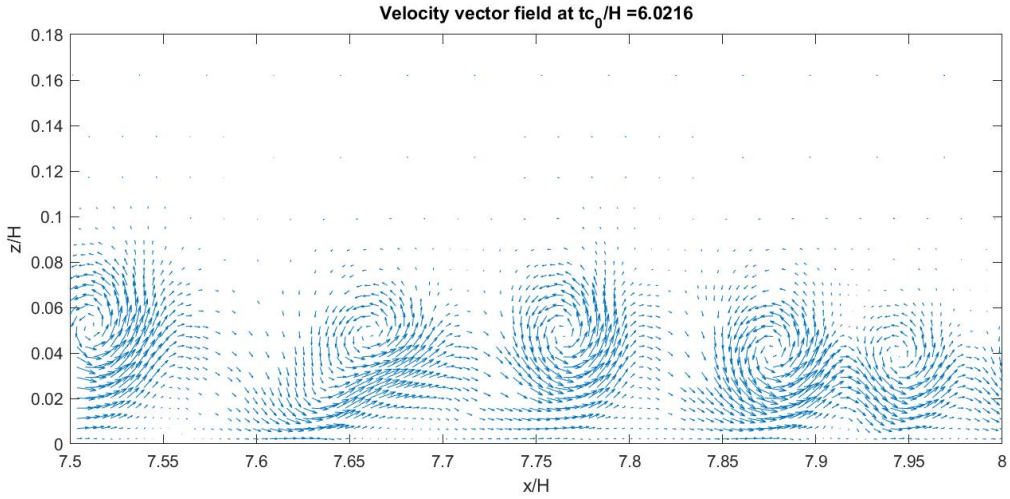

(b) $H/h_1 = 8$

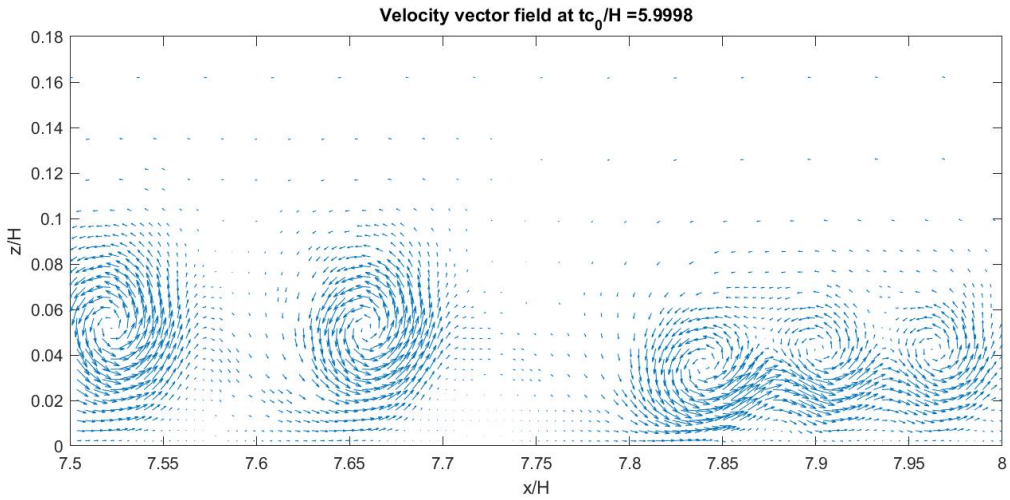

(c) $H/h_1 = 10$

Figure 5.11: Velocity vector field at $tc_0/H \approx 6$ for different values of H/h_1

CHAPTER 6

Summary and conclusion

We have in this study investigated the global instability in the bottom boundary layer, induced by large internal solitary waves, by using the numerical tool of Basilisk. Our work can be divided into three categories. First, we have a validation test of Basilisk against both experiments and analytic theory. Secondly, we have simulations using a flat bottom. Here we used both a two- and three-layered fluid of different wave amplitudes. Lastly, we performed simulations with two sloping bottoms of different steepness using a three-layered fluid.

Basilisk proved to compare well to fully nonlinear theory for all measured parameters, such as wave profile η, horizontal velocities u and wave propagation speed c. A deviation from theory was found when we increased the non-dimensional amplitude a/h_1 in accordance with Grue et al. (1999) [18], where Kelvin-Helmholtz instabilities grew strong, which broadened the tail of the wave. Kelvin-Helmholtz instabilities proved to appear for larger non-dimensional amplitudes a/h_1 for our modified solver using a passive tracer to track the interface compared to using a VOF solver that defined the interface more sharply. When we compared both solvers to experiments performed in the hydrolab at UiO, we found the modified solver to give the best representation of the resulting flow field. A small overestimation of the horizontal velocities near the bottom was found with the modified solver compared to experiments.

Through our study, we discovered that different pycnocline thicknesses affected the wave profile and global instabilities for large amplitudes (section 5.2). ISWs proved to better retain their wave shape in a three-layered fluid. This increased the induced velocities in the bottom layer and enhanced global instability. A three-layered fluid is also more representable to the actual ocean environment. A comparison was also performed against experimental work done by Carr et al. (2008) [8]. These results proved to compare well to the reverse flow, horizontal and vertical velocities in the lower layer. Global instabilities appeared at an earlier stage in Basilisk compared to the experiments, but the resulting velocity vector field from Basilisk were in good accordance with the results from Carr et al.

A broad variety of tests were performed to make sure that our numerical model was reliable for all parameters present. Our results showed that Basilisk compared well to both theory and experiments. A convergence test was also performed, which showed that the wave profile and velocity profiles converged towards the same results as the resolution

increased. For particle trajectories, it was more difficult to establish convergence since the global instability is a turbulent and random process, however, they did show a similar behaviour.

Having established that Basilisk can be used to represent ISWs in a good way, a comparison was performed between a two- and three-layered fluid of moderate amplitude. The motivation for running such a test was to see the relative differences between having a two- and three-layered fluid for otherwise equal parameters. This test showed us that the horizontal velocity in the upper layer $u(z = h_1/2)$ changed its shape. They differed by attaining a larger maximum velocity, and changed towards having a more pointy shape compared to fully nonlinear theory for a two-layered fluid. This was explained by conservation of mass in a water column. The amount of water entering a horizontal column in the fluid, must also leave the horizontal column. When adding a pycnocline to our simulation, the relative upper layer h_1 became smaller in size. In order to conserve the mass, the velocities had to increase in the upper layer.

In this study, the linear wave speed has been calculated in two different ways. For a two-layered fluid, we have used:

$$c_0^2 = \frac{gh_1h_2(\rho_2 - \rho_1)}{\rho_1 h_2 + \rho_2 h_1} \tag{6.1}$$

We also introduced a formula for the linear wave speed of a stratified ocean, valid for all stratifications:

$$c_0^2 = -\frac{\int_{-H}^{0} N^2(\phi^2)_z dz}{\int_{-H}^{0}(\phi_z^2)_z dz} \tag{6.2}$$

The relationship between the linear wave speed for a two- and three-layered fluid of otherwise equal parameters showed a large difference as seen in equation (6.3). When looking at the wave propagation speed for a two- and three-layered fluid, it showed that the relationship c/c_0 increased when using a three-layered fluid compared to a two-layer fluid. This meant that the excess propagation speed increased if we added a linear stratification to the water column. The relationship in equation (6.3) is only an example for a given stratification and will change when changing the stratification.

$$\frac{c_{0,2lay}}{c_{0,3lay}} = 1.0962 \tag{6.3}$$

In order to maximize the global instability and the vertical transportation of particles from the bottom of the wave tank, we performed several changes to try to enhance the global instability. We started by increasing the nonlinearity of the problem by reducing the upper layer height to $H/h_1 = 10$. When reducing the upper layer thickness, the excess velocities c/c_0, u/c_0 and w/c_0 increased in the fluid (section 5.3). The next step was to increase the wave amplitude. This was done by using the internal wave program IW2 developed by P. O. Rusaas [36] to find the necessary volume for creating a wave of amplitude close to half of the depth of the water column. The input amplitude was

calculated using ($\frac{a+h_1}{H} \approx 1/2$). We also added a sloping bottom to our simulations to see how this affected the global instability.

When we increased the dimensionless amplitude a/h_1, simulations were performed with both a two- and three-layered fluid. A large wave amplitude proved to have a huge impact on the wave profile. Due to a large number of Kelvin-Helmholtz instabilities present, the wave shape was changed for both layer types. But where the three-layered fluid managed to retain its wave shape in a decent manner, the wave profile from the two-layered fluid became very broad and the wave amplitude decreased. The broadening of the wave resulted in a dimensionless amplitude $a/h_1 = 3.20$ for the two-layered fluid while an amplitude of $a/h_1 = 3.75$ was obtained for the three-layered fluid. These results also affected the induced velocity profiles where the three-layered fluid had larger induced fluid velocities both in the upper and lower layer.

By using Lagrangian particle tracking, we obtained an illustration of how fluid particles are transported in the fluid. Several simulations were performed to verify the results. The results showed that both a two- and three-layered fluid had particles reaching the same maximum height at 20%, but the three-layered fluid had a much larger quantity of particles getting lifted from the bottom of the wave tank. We performed several simulations to look for convergence, and obtained similar results with a large number of particles getting lifted 20%.

The simulations performed with a flat bottom showed particles getting lifted 20% of the total water column. Diamessis and Redekopp [12] performed similar numerical simulations, but for weakly nonlinear equations, and obtained a lift of nearly 30-35%. We have previously shown that weakly nonlinear theory compares well to both fully nonlinear theory and simulations for non-dimensional amplitudes up to $a/h_1 = 0.4$ in accordance with Grue et al. (1999) [18]. When the amplitude increases above this level, the wave profiles created with weakly nonlinear theory becomes more narrow-crested. Our comparison of a two- vs three-layered fluid has shown that the global instability is increased for a three-layered fluid due to its better ability to maintain its wave form and obtain a steeper tail of the wave. This resulted in larger fluid velocities and hence stronger global instabilities. Diamessis and Redekopps use of weakly nonlinear theory can therefore have strengthened the global instability by having a very steep wave tail. Experimental work performed by Carr et al. (2008) [8] showed a maximal disturbed depth of 17%. Their setup gave the non-dimensional height of $H/h_1 = 4.83$ and their wave amplitude had a maximal displacement of the total water column given as $(a + h_1)/H = 0.47$. The simulation performed in Basilisk had a non-dimensional height of $H/h_1 = 10$ and a wave displacement of $(a + h_1)/H = 0.475$ of the total water column. A resulting lift of 20% of the water column is therefore in accordance with what we would expect when comparing to Carr et al.

Previously, a study by Aghsaee et al. (2012) [1] suggested the important role of shoaling ISWs in sediment resuspension. Shoaling waves had larger vertical velocities, higher bed shear and a greater energy transfer to the separation bubbles. This motivated us to include a sloping bottom to our simulations. Two different slopes were introduced to study how this affected the global instability. As the ISW propagated up the slope, the wave got compressed and the amplitude reduced. The wave was also constantly broadening. Adding a slope had large implications on the vortices that evolved. These were very large

in magnitude compared to simulations on a flat bottom with same initial conditions. The slope having a steepness of $\alpha = 0.014$ had a lift of particles of 40% of the total water column (scaled with H defined with a flat bottom). The vortex also had a size of 20% of the total water column, which is considered very large. Similar behaviour was found when we increased the slope steepness to $\alpha = 0.028$. The wave profile experienced the same behaviour as before. For the steeper slope, the vortex increased in size to 30% of the water column. This increase in vortex strength resulted in better lift of particles and a large amount of particles getting lifted to $z/H = 60\%$ of the total water column. We also had particles exceeding this value and reaching as high as 80% of the total water column. The increase in vortex strength with increase in slope steepness got related to an increase in the strength of the reverse flow. We believe that an increase of the velocities in the reverse flow results in stronger bed-shear, resulting in the creation of larger vortices. We know from theory that the maximum possible obtained amplitude for a two-layered fluid is given by $(a + h_1)/H = 1/2$. However, for a three-layered fluid this value can be exceeded. Knowing that an ISW has a maximum displacement of half the ocean depth, we achieve complete mixing of the water column due to the large lift of particles experienced when adding a sloping bottom.

Our results suggest that the presence of a sloping bottom has large implications on the strength of the global instability, in accordance with Aghsaee et al. (2012) [1]. We used an angle of 2.8°for the steepest slope. This is comparable to the average angle of the continental slope, which lays on 4°. On the continental shelf, the average slope steepness is 1°. Knowing this combined with our results, we understand that the global instability that occurs in the ocean can have a strong effect on mixing in the entire water column, and contribute towards resuspension of sediments from the sea floor.

If we go back to the example from the introduction, internal waves were observed in Vesterålen close to a coral reef and in an area of high fishing density. A sloping bottom with average steepness of 3.2°was also present in this area. We have in our study showed that the instability appearing beneath a large ISW of depression can contribute massively towards resuspending sediments from the sea floor, especially when having a sloping bottom. If we include the ocean currents, we have a system where sediments from the sea floor gets lifted high up in the water column where ocean currents act as a transport mechanism, spreading nutrition over a larger area. In addition to this, nutrition from the upper part of the ocean is transported downwards with the ISWs and we get a complete mixing of the water column. Based on our results, ISWs can be considered as a nutrition pump that given the right conditions, can create an environment ideal for the ocean biology.

Bibliography

[1] Aghsaee, P., Boegman, L., Diamessis, P. J., and Lamb, K. G. "Boundary-layer-separation-driven vortex shedding beneath internal solitary waves of depression". In: *J. Fluid Mech.* 690 (2012), pp. 321–344.

[2] Amick, C. J. and Turner, R. E. L. "A global theory of internal solitary waves in two-fluid systems". In: *Trans. Amer. Math. Soc* 298 (1986), pp. 431–484.

[3] Benjamin, T. B. "Internal waves of permanent form in fluids of great depth". In: *J. Fluid Mech.* 29 (1967), pp. 559–592.

[4] Benney, D. J. "Long nonlinear waves in fluid flows". In: *J. Math. Phys* 45 (1966), pp. 52–63.

[5] Bogucki, D. and Garret, C. "A simple model for the shear-induced decay of an internal solitary wave". In: *J. Phys. Oceanogr.* 23 (1993), pp. 1767–1776.

[6] Bogucki, D., Redekopp, L. G., and Barth, J. "Internal solitary waves in the Coastal Mixing and Optics 1996 experiment: multimodal structure and resuspension." In: *J. Geophys. Res.* 110 (2005), p. c02024.

[7] Carr, M. and Davies, P. A. "The motion of an internal solitary wave of depression over a fixed bottom boundary in a shallow, two-layer fluid". In: *Physics of Fluids* 18 (2006).

[8] Carr, M., Davies, P. A., and Shivaram, P. "Experimental evidence of internal solitary wave-induced global instability in shallow water benthic boundary layers". In: *Physics of Fluids* 20 (2008).

[9] Carr, M., Franklin, J., King, S. E., Davies, P. A., Grue, J., and Dritschel, D. G. "The characteristics of billows generated by internal solitary waves". In: *J. Fluid Mech.* 812 (2017), pp. 541–577.

[10] Carr, M., Fructus, D., Grue, J., Jensen, A., and Davies, P. A. "Convectively induced shear instability in large amplitude internal solitary waves". In: *Physics of Fluids* 20 (2008).

[11] Carter, G. S., Gregg, M. C., and Lien, R. C. "Internal waves, solitary-like waves, and mixing on the Monterey Bay shelf." In: *Cont. Shelf Res.* 25 (2005), pp. 1499–1520.

[12] Diamessis, P. J. and Redekopp, L. G. "Numerical investigation of solitary internal wave-induced global instability in shallow water benthic boundary layers". In: *J. Phys. Oceanogr.* 36 (2006), pp. 784–812.

[13] Dold, J. W. and Peregrine, D. H. “An efficient boundary-integral equation method for steep unsteady water waves.” In: *Numerical Methods for Fluid Dynamics*. Ed. by Morton, K. W. and Baines, M. J. Vol. 2. Clarendon press, 1985, pp. 661–670.

[14] Duda, T. F., Lynch, J. F., Irish, J. D., Beardsley, R. C., Ramp, S. R., Siu, C.-S., Tang, T. Y., and Yang, Y.-J. “Internal tide and nonlinear internal wave behavior at the continental slope in the northern South China Sea”. In: *IEEE J. Oceanic Eng.* 29 (2004), pp. 1105–1130.

[15] Fructus, D. and Grue, J. “Fully nonlinear solitary waves in a layered stratified fluid”. In: *J. Fluid Mech.* 505 (2004), pp. 323–347.

[16] Geographic, N. *Why it’s important to save our sea’s pristine places*. Feb. 2017. URL: https://www.nationalgeographic.com/magazine/2017/02/saving-our-seas-president-obama-oceans-conservation/ (visited on 04/30/2019).

[17] Grue, J., Friis, A., Palm, E., and Rusaas, P. O. “A method for computing unsteady fully nonlinear interfacial waves”. In: *J. Fluid Mech.* 351 (1997), pp. 223–252.

[18] Grue, J., Jensen, A., Rusaas, P. O., and Sveen, J. K. “Properties of large amplitude internal waves”. In: *J. Fluid Mech.* 380 (1999), pp. 257–278.

[19] Grue, J. *Brytende bølger i Vesterålen. En driver av biomasseproduksjon.* 2018.

[20] Grue, J. “Havets indre bølger”. In: *Naturen* 6 (2013), pp. 210–227.

[21] Grue, J., Jensen, A., Rusås, P.-O., and Sveen, J. K. “Breaking and broadening of internal solitary waves”. In: *J. Fluid Mech.* 413 (2000), pp. 181–217.

[22] Grue, J. and Trulsen, K. “Very large internal waves in the ocean — observations and nonlinear models.” In: *Waves in Geophysical Fluids*. Vol. 489. Oxford: CISM International Centre for Mechanical Sciences, 2006. Chap. 5, pp. 205–270.

[23] Hooft, J. A. van, Popinet, S., and Heerwaarden et al, C. van. “Towards Adaptive Grids for Atmospheric Boundary-Layer Simulations”. In: *Boundary-Layer Meteorol* (2018), pp. 167–421.

[24] Jeans, D. R. G. and Sherwin, T. J. “The evolution and energetics of large amplitude nonlinear internal waves on the Portuguese shelf”. In: *J. Mar. Res* 59 (2001), pp. 327–353.

[25] Joseph, R. I. “Solitary waves in a finite depth fluid”. In: *Journal of Physics* 10.12 (1977), pp. L225–L227.

[26] Keulegan, G. H. “Characteristics of internal solitary waves”. In: *J. Res. Natl Bur. Stand.* 51 (1953), p. 133.

[27] Koop, C. G. and Butler, G. “An investigation of internal solitary waves in a two-fluid system”. In: *J. Fluid Mech.* 112 (1981), pp. 225–251.

[28] Kubota, T., Ko, D. R. S., and Dobbs, L. D. “Weakly-nonlinear, long internal gravity waves in stratified fluids of finite depth”. In: *J. Hydronaut.* 12 (1978), p. 157.

[29] Lamb, K. G. “Internal wave breaking and dissipation mechanisms on the continental slope/shelf”. In: *Annu. Rev. Fluid Mech.* 46 (2014), pp. 231–254.

[30] Laurent, L. S. “Turbulent dissipation on the margins of the South China Sea”. In: *Geophys. Res. Lett.* 35 (2008), p. L23615.

[31] Long, R. R. “Solitary waves in one- and two-fluid systems”. In: *Tellus* 6 (1956).

[32] Melville, W. K. and Helfrich, K. R. “Long nonlinear internal waves”. In: *Annu. Rev. Fluid Mech.* 38 (2006), pp. 395–425.

[33] Osborne, A. R. and Burch, T. L. “Internal solitons in the Andaman Sea”. In: *Science* 208 (1980), pp. 451–460.

[34] Perry, R. B. and Schimke, G. R. “Large amplitude internal waves observed off the northwest coast of Sumatra”. In: *J. Geophys. Res.* 70 (1965), pp. 2319–2324.

[35] Quaresma, L. S., Vitorino, J., Oliveira, A., and Silva, J. da. “Evidence of sediment resuspension by nonlinear internal waves on the western Portuguese mid-shelf”. In: *Mar. Geol.* 246 (2007), pp. 123–143.

[36] Rusaas, P. O. “The internal wave program, developed by P. O. Rusaas at University of Oslo, documented in: J. Grue et al *Properties of large-amplitude internal waves*”. In: *J. Fluid Mech.* 380 (1999).

[37] Segur, H. and Hammack, J. L. “Soliton models of long internal waves”. In: *J. Fluid Mech.* 118 (1982), pp. 285–304.

[38] Statsna, M. and Lamb, K. G. “Sediment resuspension mechanisms associated with internal waves in coastal waters”. In: *J. Geophys. Res.* 113 (2008).

[39] Statsna, M. and Lamb, K. G. “Vortex shedding and sediment resuspension associated with the interaction of an internal solitary wave and the bottom boundary layer”. In: *Geophysical Research Letters* 29.11 (2002).

[40] Turner, R. E. L. and Vanden-Broeck, J.-M. “Broadening of interfacial solitary waves”. In: *The Physics of Fluids* 31 (1988), p. 2486.